

DISSERTATION

COMBINATORIAL DISCOVERY AND OPTIMIZATION OF NOVEL  
METAL OXIDE MATERIALS FOR PHOTOELECTROLYSIS USING  
VISIBLE LIGHT

Submitted by

Michael Woodhouse

Department of Chemistry

In partial fulfillment of the requirements

For the Degree of Doctor of Philosophy

Colorado State University

Fort Collins, Colorado

Spring 2008

UMI Number: 3321322

### INFORMATION TO USERS

The quality of this reproduction is dependent upon the quality of the copy submitted. Broken or indistinct print, colored or poor quality illustrations and photographs, print bleed-through, substandard margins, and improper alignment can adversely affect reproduction.

In the unlikely event that the author did not send a complete manuscript and there are missing pages, these will be noted. Also, if unauthorized copyright material had to be removed, a note will indicate the deletion.

**UMI**<sup>®</sup>

---

UMI Microform 3321322

Copyright 2008 by ProQuest LLC.

All rights reserved. This microform edition is protected against unauthorized copying under Title 17, United States Code.

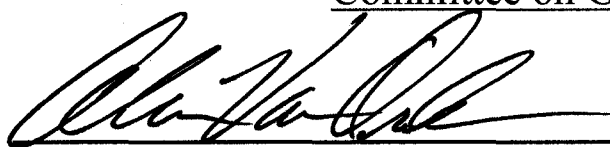
ProQuest LLC  
789 E. Eisenhower Parkway  
PO Box 1346  
Ann Arbor, MI 48106-1346

COLORADO STATE UNIVERSITY

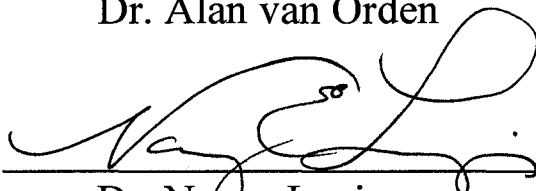
December 20, 2007

We hereby recommend that the dissertation prepared under our supervision by **Michael Woodhouse** entitled "Combinatorial Discovery and Optimization of Novel Metal Oxide Materials for Photoelectrolysis Using Visible Light" be accepted as fulfilling in part requirements for the degree of Doctor of Philosophy.

Committee on Graduate Work



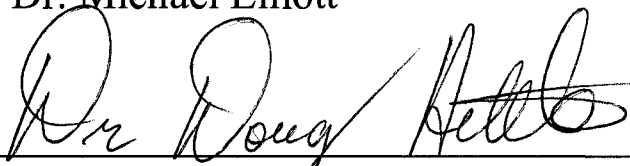
Dr. Alan van Orden



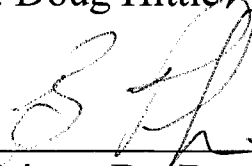
Dr. Nancy Levinger



Dr. Michael Elliott



Dr. Doug Hittle



Advisor- Dr. Bruce Parkinson



Department Head- Dr. Tony Rappe

## ABSTRACT OF DISSERTATION

### COMBINATORIAL DISCOVERY AND OPTIMIZATION OF NOVEL METAL OXIDE MATERIALS FOR PHOTOELECTROLYSIS USING VISIBLE LIGHT

Efficient and inexpensive production of hydrogen from water and sunlight has been the “holy grail” of photoelectrochemistry since Fujishima and Honda first demonstrated the feasibility of the process by illuminating TiO<sub>2</sub> single crystals with UV light. While it was a great proof of concept, a more suitable material will most likely be an oxide semiconductor containing multiple metals that will each contribute to the required properties of stability, light absorption, and being catalytic for hydrogen or oxygen evolution. Therefore we developed a high throughput combinatorial approach to prepare overlapping patterns of metal oxide precursors onto conducting glass substrates that can be screened for photoelectrolysis activity by measuring the photocurrent generated by rastering a laser over the materials while they are immersed in an electrolyte.

A ternary oxide containing cobalt, aluminum and iron, and not previously known to be active for the photoelectrolysis of water, was identified using the combinatorial technique. The optimal composition and thickness for photoelectrochemical response of the newly identified material has been further refined using quantitative ink jet printing. Chemical analysis of bulk and thin film samples revealed that the material contains cobalt, aluminum and iron in a Co<sub>3</sub>O<sub>4</sub> spinel structure with Fe and Al substituted into Co sites with a nominal stoichiometry of Co<sub>3-x-y</sub>Al<sub>x</sub>Fe<sub>y</sub>O<sub>4</sub> where x and y are about 0.18 and 0.30 respectively. The material is a *p*-type semiconductor with an indirect band gap of around 1.5 eV, a value that is nearly ideal for the efficient single photoelectrode photoelectrolysis of water. Photoelectrochemical measurements indicate that the material has a respectable photovoltage but the photocurrent is limited by the slow kinetics for hydrogen evolution. This new cobalt iron aluminum oxide is most likely not the “holy grail” of photoelectrochemistry that we seek, but our methodology gives a rational approach for future materials discovery and optimization.

Michael Woodhouse  
Department of Chemistry  
Colorado State University  
Fort Collins, CO 80523  
Spring 2008

## ACKNOWLEDGEMENTS

I came to graduate school for two reasons: because of my natural fascination with the physical sciences and because my idealistic fantasies created a desire within me to pursue a career in solar energy (which I largely attribute to concerns about global warming). Because I was a “non-traditional” student with a career as a high school Chemistry and Physics teacher in place, as well as a family, I had no idea how long I would be able to remain in graduate school. And now, five and half years after arriving at this campus, I can gratefully say that my original desires have been surpassed and I feel very fortunate to be able to pursue a valuable research opportunity in the solar energy arena at the National Renewable Energy Laboratory as the next step in my career.

But I most certainly did not achieve this on my own and I sincerely feel that I could not have picked a better place to pursue a PhD in Chemistry. There have been a lot of people here that have helped me along the way. I’ve had some great teachers here, both in the classroom and in the lab. Dr. Elliott has taught me a great deal and has, on several occasions, challenged me to think more deeply about certain things than I actually cared to, but I have always left those experiences both stronger and wiser. And I have formed a lifelong relationship with my advisor, Dr. Parkinson. As a member of his group, I have been presented with opportunities that exceeded my imagination. Together we have developed the project outlined in this thesis and he has passed on a lot of his knowledge about solar power generation to me. Our work has been integrated into four publications and numerous conferences and meetings. Before graduate school I had never even been outside the continent, but I have had two opportunities to go to Asia with him and to establish collaborations with international scientists. And now I can largely attribute the next step in my career to his help. I will always be willing to repay the debt I owe him in whatever way I can.

Finally, I would like to acknowledge the friendships that I have and say that they have been a tremendous help. I have faced many obstacles while I’ve been here, both personal and scientific, and I have really seen how mutually beneficial relationships can be invaluable in overcoming challenges and in making life an enjoyable endeavor.

# Table of Contents

## **Chapter 1: Background to Photoelectrolysis**

- 1.1 Material Requirements for Water Splitting with Solar Energy
- 1.2 Semiconductors and Energy Level Requirements for Photoelectrolysis
- 1.3 Combinatorial Production and Screening of New Materials

## **Chapter 2: Development of a Protocol for High Throughput Production and Screening of New Materials for Photoelectrolysis**

- 2.1 Preface
- 2.2 Introduction to the Development of High Throughput Production and Screening of Materials
- 2.3 Early Experimental History
- 2.4 Spray Pyrolysis

## **Chapter 3: A Combinatorial Approach to Identification of Catalysts for the Photoelectrolysis of Water**

- 3.1 Preface
- 3.2 Abstract
- 3.3 Introduction
- 3.4 Experimental Section
- 3.5 Results and Discussion
- 3.6 Conclusions

## **Chapter 4: Development of Protocol for Optimization of Materials Discovered in the Combinatorial Search**

- 4.1 Preface and Abstract
- 4.2 The Development of an Appropriate Precursor Formulation for Printing and Substrate Pretreatment
- 4.3 Substrate and Electrolyte Optimization for the Fe-Co-Al Oxide

## **Chapter 5: Combinatorial Discovery and Optimization of a Complex Oxide with Water Photoelectrolysis Activity**

- 5.1 Preface
- 5.2 Abstract
- 5.3 Introduction
- 5.4 Experimental
- 5.5 Results and Discussion
- 5.6 Conclusions

## **Chapter 6: Ongoing and Developing Work: Spatial Mapping of the Absorbed-Photon-to-Current Collection Efficiency**

- 6.1 Methodology Description

## **Chapter 7: Conclusions and Research Directions Needing Further Development**

- 7.1 Conclusions
- 7.2 Possible Directions for Future Research

## **Appendix A: Independent Research Proposal: Optimization of the Charge Transfer Kinetics For A Quantum-Confined Photoelectrode Material**

- A.1 Abstract
- A.2 Background and Significance
- A.3 Original Research Design, Methods, and Significance
  - A.3.1 Construction of Flat Quantum Dot Photoelectrodes
  - A.3.2 Construction of a Quantum-Dot Sensitized Nanocrystalline Scaffold
  - A.3.3 Analysis of the Photoelectrodes (Original Design)
- A.4 Revised Research Design, Methods, and Analysis
- A.5 Discussion of Possible Results (Revised Design)
- A.6 Concluding Remarks

## **Appendix B: Introduction to the High Throughput Materials Screening Database**

## Index of Figures

Fig. 1.1: Hybrid approaches for the splitting of water using non-oxide materials . . . . .	3
Fig. 1.2: Semiconductor-electrolyte junction energetics for the water splitting half-reactions . . . . .	6
Fig. 1.3: Photoelectrolysis cell configurations for the different types of semiconductors and a tandem system. . . . .	9
Fig. 1.4: The bandgap characteristics for several known and ideal photoelectrolysis materials . . . . .	11
Fig. 1.5: Conceptual representation of a single-electrode photoelectrolysis system with a reduced band gap . . . . .	16
Fig. 2.1: Original design of material mixtures to be printed and screened . . . . .	29
Fig. 2.2: The photoelectrochemical screening system used throughout this project. . . . .	33
Fig. 2.3: Typical high resolution SEM images of Si-doped $\alpha$ -Fe <sub>2</sub> O <sub>3</sub> nanoleaf films on SnO <sub>2</sub> :F obtained by the Grätzel group. . . . .	39
Fig. 2.4: Current configuration for a simple spray pyrolysis system	41
Fig. 2.5: Example of the uniformity capabilities once the spray pyrolysis technique had been optimized. . . . .	43
Fig. 2.6: The most efficient area of a metal oxide film deposited by spray pyrolysis . . . . .	44
Fig. 3.1: Overprinting a gradient pattern to optimize the metal oxide thickness. . . . .	55
Fig. 3.2: Printing and screening a four-metals-three-at-a-time pattern and a compositional zoom for the Fe-Cs-Nd-Cu system. . . . .	57
Fig. 3.3: Printing and screening at two laser wavelengths and two different biases a four-metals-three-at-a-time pattern for the Fe-Cs-Co-Al system. . . . .	61
Fig. 3.4: SEM image of the bright area shown in the photocurrent scan of Figure 3.2D showing that in this area the metal oxide film is a porous film overlaying the conductive SnO <sub>2</sub> :F substrate. . . . .	63
Fig. 3.5: Photocurrent action spectrum measured in the area of the bright spot seen in Figure 3.3C and 3.3E and outlined with a green circle in the inset. . . . .	65

Fig. 4.1: Hypothetical circuit patterns created by printing and screening $\alpha\text{-Fe}_2\text{O}_3$ precursors. . . . .	76
Fig. 4.2: The <i>first</i> (and unstable) dark and photocurrent-voltage curves obtained for a 2 cm x 2 cm film printed onto an FTO substrate immersed in deoxygenated 50-mM $\text{HClO}_4$ . . . . .	78
Fig. 4.3: Selected cyclic voltammetry curves for the photoelectrodeposition of platinum metal onto for a 2 cm x 2 cm film printed onto an FTO substrate. . . . .	80
Fig. 4.4: Selected scanning electron microscope (SEM) images of a freshly prepared Al-Co-Fe oxide sample on FTO and after all 11 of the Pt deposition cyclic voltammetry cycles shown in Figure 4.3. . . . .	81
Fig. 4.5: Current-Voltage curves for a 2 cm x 2 cm photocatalyst film printed on an FTO substrate. . . . .	84
Fig. 4.6: Current-Voltage curves for a 2 cm x 2 cm photocatalyst film printed on an FTO substrate immersed in a deoxygenated 0.1-M NaOH solution. . . . .	85
Fig. 4.7: A sampling of cyclic voltammetry curves for pure FTO immersed in several of the electrolytes studied . . . . .	88
Fig. 4.8: Dark and photocurrent-voltage curves for a 2 cm x 2 cm film printed onto a gold-on-chromium-on-mica substrate immersed in deoxygenated 0.1-M NaOH. . . . .	90
Fig. 5.1: Template showing the gradient pattern used for printing the metal nitrate precursors for the Al-Co-Cs-Fe system. . . . .	101
Fig. 5.2: Printing template used for quantifying the optimal stoichiometry in the Co-Al-Fe system where known amounts of the components are printed into individual squares. . . . .	103
Fig. 5.3: Compositional library produced by expansion of the compositional region outlined by the white box in Fig. 5.2. . . . .	105
Fig. 5.4: Action spectra normalized to a constant value at 500-nm for the data obtained from the compositions outlined in figure 5.2 and figure 5.3. . . . .	107
Fig. 5.5: Glancing Angle XRD for a film printed onto a flourine-doped tin oxide substrate and powder XRD for the 84% Co, 10% Fe, and 6% Al bulk sample. . . . .	109
Fig. 5.6: Thickness optimization for the optimized stoichiometry printed onto a flourine-doped tin oxide substrate. . . . .	110
Fig. 5.7: Adding a fourth component to the optimized ternary composition into individual squares. . . . .	112

Fig. 5.8: SEM images at different magnifications for the film used for measurement of the current-voltage curves and sample printed on FTO. . . . .	114
Fig. 5.9: Dark and photocurrent-voltage curves for a film printed onto a gold-on-chromium-on-mica substrate immersed in deoxygenated 0.1-M NaOH. . . . .	115
Fig. 6.1: Schematic of the equipment used to spatially record photocurrent, incident photon-to-current conversion efficiency, and/ or absorbed photon-to-current conversion efficiency. . . . .	124
Fig. 6.2: Example of the spatial mapping of APCE for a region of the thickness study described in figure 5.6. . . . .	126
Fig. 6.3: SEM images showing “monodisperse” 55-nm nanoparticles of $\alpha$ -Fe <sub>2</sub> O <sub>3</sub> on FTO (courtesy of Jianghua He). . . . .	129
Fig. 6.4: Example of spatial mapping of APCE for a sample of $\alpha$ -Fe <sub>2</sub> O <sub>3</sub> nanoparticles drop-cast onto FTO. . . . .	131
Fig. 7.1: Pictures of how the materials search program has been extended to undergraduate research. . . . .	136
Fig. A.1: Plots of the free energy, G, versus reaction coordinate, q, for reactants (R) and products (P), for three different values of $\Delta G^\circ$ . . . . .	144
Fig. A.2: Recent experimental observations displaying the expected dependence of single electron transfer rate constant on free energy difference and reorganization energy. . . . .	145
Fig. B.1: Sample screen of a combination in the ternary mixtures library. . . . .	169
Fig. B.2: The right side of the sample screen of a combination in the ternary mixtures library. . . . .	170

### Index of Tables

Table 5.1: Density of printed precursor drops used to produce the mixtures shown in Figure 5.2. . . . .	103
Table 5.2: Density of printed precursor drops used to produce the mixtures show in Figure 5.3. . . . .	105
Table 5.3: Drop spacing and calculated average thickness for the squares printed and mapped for photoactivity in fig. 5.6. . .	111

# **Chapter 1: Background to Photoelectrolysis**

## **1.1 Material Requirements for Water Splitting with Solar Energy**

As concerns about the use of fossil fuels mounts, whether from the standpoint of limited supply or from the consequences of potentially drastic climate change resulting from their use, the vision of a hydrogen-based economy evolves from “fantasy” into something more urgent. In addition to the fact that its combustion only produces water if used in a fuel cell, and ignoring for now the potential problems of storage that will hopefully be overcome as well, hydrogen is the ideal source of energy if it can be produced from the photoelectrolysis of water. In principle, such a process should provide completely renewable, nearly pollution-free energy provided that the appropriate materials can be found to perform the job.

It is rather straightforward to imagine the process as being a simple extension of solar energy processes using traditional photovoltaic materials, such as Si or compound semiconductors, in series connection to provide the necessary power for the electrolysis of water in an electrolyzer composed of two metal electrodes in an electrolyte.

Alternatively, the same material(s), in a *p-n* junction in order to provide the needed voltage, could be immersed directly into the electrolyte and one of the two water splitting half-reactions (most commonly the reduction reaction) would occur on its surface while the other occurred on a metallic counter electrode. A number of these “monolithic” configurations have been demonstrated, one of the more prominent being that shown in Figure 1.1.C<sup>1</sup>.

The problem with this approach has historically been twofold. The first is economic. Because the cost of solar power, expressed in dollars per watt calculated from the capitalization necessary to produce and install solar cells, is currently more than the cost of electricity from coal-fired power plants, electrolysis would be more cost effective if carried out by the mainstream power sources. Also, the cost of hydrogen, in dollars per Joule, is **much** higher than that of oil even when produced other means such as hydrocarbon cracking. The second problem, germane to photoelectrolysis where the semiconductor electrode is immersed in the solution, has been degradation of performance over time as the semiconductors have been unstable in aqueous electrolytes. For reasons that will be discussed in detail later, it is believed that metal oxides (i.e. nontraditional solar energy materials) hold the most promise for a stable photoelectrolysis system.

The genesis of hope for the conversion of sunlight to chemical potential energy by splitting water with metal oxides was generated from a series of experiments that used the semiconductor rutile  $\text{TiO}_2$ <sup>2,3</sup>. Unfortunately, there were complications that were

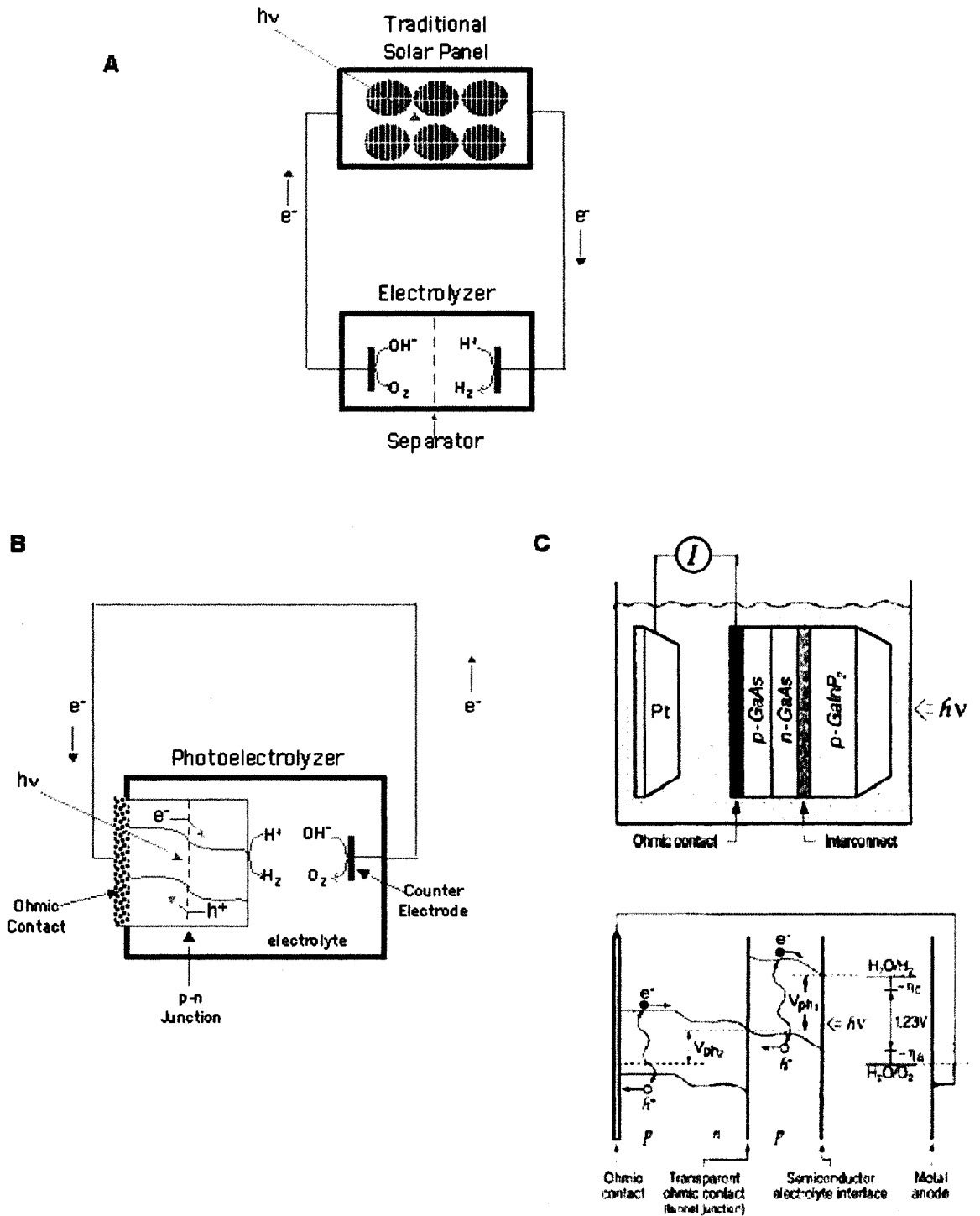


**Figure 1.1 Hybrid approaches for the splitting of water using non-oxide materials.** In A, a simple extension is shown where an external solar panel can be used to provide the power for the direct electrolysis of water. In Figure B, similar materials without a protective enclosure are immersed in an electrolyte to carry out one of the half-reactions (adapted from reference 4). Figure C displays one of the more prominent publications utilizing this “monolithic” approach<sup>1</sup>.

immediately evident and, thirty years later, we have more thoroughly identified, but not completely overcome, the same original issues. Certain facts regarding photoelectrolysis have been established and we are left with no choice but to find new materials that simultaneously conform to the thermodynamic realities *and* prove economically feasible. In this chapter I will give a brief review of the principles and history of photoelectrolysis using metal oxides, discuss the associated obstacles that have been revealed using these materials, and then offer a glimpse of hope into how new (undiscovered) materials can help to overcome those obstacles.

## **1.2 Semiconductors and Energy Level Requirements for Photoelectrolysis**

The band theory of solids is based upon the quantum mechanical idea that when two wavefunctions overlap, one is raised in energy and one is lowered in energy<sup>4</sup>. When combining atoms to make molecules, chemists and physicists refer to the altered wavefunctions as orbitals. When an essentially infinite number of wavefunctions interact from the combining of atoms to any appreciable size, one creates “bands” of orbitals having different energies. In semiconductor parlance, the energy corresponding to the highest occupied molecular orbital (HOMO) is called the valence band edge and the energy corresponding to the lowest unoccupied molecular orbital (LUMO) is called the conduction band edge<sup>5</sup>.

Some semiconductors are suitable for water electrolysis based upon where their valence and conduction band edges are relative to the two water splitting half reactions

on a reference scale (usually an electrochemical one or relative to the free-energy of an electron in a perfect vacuum). Figure 1.2 illustrates where the band edges should be (shown as flat for the sake of generalizing the doping type) for a single photoelectrode system to carry out the process<sup>6</sup>. Incident radiation with an energy in excess of the semiconductor band gap creates electron-hole pairs, some of which avoid recombination either at the surface or within the bulk and find their way to the semiconductor-liquid junction after thermalizing down to the band edges, shown as dashed lines in the figure. If the photoexcited electrons are contained within a conduction band that has a band edge more energetic than the proton reduction half-reaction, the holes are contained within a valence band that has a band edge more energetic than the water or hydroxide oxidation half reaction, **and** if there are no kinetic limitations to charge transfer for either process, then the separate hydrogen evolution reaction (HER) and the oxygen evolution reaction (OER) may occur. Because the energy difference between the oxidation and reduction half reactions for water is 1.23-eV, the physical requirement is that the forbidden band gap separation between the valence and conduction band edges must be *at least* 1.23 V. In reality, it has been calculated that the separation must be 1.5 - 2 eV in order to provide a enough overpotential to satisfy various kinetic requirements and to accommodate a phenomenon due to immersion in the electrolyte known as “band bending”<sup>7</sup>.

Because all of the metal oxide systems studied to date that are capable of functioning solely as a single electrode have band gaps that are too large to effectively

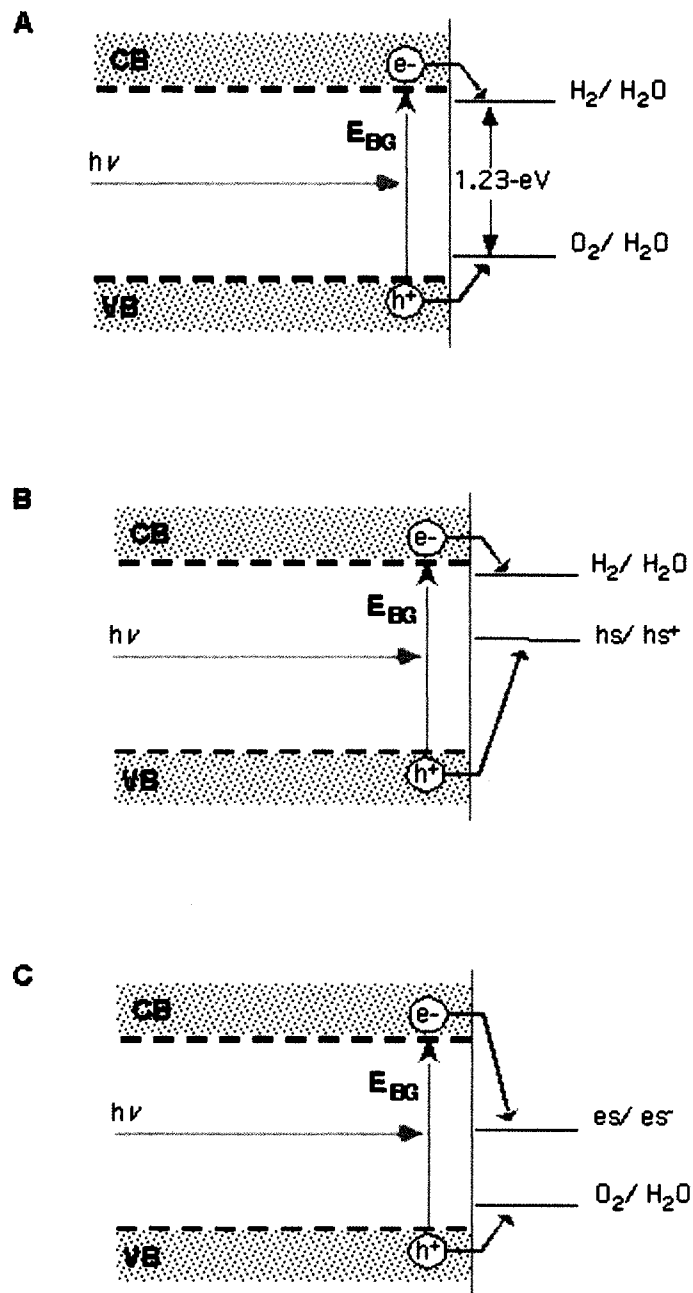


**Figure 1.2 Semiconductor-electrolyte junction energetics for the water splitting half-reactions.** In figure A, a single photoelectrode system capable of carrying out the two half-reactions is shown. In B, a photoelectrode system is shown for which a sacrificial "hole scavenger" such as a sulfite electrolyte or alcohol has been introduced into the system in order study the HER ability of the photoelectrode. In C, a photoelectrode system is shown for which a sacrificial "electron scavenger" such as an electrolyte containing  $Ag^+$  ions has been introduced into the system in order study the OER ability of the photoelectrode.

utilize the solar spectrum, “sacrificial reagents” are frequently added in the literature in order to study the HER and OER reactions separately for smaller band gap semiconductors (or perhaps in order to mask the inefficiency of the material for one of the half-reactions). The most common examples of an electron scavenger agent (labeled  $es/ es^-$ ) in Figure 1.1 is an electrolyte containing the easily reduced  $Ag^+$  cation and the most common example of hole scavenging agents introduced into solution are alcohols (usually methanol), amines (usually triethanol amine or EDTA) or sulfite salts. A large number of papers regarding photoelectrolysis contain these sacrificial reagents and so it is important to bear in mind that the reported efficiencies are probably much higher than would be achieved in a reversible, non-sacrificial system and that these systems can be thermodynamically “downhill” without any real overall energy gain.

A photoelectrolysis system can be made from a single *n*-type semiconductor electrode, a single *p*-type semiconductor, or a tandem system that utilizes both types as shown in Figure 1.2. When an *n*-type electrode (such as  $TiO_2$ ) is used to carry out the process, the semiconductor functions as a photoanode. Photoexcited electrons within the semiconductor travel through the external cell to carry out the HER at the metallic counterelectrode (typically Pt) while holes migrate to its surface to perform the OER. Unlike the case of dispersed catalyst powders (another trick one will frequently encounter in the literature) the two gases can be collected separately because they are being produced at different electrodes; an important point as separating the volatile mixture is rather difficult. In the case of a *p*-type photoelectrode, the two gases are produced at

opposite locations as the semiconductor functions as a photocathode. A tandem system, as shown in Figure 1.2c, provides a little more flexibility in the placement of the band edge positions relative to the redox potentials of water as well as flexibility with regard to the size of the band gaps. The tandem concept has been demonstrated<sup>8,9</sup>, and has the advantage of higher efficiencies because lower band gap materials can be used, the photovoltages are additive<sup>6</sup>, and the two can be configured such that the higher band gap material is placed in front of the smaller one in order to most effectively use a broader spectrum of solar flux. It does, however, suffer the disadvantages that *two* different materials must be discovered and optimized. Also, the quantum yield is reduced by a factor of two as two photons are needed for the process of dual excitation, and the current will always be limited by the worst electrode<sup>10</sup>.

In addition to the reality that we must find semiconductors with appropriate band edge placements, we must also find material(s) with band gap(s) that can effectively utilize the sun to cause the excitation of electrons across the band gap(s)<sup>11</sup>. For the case of rutile TiO<sub>2</sub>, with a band gap of 3.0 eV, only 2 - 3% of the solar spectrum is energetic enough to create an appreciable photocurrent. Additionally, the position of the conduction band is, without an externally applied electric field, not suitable for unassisted water reduction as the overpotential for the HER is too small. This second detail has been discovered for undoped TiO<sub>2</sub> and it is now believed that the original photoelectrolysis experiments were not producing hydrogen gas in the first place but were instead just reducing contaminants in the electrolyte<sup>12</sup>. These were the fundamental

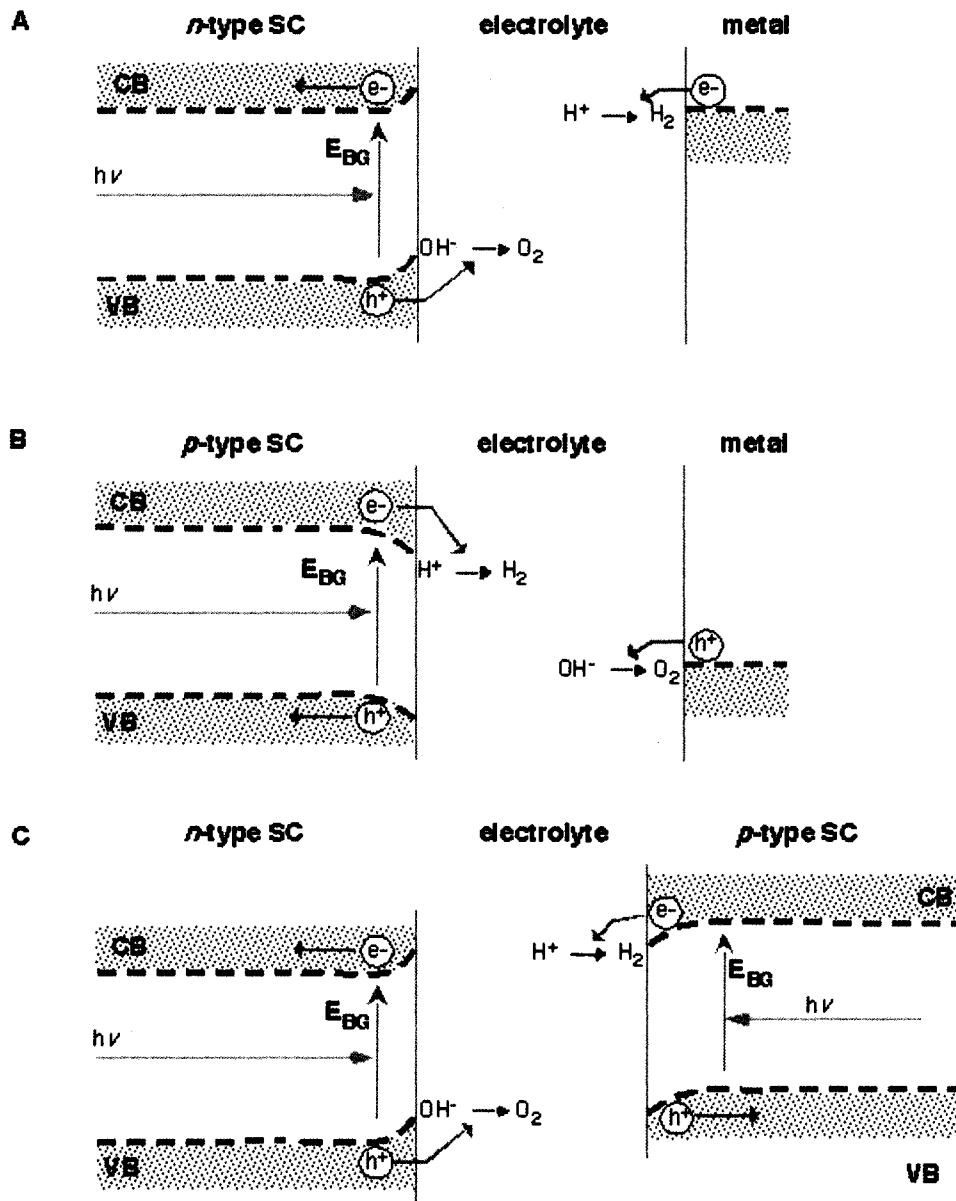


**Figure 1.3 Photoelectrolysis cell configurations for the different types of semiconductors and a tandem system.** In figure A, a single *n*-type photoelectrode system capable of independently carrying out the two half-reactions without “sacrificial reagents” is shown. In B, the analogous capability is shown for a *p*-type photoelectrode mechanism. In C, the two-electrode tandem concept is shown for which the larger bandgap material would be placed in front.

problems that quickly revealed themselves after the discoveries of Fujishima and Honda. Knowing that  $\text{TiO}_2$  alone would not meet the requirements of photoelectrolysis, the search began for more effective materials.

The positions of the valence and conduction band edges, relative to the redox potentials of water, for a variety of semiconductors that have been tried are shown in Figure 1.4. The characterization of the semiconductors relative to the reference levels indicated is the result of years of research, by several groups, for each semiconductor shown<sup>13-19</sup>. The first materials that were exhaustively studied were the perovskite structured  $\text{SrTiO}_3$ <sup>13-17</sup> and  $\text{BaTiO}_3$ <sup>13,18,19</sup>. As you can see from the graphic, both of these materials are better suited than  $\text{TiO}_2$  for water photoelectrolysis because their conduction band edges are more negative than the water reduction potential. Unfortunately, as is also true for  $\text{TiO}_2$ , their band gaps are so large that they also required a significant amount of UV light to create an appreciable photocurrent. Thus, while these early materials proved capable of splitting water while being illuminated with electromagnetic radiation, they were clearly incapable of efficiently using the sun to do it.

Smaller bandgap metal oxide semiconductors, notably  $\text{WO}_3$ <sup>20-23</sup>,  $\text{Fe}_2\text{O}_3$ <sup>24-29</sup>,  $\text{NiO}$ <sup>30,31</sup>, and  $\text{Cu}_2\text{O}$ <sup>32</sup>, were also studied at about this time in the history of semiconductor development. Although these materials are better suited for harvesting a larger percentage of the solar spectrum, their conduction band edge energies are not optimally positioned for the production of  $\text{H}_2(\text{g})$ <sup>33</sup>. They are also either poor conductors of electrons and/ or holes or are very prone to corrosion<sup>34</sup>. These same problems also haunt non-oxide semiconductors possessing near optimum band gaps<sup>34</sup> such as transition metal

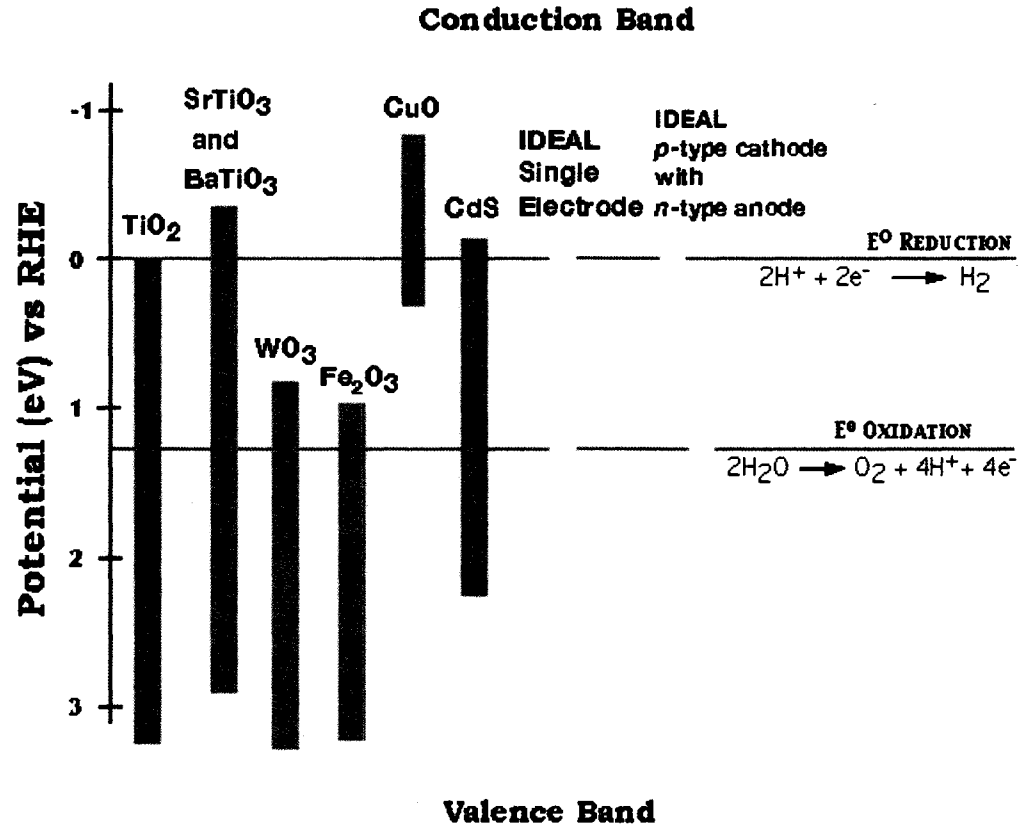


**Figure 1.4:** The bandgap characteristics for several known and ideal photoelectrolysis materials. Of the metal oxide systems shown, except for CuO, the valence band is primarily derived from O 2p orbitals- a fact that explains their relatively close valence band edges. Note that although CdS seems to match the characteristics of the ideal single material, it is unstable in aqueous electrolytes.

chalcogenides<sup>35-37</sup>, GaAs<sup>38</sup>, GaP<sup>39</sup>, and InP<sup>40</sup>. And so the conundrum was established within a few years of the original discovery: we can make materials with suitable band edge placements, conductivity, and corrosion resistance, or we can make materials that more effectively utilize the sun, but we cannot make materials that will do all of these things. This is the perplexing situation that still haunts us today.

Several clever ideas have surfaced to meet this daunting challenge, all with mixed success. One thing that has been realized for the systems mentioned above, and this can be

seen in Figure 1.3 with the exception of the *p*-type material CuO which functions more for the HER, is that the different metal oxide semiconductors show very little variation in the energy positions of the valence bands relative to the variation in the conduction bands. Thus, different metal oxides can be made, and they can all have different band gaps, but the position of the valence band edge remains fairly constant from semiconductor to semiconductor. This creates an unnecessarily large overpotential loss for oxygen generation, even if the hydrogen reduction is closely matched to the largely metal-derived conduction band, and so the resulting band gap is too large.

So the logical train of thought to this problem becomes clear: by some means the valence band edge must be higher for a material possessing an already appropriately placed (more negative than water's reduction potential) conduction band edge. This ideal material would then have a band gap that is appropriate for the solar spectrum and the efficient production of hydrogen gas can finally come to fruition. The theoretical basis for the creation of a raised valence band comes from the molecular orbital treatment of bonding in semiconductors<sup>7</sup>. When the transition metal and oxygen combine to form a semiconductor, the valence band is oxygen *2p* in nature because the electronegativity of oxygen is greater than that of the metal. The fact that the valence band is similar in energy for all semiconductors can be rationalized by the fact that they all have the oxygen anion in common. Conversely, the conduction band energy corresponds to that of the metal cation parent and this shows a larger variation from one metal oxide material to the next. However, if one introduces an additional metal into the semiconductor that has an

electronegativity greater than that of the parent metal, and it is obviously going to be less than that of oxygen, then it is possible that a filled valence band will be created that is more negative in energy (closer to the oxidation potential of water) than that of oxygen  $2p$ . This is the premise and hope of creating mixed metal oxides.

In rationalizing a suitable mixed metal material, it is often conceptually more straightforward to build up the conduction bands and valence bands separately from atomic orbitals of known energy<sup>7</sup>. With this in mind, perhaps the most promising metals to be included for mixed metal oxides are ones for which the conduction bands are derived from titanium compounds. In principle, it should then be possible to create a series of bands within the band gap of the parent titanium metal due to the mixing of atomic orbitals and so the valence band can be derived from the metal introduced into the  $\text{TiO}_2$  matrix instead of from oxygen  $2p$  orbitals. For example, the ions  $\text{Mn}^{2+}$ ,  $\text{Ni}^{2+}$ ,  $\text{Cr}^{3+}$ ,  $\text{Rh}^{3+}$ ,  $\text{V}^{4+}$ ,  $\text{Os}^{3+}$ ,  $\text{Sn}^{2+}$ ,  $\text{Sb}^{3+}$ ,  $\text{Pd}^{2+}$ , and  $\text{Pt}^{2+}$  all have  $d$  orbital energies that are more positive (further down an absolute scale) than the oxidation potential of water but more cathodic than that of oxygen's  $2p$  orbital<sup>7</sup>. And so, in theory at least, by combining these metals with titanium it should be possible to create a band gap that absorbs a large percentage of the solar spectrum and that is optimally positioned to electrolyze water. Along similar chains of logic, a potpourri of mixtures incorporating exotic metals have also been studied and some of them appear to be somewhat active. Compositions such as  $\text{LuRhO}_3$ <sup>41</sup>,  $\text{SrZr}_{0.25}\text{Ti}_{0.75}\text{O}_3$ <sup>7</sup>,  $\text{LaVaO}_3$ <sup>42</sup>,  $\text{K}_2\text{La}_2\text{Ti}_3\text{O}_{10}$ <sup>43</sup>, and  $\text{RbPb}_2\text{Nb}_3\text{O}_{10}$ <sup>44</sup>, have been reported to be viable photoelectrolytic systems relative to some traditional

semiconductors. Although an obvious problem with these types of systems is that they may be too expensive to produce on a large scale, the fact that other materials besides titanium-based compounds have demonstrated an ability to carry out aqueous photoreactions warrants an expanded materials study.

Two other obvious solutions to the problem of an overly large bandgap are to avoid oxide systems altogether (for example using GaAs, CdTe, GaP, CdS, etc.), or by raising the valence band edge by incorporating less electronegative anions (for example, S or N) into the lattice.

The first idea has produced materials that operate at remarkable efficiencies, at least initially. Cadmium and zinc chalcogenides as well as III-V materials have band gaps that are well suited for the solar spectrum and are photocatalytic for water splitting<sup>1,45,46</sup>. But the “Achilles heel” of these non-oxide based systems is that they are unstable in aqueous electrolytes<sup>46</sup>. Thermodynamic stability is assured only if the oxidation decomposition potential of the semiconductor lies below/ more positive than the valence band edge and the reduction decomposition potential lies above/ more negative than the conduction band edge<sup>47</sup>. Because the redox potentials for the decomposition reactions of these materials are generally within the band gap, and additionally because the decomposition reactions are kinetically favored due to the effects of surface states, these experiments typically yield the reduction of water to produce hydrogen at the expense of concomitantly preferentially oxidizing the electrode over the oxidation of water.

A relatively recent, and seemingly clever, idea is to alter the density of states distribution for the semiconductor by incorporating sulfur or nitrogen. A series of these compounds including  $\text{Sm}_2\text{Ti}_2\text{S}_2\text{O}_5$ <sup>48</sup>,  $\text{TaON}$ <sup>49</sup>,  $\text{Y}_2\text{Ta}_2\text{O}_5\text{N}_2$ <sup>50</sup>,  $\text{Ta}_3\text{N}_5$ <sup>51</sup>, and  $\text{LaTiO}_2\text{N}$ <sup>52,53</sup> have recently been created by several research groups in Japan and have been described in some prestigious journals. In all of these papers one can see a common set of experimental parameters. First, as supported by density functional theory simulations in each paper, the bottoms of the conduction bands consist of empty *d*- orbitals and the tops of the valence bands consist mainly of N 2*p* or S 3*p* orbitals depending upon the material. Thus, as one would *a priori* expect, the band gaps of these materials are smaller than that of the traditional large band gap metal oxides and so these materials are better suited for solar energy utilization. The resulting smaller band gaps, and their fortuitous positions relative the redox potentials of water, means that these materials could function as photoactive materials; and indeed H<sub>2</sub> and/ or O<sub>2</sub> is cited as being produced at quantum efficiencies even up to 30%<sup>49</sup>. Unfortunately, however, these systems are typically not reported to function without the presence of the “sacrificial reagents” mentioned earlier. It is this author’s belief that the sacrificial reagents are necessary to camouflage inherent oxidation or reduction decomposition reactions and that these materials ultimately have the same stability problems as the earlier materials that incorporated non-oxide anions.

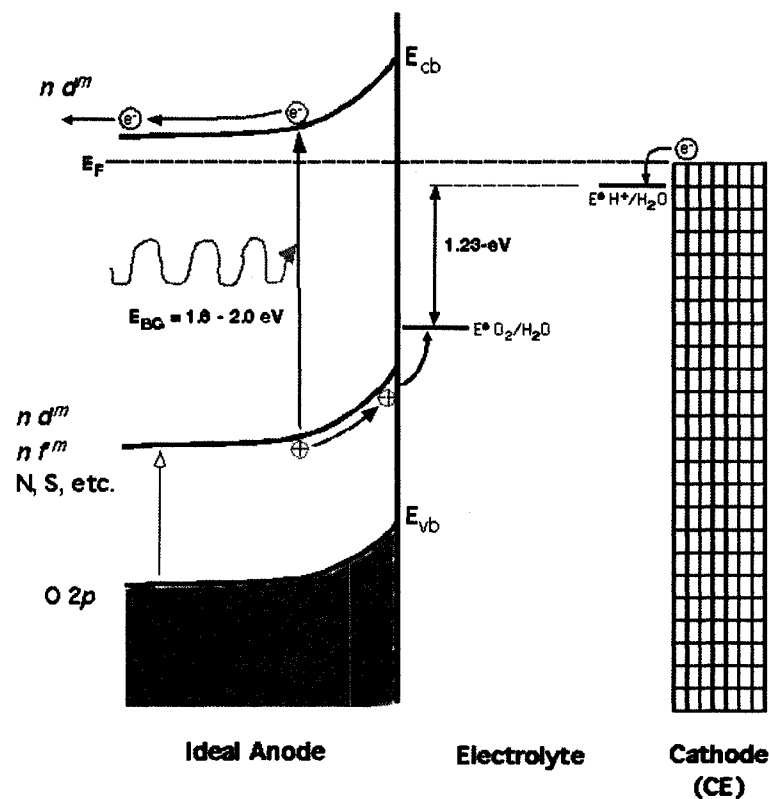


**Figure 1.5: Conceptual representation of a single-electrode photoelectrolysis system with a reduced band gap created by altering the valence band character within a large band gap parent matrix.** Shown in the figure is a “false valence band edge” created by introducing additional transition metal *d*- or *f*- orbitals and/ or additional anions such as S, N, P, etc. into a metal oxide photoelectrode. Doing so alters the density of states distribution relative to the pure metal oxide material such that the effective valence band edge is raised from the usual O 2*p* level by the qualitative amount shown in the hollow arrow. The result is an effectively smaller band gap that can more efficiently split water with visible light as the overpotential for oxygen generation is reduced.

Among all of the theoretical discussions given so far, the Parkinson research group believes that best possible means to create a metal oxide capable of water splitting using visible light would be to derive both the valence and conduction band from a mixture of metals as such a system would have a lower band gap with the added bonus of metal oxide stability.

### 1.3 Combinatorial Production and Screening of New Materials

Materials derived from multiple elements are often needed when a special property needs to be optimized. For example, the highest transition temperature superconductor contains four metals ( $\text{HgBa}_2\text{CaCu}_2\text{O}_{6+\delta}$ ). A new cathode material for the next generation of solid oxide fuel cells is derived from multiple metals,  $\text{Ba}_{0.5}\text{Sr}_{0.5}\text{Co}_{0.8}\text{Fe}_{0.2}\text{O}_{3-d}$ , and has demonstrated operation at much more reasonable temperatures than typically needed and with higher power output<sup>54</sup>. New materials for lithium batteries<sup>55</sup>, and CO oxidation catalysts<sup>56</sup>, among others, are all recent multi-component discoveries showing enhanced performance over earlier materials made from a smaller number of materials. This is not to imply that one can haphazardly combine elements and expect special results, but it does suggest that each element plays a specific role in the overall functionality of these special materials and that the right amount of the right elements can create a synergy between each of these roles.

Perhaps elements suited for each role in the photoelectrolysis of water can be choreographed into a functional device. The traditional parent materials of wide-band gap metal oxide semiconductors (for example, Ti, Sn, W, Ta, and Nb) are needed for structure and stability. It will be necessary to incorporate colored transition metals into those materials to serve the role of visible light absorbers and indeed work done in the past has already shown that the visible response of wide band gap semiconductors can be enhanced by such additions<sup>57,58</sup>. Yet another material may help to suppress electron-hole

recombination within the material by acting as charge compensator or a surface state modifier, a role that has also been shown to increase the efficiency of the same materials mentioned above<sup>57,59</sup>. Finally, it may be necessary to sprinkle the surface of the electrode with catalytic materials, or provide small amounts in the bulk, such as Pt, Pd, Ir, Ru, or, even better yet, a cheap element such as Ni<sup>60-62</sup>.

In the final analysis we see that “the photocatalyst that will revolutionize the world” has not yet been found. But armed with the insight that the catalyst must fulfill the multiple requirements of visible wavelength response, stability, and band edge placement, it is easy to reason that the catalyst will be composed of several elements. Unfortunately, and in spite of such simple logic as that used above and even with the sophisticated computer models and high processing speeds available today, it is impossible to deduce *a priori* the identity and stoichiometry of the mixed metal oxide system that will fulfill all of these requirements. We are left with no choice but to discover the system empirically and so a rapid and high-throughput method to test the representative properties needs to be developed.

The basic premise behind a combinatorial search is to produce as many combinations as possible, both in the number of materials and the stoichiometry of each mixture, and rapidly screen them for the property of interest. It can be extremely difficult for a scientist, especially when trained to believe in his or her abilities to solve problems largely by deductive reasoning, to believe that such a seemingly chaotic endeavor could ever produce anything useful.

The application of rapid throughput production and screening has revealed invaluable applications within the pharmaceutical industry but has also been extended to solid state systems to discover new luminescent materials<sup>63-65</sup>, gate dielectrics<sup>66</sup>, and fuel cell catalysts<sup>67,68</sup>. The properties of all of these new materials discovered by combinatorial means appear to be more promising than the previous materials used for the same purpose.

In a similar vain, perhaps thousands of mixed metal oxides for water splitting will have to be produced and tested before a working material is found. The McFarland group has already embarked on the search by generating and screening a small library of binary oxides using an automated array-based electrodeposition and electrochemical scanning system<sup>69,70</sup>. Through this approach they have identified an optimal tungsten-molybdenum composition. The group has also synthesized electrocatalyst libraries using electron beam evaporation<sup>71</sup>. Unfortunately, the methods used to create their libraries are both very time-consuming and very expensive and only binary mixtures have thus far been produced.

A much cheaper and faster approach to materials deposition is to use ink jet printers. Ink jet printing of materials for combinatorial searches has also been applied to organic electronic materials<sup>72</sup> and even protein<sup>73</sup> and nucleic acid arrays<sup>74</sup>. Ink jet printing also offers the added advantages that gradients of compositions can easily be created instead of array-based samples and that an unlimited number of materials can be mixed.

We have combined the speed and versatility of ink jet printing with a customized electrochemical screening system to search for potentially promising metal oxide photocatalysts. We have printed gradients of one, two, three, or four materials onto transparent conductive substrates and have screened them for photoactivity using visible light. From common and inexpensive common electrochemical equipment we have already screened hundreds of compositions. The system that we have designed and implemented appears to be more versatile, inexpensive, and faster than any others that have been designed for the same purpose. It also appears to be the most realistic as we are only testing the materials as they would practically be used in any real system; we do not introduce any sacrificial reagents into our electrolyte and we use incident radiation that is energetically representative of the actual sun.

Although their techniques differ from ours, other groups have applied the idea of combinatorial screening for a similar quest. The Mallouk group has screened thousands of ternary mixtures containing Ir, Pt, Ru, Os, and/ or Rh for water oxidation or oxygen reduction using robotic plotters and fluorescent indicator molecules<sup>75,76</sup>. They have shown that the compositions they have revealed are indeed more efficient than what was previously recorded and they have also tested them against corrosion<sup>77</sup>. Eric McFarland and coworkers have tested a vast array of tungsten-based ternary mixed metal oxides for hydrogen production<sup>78</sup> and they have extended the idea to the discovery and optimization of luminescent materials<sup>79</sup>. The pre-screening of a huge number of platinum based catalysts for polymer fuel cells has also been carried out<sup>80</sup>.

The optimal mixture that we and other groups seek might have a different metal or metals for each of the necessary water photoelectrolysis roles. For instance, one of the metals might reduce water. Another might oxidize water. Yet another metal might prevent against corrosion and/ or facilitate electrical conductivity. The final metal might be needed for light absorption. Figuring out the right combination of particular metals might produce a mixture that will do everything needed for efficient water splitting. And although a couple of other groups are using combinatorial concepts, we all have different techniques and approaches that should be tried because the quest is too important to be attempted by only a few.

## References

- (1) Khaselev, O.; Turner, J. A. *Science* **1998**, *280*, 425-427.
- (2) Fujishima, A.; Honda, K. *Bulletin of the Chemical Society of Japan* **1971**, *44*, 1148-1150.
- (3) Fujishima, A.; Honda, K. *Nature* **1972**, *238*, 37-38.
- (4) Huheey, J. E.; Keiter, E. A.; Keiter, R. L. *Inorganic Chemistry*; Fourth ed.; HarperCollins College Publishers: New York, NY, 1993.
- (5) Hummel, R. E. *Electronic Properties of Materials*; 3rd ed. ed.; Springer-Verlag: New York, 2001.
- (6) Rajeshwar, K. *J. Appl. Electrochem.* **2007**, *In Print*.
- (7) Bin-Daar, G.; Dare-Edwards, M. P.; Goodenough, J. B.; Hamnett, A. *Journal of the Chemical Society, Faraday Trans.* **1983**, *79*, 1199-1213.
- (8) Nozik, A. J. *Appl. Phys. Lett.* **1977**, *30*, 567-569.
- (9) Jarrett, H. S.; Sleight, A. W.; Kung, H. H.; Gilson, J. L. *J. Appl. Phys* **1980**, *51*, 3916-3925.
- (10) Bolton, J. R.; Strickler, S. J.; Connolly, J. S. *Nature* **1985**, *316*, 495-500.
- (11) Rauh, R. D.; Buzby, J. M.; Reise, T. F.; Alkaitis, S. A. *Journal of Physical Chemistry* **1979**, *83*, 2221-2226.
- (12) Ming X. Tan, P. E. L., Sonbinh T. Nguyen, Janet T. Kesselman, Colby E. Stanton, and Nathan S. Lewis *Progress in Inorganic Chemistry* **1994**, *41*, 21-144.
- (13) Kung, H.; Jarrett, H.; Sleight, A.; Ferretti, A. *Journal of Applied Physics* **1977**, *48*, 2463-2469.
- (14) Wrighton, M. S.; Ellis, A. B.; Wolczanski, P. T.; Morse, D. L.; Abrahamson, H. B.; Ginley, D. S. *Journal of the American Chemical Society* **1976**, *98*, 2774-2779.
- (15) Mavroides, J. G. *Semiconductor Liquid-Junction Solar Cells*; The Electrochemical Society: NJ, 1977; Vol. 77-3.
- (16) Watanabe, I.; Matsumoto, Y.; Sato, E. *J. Electroanal. Chem.* **1982**, *133*, 359-366.

- (17) Mavroides, J. G.; Kafalas, J. A.; Kolesar, D. F. *Applied Physics Letters* **1978**, *28*, 241.
- (18) Nasby, R. D.; Quinn, R. K. *Materials Research Bulletin* **1976**, *11*, 985-992.
- (19) Kennedy, J. H.; Karl W. Freese, J. *J. Electrochem. Soc.* **1976**, *123*, 1683-1686.
- (20) Butler, M.; Nasby, R.; Quinn, R. *Solid State Commun.* **1976**, *19*, 1011.
- (21) Butler, M. A. *Journal of Applied Physics* **1977**, *48*, 1914.
- (22) Berak, J. M.; Sienko, M. J. *J. Solid State Chem.* **1970**, *2*, 109.
- (23) Wang, H.; Lindgren, T.; He, J.; Hagfeldt, A.; Lindquist, S.-E. *J. Phys. Chem. B* **2000**, *104*, 5686-5696.
- (24) Hardee, K.; Bard, A. *J. Electrochem. Soc.* **1976**, *123*, 1024.
- (25) Nasby, R.; Quinn, R. *Materials Research Bulletin* **1976**, *11*, 985.
- (26) Kennedy, J. H.; K. W. Frese, J. *J. Electrochem. Soc.* **1978**, *125*, 709.
- (27) McGregor, K. G.; Calvin, M.; Otvos, J. W. *J. Appl. Phys.* **1979**, *50*, 369.
- (28) Frelein, R. A.; Bard, A. J. *J. Electrochem. Soc.* **1979**, *126*, 1892.
- (29) Wilhelm, S. M.; Yun, K. S.; Ballenger, L. W.; Hackerman, N. *J. Electrochem. Soc.* **1979**, *126*, 419-424.
- (30) Dare-Edwards, M. P.; Goodenough, J. B.; Hammett, A.; Nicholson, N. D. *J. Chem. Soc., Faraday Trans.* **1981**, *77*, 643.
- (31) Koffyberg, F. P.; Benko, F. A. *J. Electrochem. Soc.* **1981**, *128*, 2476.
- (32) Nikitine, S.; Zielinger, J. P.; Coret, A.; Zouaghi, M. *Phys. Lett.* **1965**, *18*, 105.
- (33) Goodenough, J. B.; Hammett, A.; Dare-Edwards, M. P.; Campet, G.; Wright, R. D. *Surface Science* **1980**, *101*, 531-540.
- (34) Harris, L. A.; Wilson, R. H. *Annu. Rev. Mater. Sci.* **1978**, *8*, 99.

- (35) Hodes, G.; Fonash, S. T.; Heller, A.; Miller, B. *Advances in Electrochemistry and Electrochemical Engineering*; Wiley-Interscience: New York, 1985.
- (36) Rajeshwar, K.; Singh, P.; Dubow, J. *Electrochim. Acta* **1978**, *23*, 1117.
- (37) Fan, F. R. F.; White, H. S.; Wheeler, B. L.; Bard, A. J. *J. Electrochem. Soc.* **1980**, *127*, 518.
- (38) Heller, A. *Acc. Chem. Res.* **1981**, *14*, 154.
- (39) Strehlow, W. H.; Cook, E. L. *J. Phys. Chem. Ref. Data* **1973**, *2*, 163.
- (40) Levy-Clement, C.; Heller, A.; Bonner, W. A.; Parkinson, B. A. *ibid.* **1982**, *129*, 1701.
- (41) Jarrett, H. S.; Sleight, A. W.; Kung, H. H.; Gillson, J. L. *J. Appl. Phys.* **1980**, *51*.
- (42) Guruswamy, V.; Keillor, P.; Campbell, G. L.; Bockris, J. O. M. *Solar Energy Materials and Solar Cells* **1980**, *4*, 11-30.
- (43) Takata, T.; Shinohara, K.; Tanaka, A.; Hara, M.; Kondo, J.; Domen, K. *Journal of Photochemistry and Photobiology* **1997**, *106*, 45-49.
- (44) Yoshimura, J.; Ebina, Y.; Kondo, J.; Domen, K. *J. Phys. Chem.* **1993**, *97*, 1970-1973.
- (45) De, G. C.; Roy, A. M.; Bhattacharya, S. S. *Int. J. Hydrogen Energy* **1996**, *21*, 19-23.
- (46) Rauh, R. D.; Buzby, J. M.; Reise, T. F.; Alkaitis, S. A. *J. Phys. Chem.* **1979**, *83*, 2221-2226.
- (47) Gerischer, H. *Faraday Disc.* **1980**, *70*, 1A-8B.
- (48) Ishikawa, A.; Takata, T.; Kondo, J.; Hara, M.; Kobayashi, H.; Domen, K. *J. Am. Chem. Soc.* **2002**, *124*, 13547-13553.
- (49) Hitoki, G.; Takata, T.; Kondo, J. N.; Hara, M.; Kobayashi, H.; Domen, K. *Chem. Commun.* **2002**, 1698-1699.
- (50) Liu, M.; You, W.; Lei, Z.; Zhou, G.; Yang, J.; Wu, G.; Ma, G.; Luan, G.; Takata, T.; Hara, M.; Domen, K.; Li, C. *Chem. Commun.* **2004**, 2192-2193.

- (51) Hitoki, G.; Ishikawa, A.; Takata, T.; Kondo, J.; Hara, M.; Domen, K. *Chem. Lett.* **2002**, *1*, 736-737.
- (52) Kasahara, A.; Nukumizu, K.; Hitoki, G.; Takata, T.; Kondo, J.; Hara, M.; Kobayashi, H.; Domen, K. *J. Phys. Chem. A* **2002**, *106*, 6750-6753.
- (53) Kasahara, A.; Nukumizu, K.; Takata, T.; Kondo, J.; Hara, M.; Kobayashi, H.; Domen, K. *J. Phys. Chem. B* **2003**, *107*, 791-797.
- (54) Shao, Z.; Haile, S. *Nature* **2004**, *431*, 170-173.
- (55) Kalyani, P.; Kalaiselvi, N.; Renganthan, N. G.; Raghavan, M. *Mat. Res. Bull.* **2004**, *39*, 41-54.
- (56) Kirsten, G.; Maier, W. F. *Appl. Surf. Sci.* **2004**, *223*, 87-101.
- (57) Ghosh, A. K.; Maruska, P. *J. Electrochem. Soc.* **1977**, *124*, 1516-1522.
- (58) Kato, H.; Kudo, A. *J. Phys. Chem. B* **2002**, *106*, 5029-5034.
- (59) Ishii, T.; Kato, H.; Kudo, A. *J. Photochem. and Photobiol. A* **2004**, *163*, 181-186.
- (60) Tsuji, I.; Kato, H.; Kobayashi, H.; Kudo, A. *J. Am. Chem. Soc.* **2004**, *126*, 13406-13413.
- (61) Zou, Z.; Ye, J.; Sayama, K.; Arakawa, H. *Nature* **2001**, *414*, 625-627.
- (62) Kudo, A.; Kato, H. *Chem. Phys. Lett.* **2000**, *331*, 373-377.
- (63) Wang, J.; Yoo, Y.; Gao, C.; Takeuchi, I.; Sun, X.; Chang, H.; Xiang, X.-D.; Schultz, P. G. *Science* **1998**, *279*, 1712-1714.
- (64) Danielson, E.; Devenney, M.; Giaquinta, D. M.; Golden, J. H.; Haushalter, R. C.; McFarland, E. W.; Poojary, D. M.; Reaves, C. M.; Weinberg, W. H.; Wu, X. D. *Science* **1998**, *279*, 837-839.
- (65) Danielson, E.; Golden, J. H.; McFarland, E. W.; Reaves, C. M.; Weinberg, W. H.; Wu, X. D. *Nature* **1997**, *389*, 944-948.
- (66) Dover, R. B. v.; Schneemeyer, L. F.; Fleming, R. M. *Nature* **1998**, *392*, 162-164.
- (67) Reddington, E.; Sapienza, A.; Gurau, B.; Viswanathan, R.; Sarangapeni, S.; Smotkin, E. S.; Mallouk, T. E. *Science* **1998**, *280*, 1735.

- (68) Cong, P.; Doolen, R. D.; Fan, Q.; Giaquinta, D. M.; Guan, S.; McFarland, E. W.; Poojary, D.; Self, K.; Turner, H. W.; Weinberg, W. H. *Angew. Chem. Int. Ed.* **1999**, *38*, 484-488.
- (69) Baeck, S. H.; Jaramillo, T. F.; Brandli, C.; McFarland, E. W. *J. Comb. Chem.* **2002**, *4*, 563-568.
- (70) Baeck, S.-H.; Jaramillo, T. F.; Jeong, D. H.; McFarland, E. W. *Chem. Commun.* **2004**, 390-391.
- (71) Jaramillo, T. J.; Ivanovskaya, A.; McFarland, E. W. *J. Comb. Chem.* **2002**, *4*, 17-22.
- (72) Sirringhaus, H.; Kawase, T.; Friend, R. H.; Shimoda, T.; Inbasekaran, M.; Wu, W.; Woo, E. P. *Science* **2000**, *290*, 2123-2126.
- (73) MacBeath, G.; Schreiber, S. L. *Science* **2000**, *289*, 1760-1763.
- (74) Calvert, P. *Chem. Mater.* **2001**, *13*, 3299-3305.
- (75) Morris, N.; Mallouk, T. E. *J. Am. Chem. Soc.* **2002**, *127*, 11114-11121.
- (76) Chen, G.; Bare, S. R.; Mallouk, T. E. *Journal of the Electrochem. Soc.* **2002**, *149*, A1092-A1099.
- (77) Chen, G.; Delafuente, D.; Sarangapani, S.; Mallouk, T. E. *Catalysis Today* **2001**, *67*, 341-355.
- (78) Jaramillo, T. F.; Ivanoskaya, A.; McFarland, E. *J. Comb. Chem.* **2002**, *4*, 17-22.
- (79) Danielson, E.; Golden, J.; McFarland, E.; Reaves, C.; Weinberg, W. H.; Wu, X. D. *Nature* **1997**, *389*, 944-948.
- (80) TamizhMani, G.; Dodelet, J. P.; Guay, D.; Dignard-Bailey, L. *Journal of Electroanalytical Chemistry* **1998**, *444*, 121-125.

## **Chapter 2: Development of a Protocol for High Throughput Deposition, Screening, and Bulk Production of New Materials for Photoelectrolysis**

### **2.1 Preface**

In this chapter I outline the development of the methodology that was implemented for the results obtained in Chapter 3. The purpose of this chapter is to provide a more thorough account of the background, procedures, equipment, and rationale for the research. Also, I discuss our work on spray pyrolysis- a technique that may prove useful in the future as a bulk deposition method but for metal oxide films discovered by our search.

## 2.2 Introduction to the Development of High Throughput Production and Screening of Materials

This project began as an idea of materials production by inkjet printing shown by the diagram in Figure 2.1, and, although the experimental details of the high throughput production process have ultimately proven to be quite simple, the discovery and refinement of them was certainly not. We began this unfunded project with the vision that metal oxide precursors, initially in the form of aqueous nitrate salts, would be mixed by ink jetting in the same way that a printer mixes different colors. The goal was to print the precursors onto a transparent conductive substrate, pyrolyze them to produce metal oxides, and correlate the photoactivity to promising compositions by measuring the photocurrent produced while a laser rastered over the surface of the materials.

Because the identity of the “ideal” material for photoelectrolysis is unknown and is beyond theoretical prediction, it is necessary to discover it empirically. Because each of the material’s functional roles needs to be choreographed into a single functional device, it is logical to assume that the functional material may be composed of a mixture of three, four, or maybe even more materials. To mix  $N$  materials three at a time there are  $N! / 3!(N-3)!$  different permutations. If we loosely identify 45 possible candidates to fit the roles shown in Figure 2.1 that equates to 14,200 combinations to be produced and tested. To mix  $N$  materials four at a time there are  $N! / 4!(N-4)!$  different permutations, which equates to 149,000 possible combinations for those elements. However, some

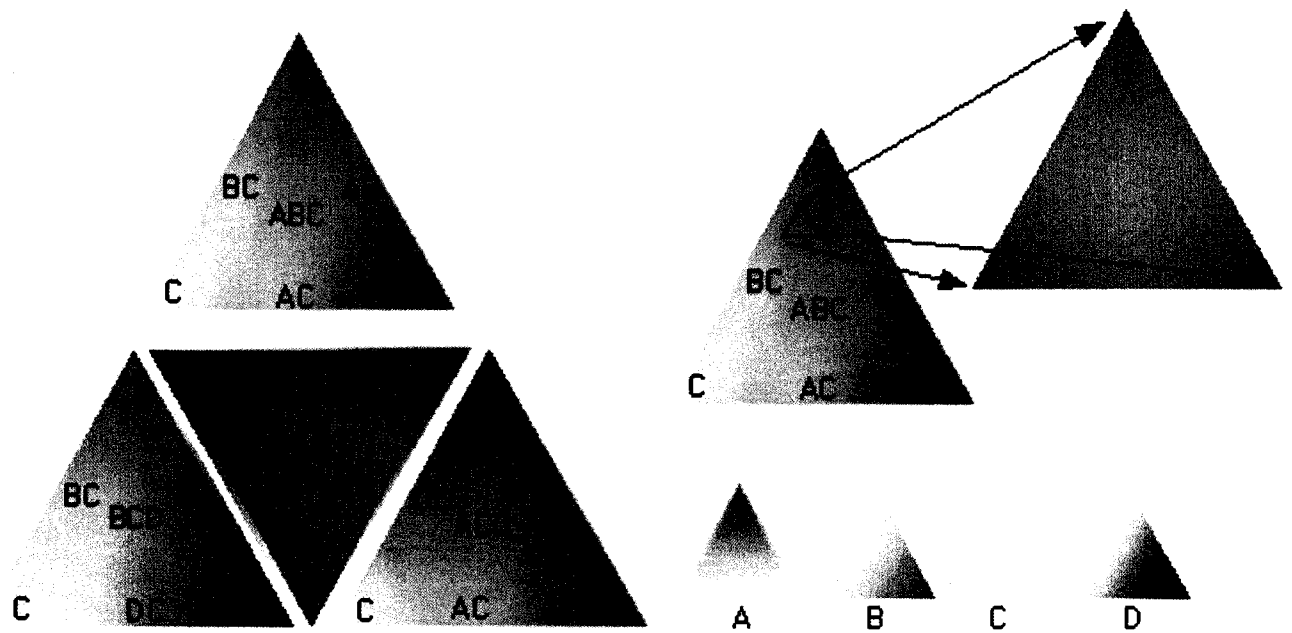


**Figure 2.1: Original design of material mixtures to be printed and screened.** This template, derived from the “unfolded tetrahedron” approach designed by Thomas Mallouk et al.<sup>1,2</sup>, was the cornerstone of thought for designing the combinatorial production and screening project. The concept was to mix four metals three at a time in triangles that would roughly correspond to ternary phase diagrams (although the printer driver software doesn’t utilize linear gradients typical of traditional phase diagrams). When a promising composition was found, for example the small triangle inset of the ABC ternary mixture, the printing gradients could be adjusted to expand that region of the ternary phase diagram and the necessary number of iterations could be performed until the best mixture was found.

combinations could be excluded because it probably would not make sense to, for example, mix only large band gap structural materials and expect visible light absorption. Nonetheless, rapid production and testing is obviously needed to even begin such a daunting endeavor. We developed a beautiful proof of concept for how this might be achieved over the course of my first two years of graduate school.

## 2.3 Early Experimental History

The first task was to find an appropriate substrate to print on. Primarily because we had samples already in the lab, indium tin oxide (ITO) was tested first. We also believed at the time that the metal oxides would work best if deposited onto a high surface area, nanoporous “Gratzel” scaffold of  $\text{TiO}_2$  and so a colloidal suspension of this material was applied by the “doctor blading” technique<sup>3</sup>. To test the efficacy of this architecture, several of these porous electrodes were immersed in various aqueous metal nitrate solutions, annealed, and tested by cyclic voltammetry in a three-electrode cell at acidic, neutral, and basic pH values while being irradiated with a 150-W Xe arc lamp. Unfortunately, after background subtraction, no appreciable photocurrent was detected for any of the samples tested.

It was believed that the  $\text{TiO}_2$  layers produced by the above technique were too thick and so photogenerated charge carriers could not diffuse to the back contact before recombination. So we researched a technique to deposit thin films of  $\text{TiO}_2$  by the sol-gel technique<sup>4</sup> and spin coated a partially hydrolyzed titanium isopropoxide in ethanol solution onto both the ITO and onto 3.0-mm thick 8- $\Omega$  fluorine-doped tin oxide ( $\text{SnO}_2\text{:F}$

or FTO) conductive and transparent glass substrates. As in the nanoparticulate layers, the thin films were immersed into metal nitrate solutions and annealed. Again, no appreciable photocurrent was detected.

To deduce whether it was the substrate or the  $\text{TiO}_2$  layer that was causing the lack of photocurrent, an ITO substrate was compared to a  $\text{SnO}_2\text{:F}$  substrate by sensitizing a layer of  $\text{TiO}_2$  nanoparticles deposited on each with the ruthenium-based organometallic dye commonly called N3. Cyclic voltammetry was performed on these dye-sensitized films in solutions containing tetrabutyl ammonium fluoride (TBAF) supporting electrolyte and hydroquinone redox mediator in acetonitrile. The best photocurrent was measured using the FTO substrate and so it was chosen for future studies. Unfortunately, after numerous attempts over the past several years, we have never gotten any appreciable photocurrent-voltage response from ANY metal oxide precursor that has been printed or dip-coated onto either  $\text{TiO}_2$  or the high surface area transparent conducting oxide antimony tin oxide provided by the Lian group of Emory University (we speculate that this maybe due to improper positioning of the conduction bands for charge transfer to occur). Ultimately, it was decided to go with a substrate preparation protocol of simply soaking the as-received FTO substrates in a saturated KOH in isopropanol base bath for at least thirty minutes, a recommendation from Jeremy Nelson in Dr. Mike Elliott's group. After soaking, the substrates are rinsed with copious amounts of distilled water and ethanol.

The scanning system shown in Figure 2.2 was the most conceptually complex aspect of this project, as I had no prior significant computer programming or photoelectrochemistry experience. The overall purpose of the scanning system is to raster a laser with a pair of galvanometer mirrors over the printed materials immersed in an aqueous electrolyte and produce a two-dimensional “image” of photocurrent “pixels”. The two mirrors move separately in response to an applied analog voltage and it was decided that Labview software was best suited for this purpose. After a short time of learning about the software, it was possible to control the mirrors to move the laser in two dimensions by first stepping the laser in quantized increments across the sample from left to right, then move the laser down in the vertical direction by an incremental amount and back over to the left side of the sample, and then repeating for the desired number of repetitions.

The photocurrent at each step is recorded by an analog-to-digital data acquisition (DAQ) board made by National Instruments installed on a PC. For the majority of experiments, it is connected in series to a lock-in amplifier and potentiostat, although the lock-in amplifier can be removed and the current can be measured as DC if the magnitude of the signal (a voltage which is proportional to the current) is sufficiently large. When the current is very small, however, a technique known as “phase-sensitive detection” must be employed. Briefly, the laser illuminates the sample at a frequency set either by chopping or, if the laser has the capability, by modulation with a function

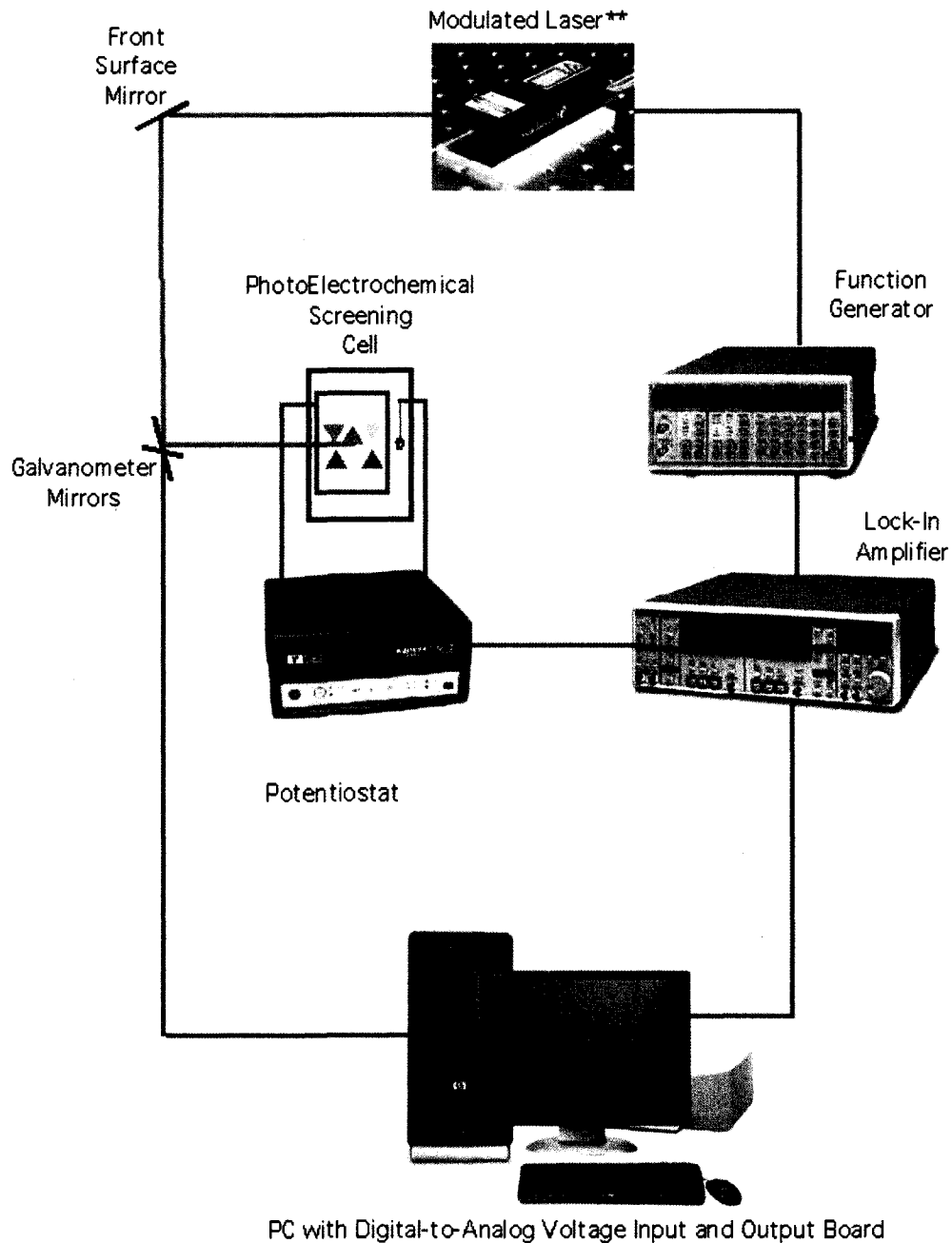


**Figure 2.2:** The photoelectrochemical screening system used throughout this project. The front surface mirror is placed on an optical rail within the system as three lasers (633-nm, 532-nm, and 477-nm) are arranged in parallel and the mirror can be moved to any one of them. See the text for a more complete description of the other pieces of equipment.

generator and the current is detected at that same frequency. In this way, one can isolate the signal of interest from the electrical noise common to conventional AC power usage as long as the frequencies are different (which should be the case as long as integer values of 30 Hz are avoided). The potentiostat, used to record the current and convert it to an analog voltage, is connected in a two-electrode configuration by short-circuiting the reference and counter electrode inputs to a platinum wire or basket. The potentiostat can also be used to apply an external bias to the sample, something that can be useful when screening for materials of a certain doping type.

I was quickly limited in my progress in the development of this protocol by the problem of recording the photocurrent after each quantized horizontal step and then generating an array of photocurrent values corresponding to each step. With some outside assistance, this problem was overcome and the program is currently designed so that the Cartesian start and end points of an approximately 2" x 2" scan are completely adjustable, and typically a 140 x 140 array of photocurrent values is produced. A false color image that displays photocurrent as a function of Cartesian position can then be obtained by opening the data array with the ImageJ software program. In these images, shown frequently throughout this thesis, the photocurrent values relative to other materials that are screened on the same film are displayed as a false color images. The color table is set so that highest photocurrent in the two-dimensional array appears as the brightest (white or yellow) spot in the image and the lowest photocurrent (and, in some cases, opposite in sign) pixels are displayed as dark blue or black.

Through our collaboration with the Hewlett-Packard corporation, we obtained an HP Deskjet 1220C printer that had been modified for materials printing by raising the rail on which the printer cartridges slides to effectively increase the printhead-to-substrate distance so that our rather thick glass substrate could be pulled through the printer. It was decided early on that a printable solution of iron (III) nitrate would be optimized first because it is a colored solution that allows one to see if it is actually printing and because of some reports, most notably from the Somorjai group, that  $\alpha\text{-Fe}_2\text{O}_3$  was a stable visible band gap material that had shown promise as a water splitting material<sup>5-8</sup>.

The HP printer that we use is of the thermal ink jet type. Briefly, this type of printer operates due to the action of resistive elements that are placed within the printhead. Passage of a current through these resistive elements near the nozzle openings causes rapid heating ( $>100\text{ }^\circ\text{C}/\mu\text{s}$ ) and vapor explosion of the solution at the nozzle. Picoliter volume droplets burst out of the nozzles at a frequency corresponding to the electrical signal set by the printer driver. There are two different types of cartridges for this particular printer, each with their own particular requirements with respect to “ink” viscosity and surface tension, backpressure within the cartridge chamber, inkjetting characteristics, etc. After more than four months of continuous failures it was decided that the color cartridges have a much more complex set of requirements and would only be useful for the three metals loaded into them to be printed together. The black cartridges were much more promising, albeit inconsistent until we consulted with some specialists at HP to derive “ink” formulations that would consistently print. All of our

metal oxide precursors for the HP black cartridges are soluble salts and they are prepared at a concentration of 0.35 M in the presence of 0.6 M  $\text{NH}_4\text{NO}_3$  and 0.015 M  $\text{HNO}_3$ . The purpose of the ammonium nitrate is to provide an additional force to the thermal ink jetting process where the rapid thermal heating of the fluid by resistors within the printhead causes the formation of drops. The ammonium nitrate also rapidly detonates at the high temperatures, effectively causing the droplets to burst out of the nozzles. The acid is necessary to prevent the formation of metal hydroxide precipitates that can clog the nozzles. The solution is injected into empty black printer cartridges through a syringe filter. A large clip is used to establish backpressure within the cartridge when it is sealed, and the printer's cleaning cycle is run before each printing. The cartridges can be used repeatedly up to several months after they were originally made provided they are stored in a "humidor" (a dessicator that is filled with water at the bottom to help prevent the drying, and subsequent clogging, of nozzles) and a special tape provided by HP is cut and pasted onto the printhead.

The solutions can then be printed onto the substrates after they have been taped to a standard sheet of printer paper. Because only the black cartridges can be used, grayscale triangular gradient patterns are used for each material. The three triangles are overlaid by printing one material, exchanging the cartridge, and then printing the next materials over the top by positioning the triangles to print over the same area of the substrate. The printed metal patterns are fired in a tube furnace at 500 °C anywhere from 2 to 24 hours without any noticeable change in measured material properties (at least for

the materials that have been extensively studied thus far). The metal nitrates are easily pyrolyzed to metal oxides at this temperature, an assertion that has been confirmed with both EDS and X-ray diffraction. After cooling, scanning is typically performed in either 0.1 M or 0.5 M NaOH (a solution that we decided to use after multiple accounts and personal observation that the majority of metal oxides are most stable in alkaline solution) although any aqueous or organic solvent system may be used. One of the most exciting days of my graduate school experience to date was when I finally obtained a false color image of a printed metal oxide scanned with the system that we designed. Over the course of my graduate school career, this protocol has been used by myself, another graduate student, and several undergraduate students to produce and test over 500 ternary or quaternary mixtures. An extensive database of these mixtures has also been created, using FileMaker<sup>®</sup> software. It is available to the public through our group server and is discussed in more detail in Appendix B.

## 2.4 Spray Pyrolysis

After we had established a protocol for ink jet printing metal oxide precursors, we quickly noticed that the photocurrents resulting from our as-produced materials were always very small and certainly beyond the sensitivity of a direct-current measurement. We believe that this is most likely because the majority of light passes through, or is possibly scattered, without being harvested. And so soon after the printing procedures were in place, we began to address the question of how best to create more efficient, large area photoelectrodes once a promising composition was discovered.

Researchers within the Grätzel group have made progress in addressing this problem by producing high surface area nanoparticulate morphologies, with  $\text{TiO}_2$ <sup>3</sup> as well as  $\alpha\text{-Fe}_2\text{O}_3$ <sup>9-11</sup>, that can much more effectively harvest visible light relative to flat films while still producing grain sizes small enough to shuttle charge carriers to the back contact before photoexcited electron-hole recombination occurs. For water cleavage, the best reported efficiencies (a solar-to-chemical conversion efficiency of 2.1%, based on the heat of hydrogen combustion, when used in a tandem configuration with a dye-sensitized solar cell) are achieved when producing the nanostructured morphologies typical of Figure 2.3 for which the thickness of the perpendicularly aligned sheets is between 15 and 25 nm. This optimal morphology appears to be a critical parameter, as all samples produced by different methods have similar thicknesses, pure  $\alpha\text{-Fe}_2\text{O}_3$  crystal structures as determined by X-ray diffraction, and identical optical characteristics as

examined by UV-visible and Raman spectra. The authors argue that this particular grain size, and orientation, of the leaf-shaped sheets is best suited for the short hole diffusion length of only a few nanometers. This particular morphology affords immediate transfer of holes to the electrolyte, before recombination occurs, while still shuttling electrons, with a longer diffusion length, to the back contact. The group has been able to achieve this morphology by using ultrasonic spray pyrolysis of their iron precursor solutions<sup>11</sup>, with even further improvements observed after doping with silicon<sup>9</sup>.

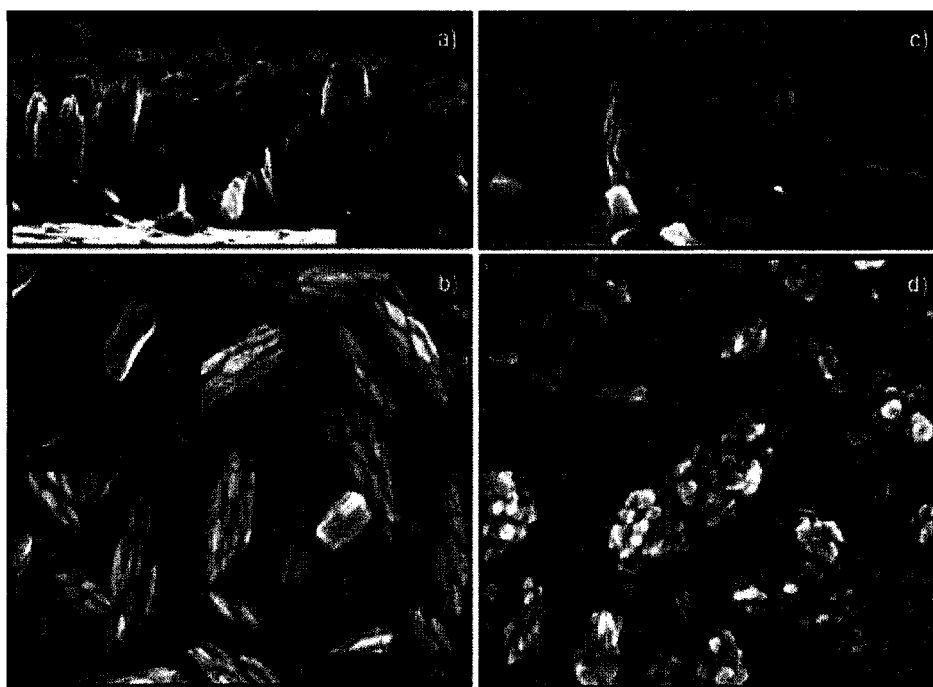


**Figure 2.3: Typical high resolution- scanning electron microscope images of Si-doped  $\alpha$ -Fe<sub>2</sub>O<sub>3</sub> films on SnO<sub>2</sub>: F obtained by the Grätzel group<sup>9</sup>.** (a) is the side view for a film prepared by ultrasonic spray pyrolysis, (b) is the top view. (c,d) are the side and top views for films prepared by atmospheric pressure chemical vapor deposition. The insets of (b) and (d) are to show the grains obtained by the two methods without Si doping.

It was primarily because of the results presented in references 9-11 that we were motivated to create our own spray pyrolysis system with the hopes of achieving similar success with any newly discovered compound revealed by our search. An invaluable collaboration with Dr. Calvin Curtis of the National Renewable Energy Laboratory, and Elden Burke with the CSU Chemistry Department, led to the design of the station shown in Figure 2.4, which does lack the feature of ultrasonication of the precursor used by the Grätzel group<sup>9</sup>. In this design, cartridge heaters installed into a copper block are used to heat the FTO substrate that is held inside of a square cut out of the top aluminum plate. A thermocouple is also implanted into the block to provide feedback to the temperature controller which ramps the temperature to a point set by the user (typically 400 °C for the experiments we performed). An airbrush, manufactured by the Badger Corporation, sprays the precursor solution in small drops (usually at a concentration of 0.05 M in ethanol) onto the substrate by aspiration and mixing with nitrogen gas. Because of the temperature of the substrate, the precursor is expected to decompose upon contact.

Several methods have been tried to achieve uniform coverage, with the best results obtained by clamping the airbrush at a fixed distance from the substrate in a perpendicular orientation, taping the fluid cap and plunger head at fixed positions, and opening the nitrogen gas tank regulator to the desired pressure and allowing the solution to spray for the desired length of time. In principle as well as in practice, it can be advantageous to spray for short bursts of time (15 seconds or less), turn off the spraying

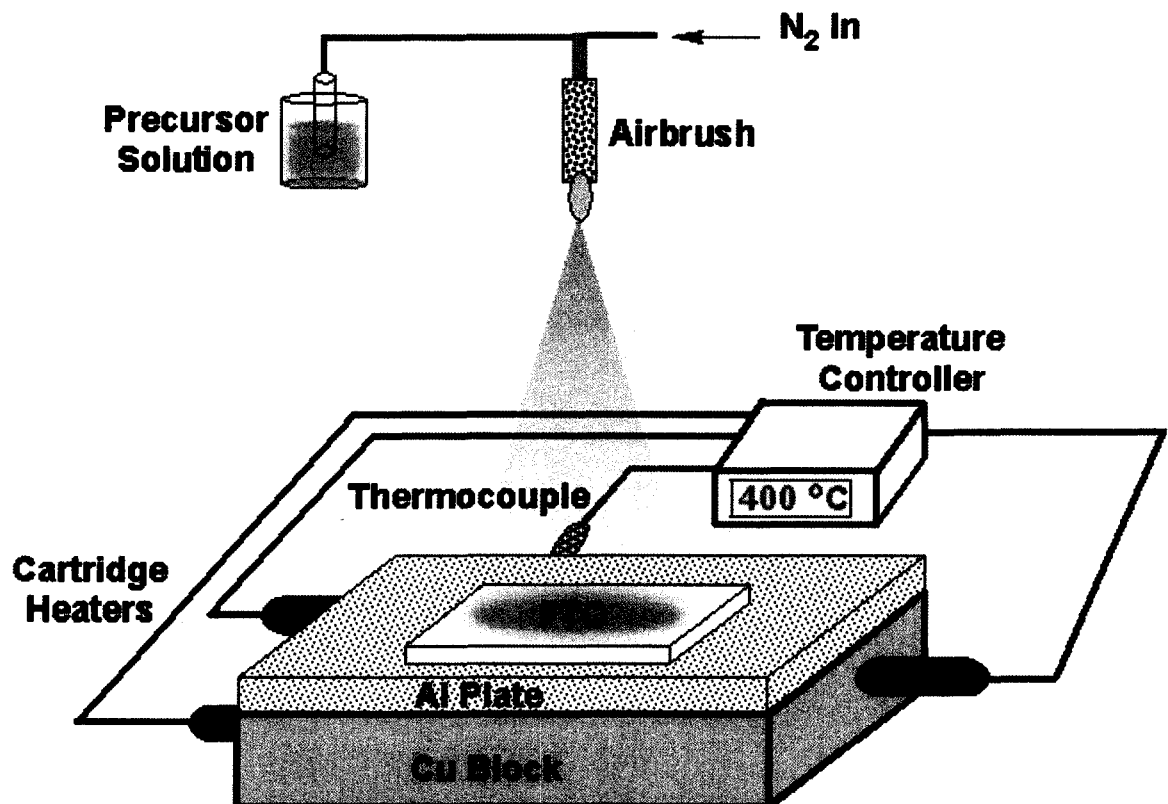
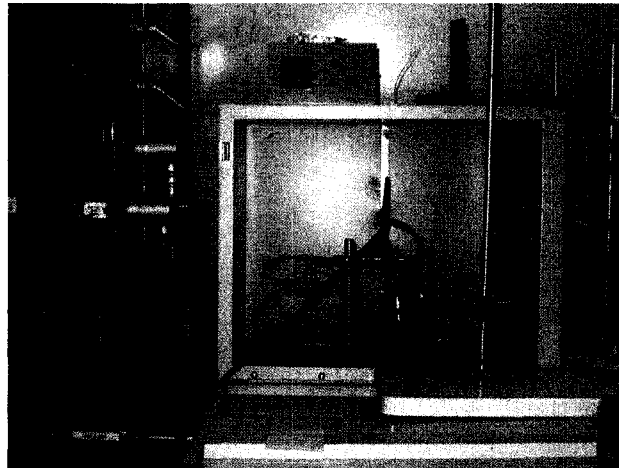


**Figure 2.4: Current configuration for a simple spray pyrolysis system.** (Top) Photograph from the front view of the station described in the text. (Bottom) Schematic to illustrate the working parts and engineering of the configuration.

by turning the regulator valve, wait for approximately 60-s in order for the substrate temperature to equilibrate and to ensure complete decomposition of the precursor, and then apply additional layers in the same fashion until the desired volume of solution has been deposited. Conceptually, this would ensure complete decomposition of the precursor as the substrate temperature would not be expected to significantly drop if spraying layers. However, *when depositing smaller volumes of material*, I have not seen this method produce drastically different results than those obtained by simply decreasing the spray deposition rate by using a smaller fluid cap rotation and spraying continuously until the desired volume of solution has been deposited.

The most uniform and efficient photoelectrodes produced by spray pyrolysis are shown in figures 2.5 and 2.6. The solution deposited in both cases was a mixture iron (III) acetylacetonate, titanium (IV) isopropoxide, and aluminum (III) chloride hexahydrate in ethanol, a mixture that was optimized by the Augustynski group for spray pyrolysis of water oxidation catalysts<sup>10,12</sup>. The solution was prepared to a total concentration of 0.05 M with, in atomic percentages, 94% Fe, 6%Ti, and 1% Al<sup>10</sup>. From the SEM images shown in Figure 2.6, we can see that the shape of the material looks somewhat similar to that obtained by the Grätzel group as shown above, although the grain sizes appear to be quite a bit larger. Before this process was studied further, we obtained a research grade printer and our priorities changed to the work shown in Chapter 4 of this thesis.

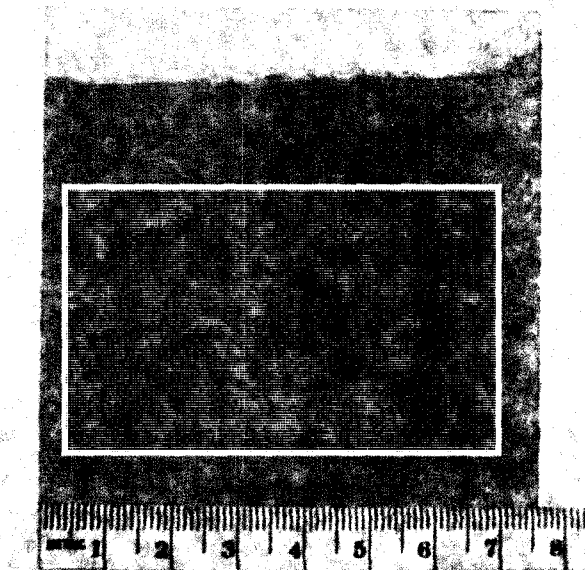


**Figure 2.5: Example of the uniformity capabilities once the spray pyrolysis technique had been optimized.** (Top) Photograph of a film deposited by continuous spraying of a solution made from Fe, Al, and Ti precursors described in the text. A metric ruler is shown below to show the size of the film. (Bottom) False-color photocurrent map of the boxed area of the film shown. The average incident-photon-to-current conversion efficiency (IPCE) was 0.19% with a standard deviation of less than 10% in 0.1-M NaOH with a 532-nm laser at +0.5-V vs SCE.

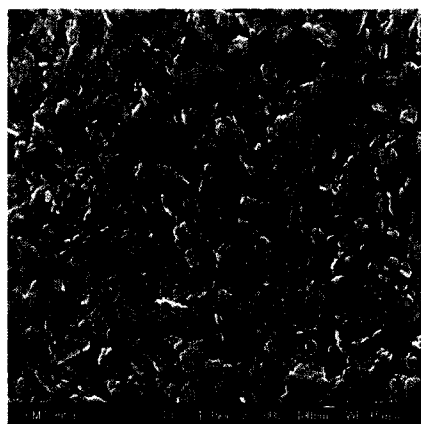
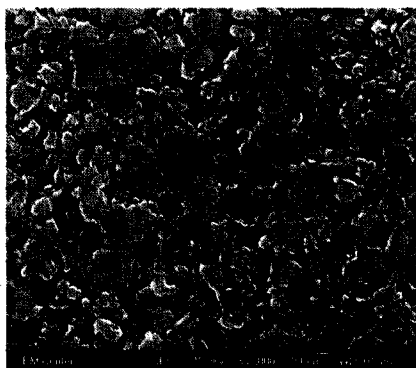
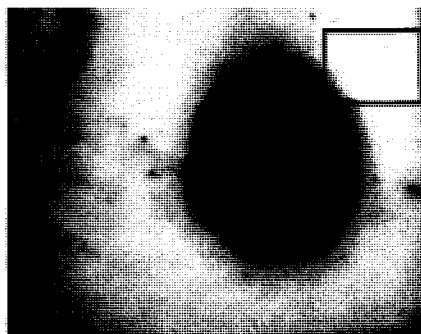


**Figure 2.6: The most efficient area of a metal oxide film deposited by spray pyrolysis.** (Top) False color photocurrent scan of a film made using the recipe described in figure 2.5. The volume of solution sprayed was greater in this case and so the dark halo is presumably a result of the film being too thick in that area that was directly beneath the airbrush. The average IPCE for the area outlined by the box is  $1.94 \times 10^{-4}$  with a standard deviation of less than 5%. (Middle) Annotated SEM image for a spot within the box showing varying grain sizes in the hundreds of nanometers, but an overall shape approaching the desired architecture. (Bottom) Another spot within the box showing similar characteristics.

It is this author's belief, nonetheless, that a much higher efficiency could be measured for these water oxidation materials. Because they are often tested in a short-circuited two-electrode configuration, the current may be limited by the water reduction half-reaction occurring at the counter electrode and so the true capabilities of the material may be underestimated. To address this problem, an additional electrolyte could be added (e.g. an electron scavenger as discussed in chapter 1) or an additional, highly efficient photoactive material with HOMO-LUMO levels appropriate for water reduction could be connected in series to make a tandem configuration so that the current is assured to be limited by the working electrode. In cases where a reference electrode was not used, the efficiencies might also be higher if measured in a three-electrode system.

## **Acknowledgements**

Dr. Michael Kramer of the CSU Mathematics Department is acknowledged for providing helpful guidance in developing the Labview program used for screening. Dr. David Schut with the Hewlett Packard Corporation needs to be recognized for revealing (somewhat) proprietary insights about inkjet formulations that made printing not only possible, but also consistent. Substrate advice and training was received from Mike Scott and Jeremy Nelson, members of the Elliott group at Colorado State. Finally, Dr. Calvin Curtis with the National Renewable Energy Laboratory is acknowledged for sharing his expertise on spray pyrolysis and we are grateful to Elden Burke for machining the necessary components.

## References

- (1) Reddington, E.; Sapienza, A.; Gurau, B.; Viswanathan, R.; Sarangapeni, S.; Smotkin, E. S.; Mallouk, T. E. *Science* **1998**, *280*, 1735.
- (2) Morris, N. D.; Mallouk, T. E. *J. Am. Chem. Soc.* **2002**, *124*, 11114-11121.
- (3) Nazeeruddin, M. K.; Kay, A.; Rodicio, I.; Humphry-Baker, R.; Muller, E.; Liska, P.; Vlachopoulos, N.; Gratzel, M. *J. Am. Chem. Soc.* **1993**, *115*, 6382-6390.
- (4) Smestad, G. P.; Spiekermann, S.; Kowalik, J.; Grant, C. D.; Schwartzberg, A. M.; Zhang, J.; Tolbert, L. M.; Moons, E. *Sol. Energy Mater. Sol. Cells* **2003**, *76*, 85-105.
- (5) Khan, S. U. M.; Akikusa, J. *J. Phys. Chem. B* **1999**, *103*, 7184-7189.
- (6) Wilhelm, S. M.; Yun, K. S.; Ballenger, L. W.; Hackerman, N. J. *Electrochem. Soc.* **1979**, *126*, 419-424.
- (7) Ingler, W. B.; Baltrus, J. P.; Khan, S. U. M. *J. Am. Chem. Soc.* **2004**, *126*, 10238-10239.
- (8) Leygraf, C.; Henderwerk, M.; Somorjai, G. A. *J. Phys. Chem.* **1982**, *86*, 4484-4485.
- (9) Cesar, I.; Kay, A.; Martinez, J. A. G.; Gratzel, M. *J. Am. Chem. Soc.* **2006**, *128*, 4582-4583.
- (10) Sartoretti, C. J.; Alexander, B. D.; Solarska, R.; Rutkowska, I. A.; Augustynski, J.; Cerny, R. *J. Phys. Chem. B* **2005**, *109*, 13685-13692.
- (11) Duret, A.; Gratzel, M. *J. Phys. Chem. B* **2005**, *109*, 17184-17191.
- (12) Sartoretti, C. J.; Ulmann, M.; Alexander, B. D.; Augustynski, J.; Weidenkaff, A. *Chem. Phys. Lett.* **2003**, *376*, 194-200.

## **Chapter 3: A Combinatorial Approach to Identification of Catalysts for the Photoelectrolysis of Water**

### **3.1 Preface**

The work in this chapter was published in the ACS journal Chemistry of Materials **2005**, *17*, 4318-4324. All data shown were obtained by me, except the XRD which was obtained by Dr. Sandeep Kohli. The printer was provided by the Hewlett Packard Corporation, as were some invaluable conversations about making solutions that were printable.

## **3.2 Abstract**

A new simple and high-throughput combinatorial method to search for materials capable of the photoelectrolysis of water is presented. Ink jet printing is used to pattern metal oxide precursors (simple nitrate salts) onto conductive glass substrates. Subsequent pyrolysis yields electrodes with patterns of metal oxide compositions that, when immersed in an electrolyte, are easily screened for photoelectrolysis activity using a scanning laser system. Some promising metal oxide compositions were identified using this approach.

### 3.3 Introduction

Hydrogen obtained from renewable energy will be the fuel of choice either when fossil fuels become depleted or when the environmental consequences of burning fossil fuels are no longer acceptable. Direct photoelectrolysis of water using solar energy is the ideal method for producing hydrogen from a renewable, inexpensive and abundant raw material. The first steps towards this goal were taken more than thirty years ago by Fujishima and Honda when they demonstrated that crystalline rutile ( $\text{TiO}_2$ ) electrodes, when illuminated with UV light, produced hydrogen from water without decomposition of the electrode<sup>1,2</sup>. Despite the promising start, there has been little progress towards an affordable, stable and efficient method to photoelectrolyze water. Efficient photoelectrolysis of water has been achieved using expensive single crystal III-V multijunction electrodes<sup>3</sup>, but their long-term stability and high cost remain problematic.

Due mainly to their inherent stability, semiconducting oxides are strong candidate materials for the ability to efficiently photoelectrolyze water. The ideal single metal oxide photoanode or photocathode material will have a bandgap around 1.6 - 2.0 eV. A photoelectrolysis system could also be efficient by coupling both a *p*-type and an *n*-type material to drive water photoreduction and photooxidation respectively, as was originally described by Nozik et al<sup>4</sup>, where band gaps in the range of 0.8 to 1.2 eV for each material would be optimum. This approach, where annihilation of minority carriers at the ohmic contact generates the extra voltage or driving force for photoelectrolysis, also lowers the theoretical quantum yield by a factor of two. However, this approach does have the

advantage that two smaller band gap materials could be used, thereby extending the utilization of the solar spectrum into the near-infrared. The disadvantages of this approach are that the currents in the two electrodes must be matched for optimum efficiency and that two materials, rather than just one, need to be discovered and optimized.

A material will also need to be affordable and stable under illumination in aqueous electrolytes and be catalytic for the evolution of oxygen or hydrogen from water in order to minimize overpotential losses. The material must also have conduction and valence band energies negative of the water reduction potential and positive of the water oxidation potential, respectively. No material that meets these conditions has yet been identified. However, such a material will likely be composed of multiple metals; each of which contributes to the required special properties. High temperature superconductivity is a good example of a special property requiring multicomponent materials. The oxide with the highest known transition temperature contains four metals ( $\text{HgBa}_2\text{CaCu}_2\text{O}_{6+\delta}$ ,  $T_c = 125\text{K}$ ). Since our present theoretical knowledge is insufficient to *a priori* calculate the behavior of such complex systems, empirical methods will be necessary to identify the best material for efficient water photoelectrolysis. Thousands, or perhaps hundreds of thousands, of mixed metal oxide photocatalyst compositions may need to be produced and tested for efficiency and corrosion resistance until an effective material is discovered.

The recent development of combinatorial methods provides tools to speed the discovery process when a large number of candidate materials need to be synthesized and

screened for the property of interest<sup>5</sup>. Combinatorial methods have been applied to optimize oxide materials for use as phosphors<sup>6-9</sup>, gate dielectrics<sup>10</sup> and fuel cell catalysts<sup>11,12</sup>. The MacFarland group has demonstrated the electrochemical deposition of metal oxide compositions using robotics to plate and screen individually created binary oxide materials and have looked at water photooxidation catalysts using multiplexed photoelectrochemical cells<sup>13</sup>.

Herein we report a novel high throughput combinatorial search strategy to identify multicomponent metal oxide materials with suitable band gaps and band positions for water photoelectrolysis operating as either a photoanode or a photocathode. Our combinatorial search strategy uses ink jet printing of overlapping patterns of soluble metal nitrate salts, as metal oxide precursors, onto a conductive glass substrate. Metal nitrates decompose to form metal oxides, oxygen, and NO<sub>2</sub> by heating at relatively low temperatures.

The low cost, speed and versatility of ink jet printing have made it attractive for combinatorial searches for fuel cell catalysts<sup>5</sup>, organic device combinations<sup>14</sup> and biomaterials<sup>15</sup>. We feel that our approach has several major advantages over previous combinatorial search strategies for identifying oxide photoelectrolysis materials. First, we create a variation of composition across our samples to produce a plethora of compositions in each experiment. Second, we are not limited to materials that can be electrodeposited, and third, we do not need custom engineered robotic devices but are using simple, off-the-shelf items for both creating and screening our libraries. Finally,

we are directly testing our compositions under the same conditions to be used in a realistic photoelectrolysis device (e.g. we do not use sacrificial reagents in our electrolyte and we illuminate our samples with visible wavelength radiation).

### 3.4 Experimental Section

Fluorine-doped tin oxide coated glass (8-ΩR, 3.0 mm thickness) was obtained from Pilkington industries and cut into 3" x 3" squares. The glass was soaked in an isopropyl alcohol/ KOH base bath for a minimum of 30 minutes followed by rinsing with copious amounts of distilled water and ethanol.  $\text{Fe}(\text{NO}_3)_3$ ,  $\text{Cu}(\text{NO}_3)_2$ ,  $\text{CsNO}_3$ ,  $\text{Nd}(\text{NO}_3)_3$ ,  $\text{Co}(\text{NO}_3)_2$ , and  $\text{Al}(\text{NO}_3)_3$  were obtained from Fisher Scientific (Fe), Strem (Cu and Nd), Alfa Aesar (Co and Cs) and Baker Chemical (Al) and all were analytical reagent grade. Solutions of the appropriate metal nitrate salt (0.35 M) with  $\text{NH}_4\text{NO}_3$  (0.6 M) and  $\text{HNO}_3$  (0.015 M) were injected into empty Hewlett Packard 1220C DeskJet black ink jet printer cartridges. The cartridges were then manually primed using a commercially available kit from ABC Printer Repair and the cleaning cycle was run on each cartridge to ensure that printing was uniform. The  $\text{SnO}_2:\text{F}$  glass was taped to a piece of printer paper and patterns of nitrate salts were then sequentially printed for each metal. The metal salt solutions were often reprinted up to three times to achieve the appropriate metal oxide thickness.

The printed metal patterns were then fired in air at 500 °C for 24 hours in a ThermoLyne Type 1300 furnace to decompose the metal nitrates into metal oxides. The metal oxide coated conductive glass was then connected as the working electrode in a

two-electrode configuration with a Princeton Applied Research 174A Potentiostat. A loop of Pt wire around the perimeter of the printed substrate served as both the reference and counter electrodes. A 0.500 M NaOH solution was the electrolyte. A positive or negative bias was applied to screen for photoanode or photocathode materials respectively. The sample was irradiated with a ~2mm unfocused laser beam (514.5-nm Ar<sup>+</sup> laser (Ion Laser Technology model 400), 532 nm doubled YAG laser (BWN-532-20-E), 632.8 nm (Melles Griot 05-LHR-991 HeNe laser)). The resulting photocurrent from the photoelectrochemical cell was measured with a Stanford Research Systems SR530 Model Lock-In Amplifier and a PTI model OC4000 chopper operating at 13-Hz. A program written with Labview software controlled the rastering of the laser over a selected region of the substrate by applying stepwise voltages to a two-mirror galvanometer (CLS-200 from Intelite, Inc.) and recording the subsequent photocurrent at each pixel (typically resulting in a 140 x 140 matrix for each scan). X-ray diffraction was done using the Cu K- $\alpha$  line from a Bruker D8 Discover glancing angle x-ray diffractometer. Photocurrent spectroscopy was done using an apparatus that has been described previously<sup>16</sup>.

### **3.5 Results and Discussion**

Our first task was to optimize printing procedures by printing thickness gradients of a single component and measuring the photocurrent. Figure 3.1A shows a simple rectangular gradient pattern that was printed onto SnO<sub>2</sub>:F coated glass with 0.35M Fe(NO<sub>3</sub>)<sub>3</sub> ·  $\alpha$ -Fe<sub>2</sub>O<sub>3</sub>

has previously been shown to have some activity for water photooxidation and so it was a logical material for our initial studies<sup>17,18</sup>. The simple printed pattern was printed over once, twice, and three times to determine the number of times to overprint the metal nitrate solution in order to optimize the photocurrent signal. Thin film X-ray diffraction was used to verify that  $\alpha\text{-Fe}_2\text{O}_3$  is the phase produced by pyrolyzing ferric nitrate at 500 °C. A photograph of the substrate after printing and firing at 500 °C is shown in Figure 3.1B. The electrode/ substrate was then immersed in a 0.5M NaOH solution with an applied bias of 0.5 V with respect to the platinum counter electrode in the same solution. A false color photocurrent scan, produced by scanning the 514 nm line of a chopped Ar ion laser over the immersed substrate, is shown in Figure 3.1C. The figure demonstrates that if the coating is too thin, then not much of the incident light is absorbed (1X scan). If the coating is too thick, the photogenerated carriers are created too far away from the metal oxide/solution interface and recombine before they can be transported to the interface (far end of 3X scan). The photocurrent scan reveals that the optimum thickness occurs about two-thirds of the way up on the pattern that was been overprinted three times. Figure 3.1D shows an average photocurrent cross section for the region enclosed by the white rectangle in Figure 3.1C where the maximum in the photocurrent response is clearly seen 50-60 pixels from the end. This corresponds to an average thickness of about 12 nm of  $\alpha\text{-Fe}_2\text{O}_3$ .

Once the concentration of solution in the ink jet cartridges and the number of overprints was optimized, we turned our attention to printing ternary and quaternary composition gradients. A significant advantage of printing the continuous composition gradients is that the effects of doping small amounts of different elements into a particular oxide can be simultaneously examined over a large range of doping levels by controlling the printing gradient, a useful property to examine as small amounts of added dopants have

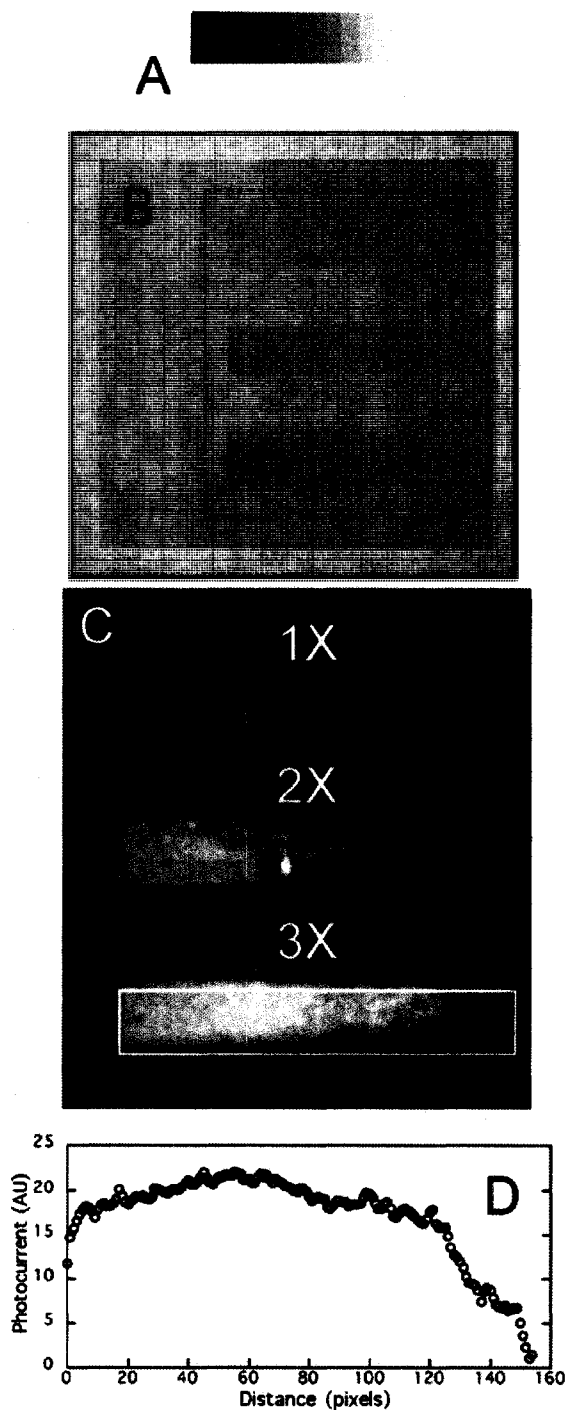


**Figure 3.1. Overprinting a gradient pattern to optimize the metal oxide thickness.**  
 A. Rectangular gray scale gradient used to template the printing of the  $\alpha\text{-Fe}_2\text{O}_3$  precursor.  
 B. Photograph of the gradient pattern in A that was printed one, two, and three times on  $\text{SnO}_2\text{:F}$  coated glass (graph paper underneath has 1 cm large squares).  
 C. A false color photocurrent image of the region inside the dotted rectangle of B displaying IPCE values generated by scanning a 514.5 nm laser over the surface in a 0.5 M NaOH solution.  
 D. Line profile obtained by averaging the IPCE values along the length of the rectangle outlined over the 3X printed gradient.

been shown to dramatically influence the photoactivity of metal oxide photoelectrodes<sup>19,20</sup>. Linear, exponential, or other gradient patterns can be used depending on the drawing program and the printer driver software. However, it must be kept in mind that the gradients produced by an ink jet printer are produced by variation in the density of individual ink dots and so are not continuous on a microscopic scale. Overprinting several times with a less concentrated solution, as was done in the thickness study discussed above, is one way to make the printed pattern more continuous, although regions of very light printing may have widely separated individual dots. Upon heating, the nitrate salts will first dehydrate and then melt and decompose, resulting in mixing of the elements.

Our initial high throughput approach involves ink jet printing and screening four metals, three at a time, in four triangular patterns that represent the faces of an unfolded tetrahedron (Figure 3.2A) akin to the pattern used by Mallouk et al for printing mixtures of precious metals for screening as fuel cell catalysts<sup>5</sup>. The unfolded tetrahedron pattern represents the four ternary faces of the three-dimensional tetrahedral four-component phase diagram.

The number of metal combinations to be screened can be enormous (there are at least 60 potentially useable metals in the periodic table resulting in  $>60^3$  or 216,000 combinations for three components and  $>60^4$  or almost 13 million for four). To reduce the number of combinations, we use some intuitive guidance to aid in selecting promising combinations. We can very loosely classify metals into one of four categories according to their potential role in a photoelectrode material; structural (i.e. Ti, W, Zr, Ta, Si, Mo, Nb, Hf, In, Sn, Ga, Y, Sc), light absorbing (i.e. Fe, Cr, V, Co, Mn, Ni, Cu, and some rare

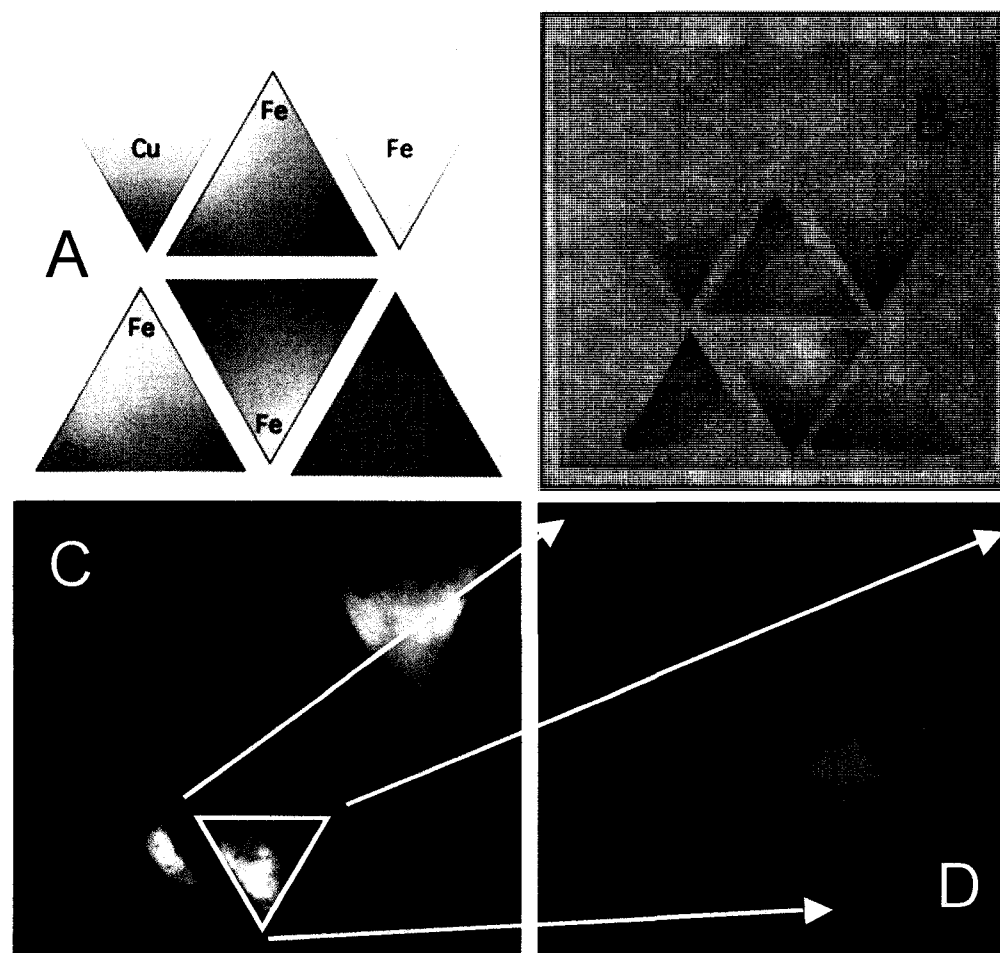


**Figure 3.2. Printing and screening a four-metals-three-at-a-time pattern and a compositional zoom for the Fe-Cs-Nd-Cu system.** A. False color template showing the positions and gradients used for printing the four metal precursor solutions. B. Photograph of the printed and fired film. Note the triangular internal standards of  $\alpha\text{-Fe}_2\text{O}_3$  and CuO (upper right and left, respectively) with thickness gradients (bottom to top) that are used as internal standards. C. False color photocurrent image of the film shown in B using 514.5-nm illumination under a 0.5 V bias in 0.5 M NaOH solution. D. Photocurrent scan at 514.5-nm of a triangular composition zoom in on the brightest area of the Fe-Cs-Nd triangle shown in C that has a maximum IPCE value approximately twice that of the  $\alpha\text{-Fe}_2\text{O}_3$  internal standard (smaller triangle to the lower right).

earths such as Ce), catalytic (i.e. Ru, Rh, Pd, Pt, Ir, Os, Re, Ni) and ionic charge compensators (i.e. Ca, Sr, Ba, Mg, Zn, Cd, Li, Na, K, Rb, Cs)\*. This intuitive guidance greatly reduces the number of possible combinations. For instance, it is not productive to try combinations of all high bandgap materials (i.e. Ti-Zr-Si-Y oxides) since none of the elemental oxides absorb visible light and it is unlikely that the produced mixtures will either. It may, however, be useful to select multiple light absorbing metals that have complementary absorption bands to produce a material with better spectral overlap with the solar spectrum.

To date we have printed and screened dozens of the four-metal-three-at-a-time patterns discussed above. Most show no or very little photoresponse. Figure 3.2B shows a photograph taken after twice printing the pattern in 3.2A of Fe, Cu, Nd and Cs and firing the film. Additional small triangles of  $\alpha$ -Fe<sub>2</sub>O<sub>3</sub> and CuO were printed in the upper left and upper right respectively with their thickness decreasing from bottom to top. We use these triangular areas as internal standards for the photocurrent screening since these materials show some *n*-type photoactivity for water oxidation ( $\alpha$ -Fe<sub>2</sub>O<sub>3</sub>) and *p*-type activity for water reduction (CuO)<sup>21</sup>. The  $\alpha$ -Fe<sub>2</sub>O<sub>3</sub> triangle “lights up” in screening scans with a positive applied bias (Figure 3.2C upper left triangle) whereas the CuO triangle “lights up” with a negative applied bias (not shown in this figure). The internal standards provide a check that our processing conditions are reproducible from run-to-run and serve

---

\* We are purposely avoiding toxic metals such as Pb, Tl, Cd and Hg since we envision large-scale implementation of any discovered photocatalyst and we want to avoid the potentially damaging environmental consequences of using these metals.

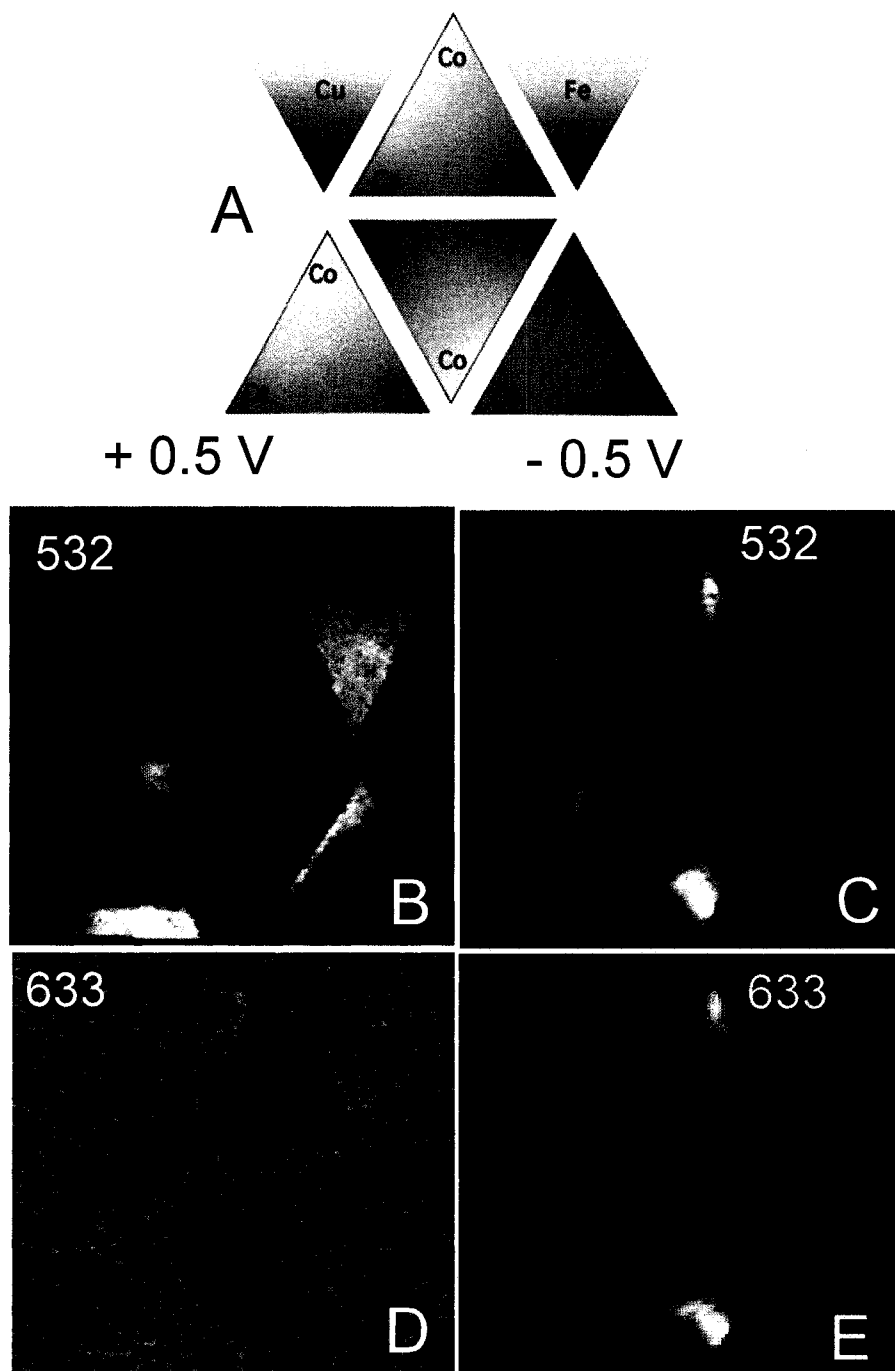
as a benchmark for the photoactivity of the mixed phases printed in the main triangles. Areas showing considerably higher photocurrent, relative to the internal standards, then represent promising new compositions.

Figure 3.2C shows the results of screening the combination of Fe, Cu, Nd and Cs with the same conditions used in Figure 3.1. We add a small electrical bias ( $\pm 0.5V$ ) to reveal compounds that are effective at light absorption and charge separation but may not be especially catalytic towards water oxidation (positive bias) or reduction (negative bias). The photocurrent scan (Figure 3.2C) reveals that adding Cs and Nd to  $Fe_2O_3$  produces a composition with a photoresponse almost two times higher than the pure  $\alpha$ - $Fe_2O_3$  internal standards (central triangle of Figure 3.2C). The Fe, Cu, Cs triangle also shows a respectable response along the Fe-Cs edge of the triangle but apparently adding small amounts of Nd improves the photoresponse. Too much Nd content appears to completely kill any photoresponse as indicated by the abrupt loss of photocurrent signal as the Nd vertex is approached. The Fe, Cu, Cs triangle also shows a respectable response along the Fe-Cs edge of the triangle.

Areas of the printed patterns that show promising photocurrent can be expanded by adjusting the printed pattern such that the composition at the vertices of the newly printed triangle border the “hot spot” in the photocurrent map. Figure 3.2D shows an example of such a “zoom in” on the promising high photocurrent area of the Fe, Cs, Nd triangle from Figure 3.2C. Again an abrupt loss of photocurrent is visualized when the Nd content becomes too high. The “zoom in” technique allows for further refinement of

the composition of a promising photocatalyst. Rational methods can then be used for further compositional refinement. For example, a ternary composition that shows good light absorption, but poor current-voltage behavior for water photoelectrolysis, will be printed with a constant composition and be overprinted with gradient patterns of combinations of catalytic metals. This method provides an entry into the very large four-component phase space.

Figure 3.3 shows the “four-metals-three-at-a-time” approach for Fe, Co, Al and Cs. Figure 3.3A shows a color keyed printing pattern. We have screened this combination at both 532 nm (2.33 eV) and 632.8 nm (1.96 eV), so that an initial spectral response is obtained, and at both positive and negative biases to highlight *n*-type and *p*-type materials. It can be seen in Figure 3.3B that illuminating the  $\alpha$ -Fe<sub>2</sub>O<sub>3</sub> internal standard with 532 nm light under a positive bias produces a response as does the Fe-Cs edge of the Fe-Cs-Co triangle. The Fe-Cs-Al triangle also generates a response but with the Al suppressing the photocurrent at even small amounts. The dark regions represent areas where the photocurrent is still in the cathodic direction despite the positive applied bias and correspond to the brightest areas of the 532 nm scan done at negative bias (as shown in Figure 3.3C where the Cu internal standard “lights up”). Areas of *p*-type photoresponse that are 2 to 2.5 times higher than pure CuO are identified in Figures 3.2C and 3.2E for the Co rich regions of the Co-Al-Fe and Co-Al-Cs triangles. Scanning the sample using 632.8 nm laser light at positive bias (Figure 3.2D) produces no appreciable anodic photocurrent. Only noise and a small *p*-type response can be seen since this



**Figure 3.3 Printing and screening at two laser wavelengths and two different biases a four-metals-three-at-a-time pattern for the Fe-Cu-Co-Al system.** A. False color template showing the positions and gradients used for printing the four metal precursor solutions. B. Laser screening scan at 532 nm with a 0.5 V bias in a 0.5 M NaOH solution. C. Same film scanned at -0.5 V. D. Same film scanned at 632 nm with a 0.5 V bias. E. Same film scanned at 632 nm with a -0.5 V bias. Refer to the text for a more complete description.

wavelength is below the band gap of  $\alpha\text{-Fe}_2\text{O}_3$  and other phases that might be present. At negative bias the photocurrent image is similar to the image taken with 532 nm illumination, confirming that the new Co containing phase has a band gap of less than 1.96 eV. The photocurrent image had the same appearance as the images in Figure 3.2C and 3.2E but with a smaller maximum current value, demonstrating the strong *p*-type response of this new metal oxide composition and that it is apparently capable of a spontaneous water photoelectrolysis albeit at a very low efficiency.

Examination of the surface of the pyrolyzed samples with an optical microscope reveals that the surface can be heterogeneous and porous. Different areas of the surface appear microcrystalline, glassy or even somewhat free of any deposits. Although the heterogeneity is perhaps not aesthetically pleasing, and points out that we are not producing the true triangular ternary phase diagram of the system, it is actually a virtue of our method. Since we screen only for the desired property, photoactivity, and the phase structure and composition of our eventual target material is not known in advance, a variety of microscopic morphologies produces more diverse possibilities from which an effective photocatalyst might be discovered. SEM imaging of selected active areas of the Fe, Cs, Nd triangle revealed areas of porous microcrystalline deposits with a grain size of less than 100 nm.

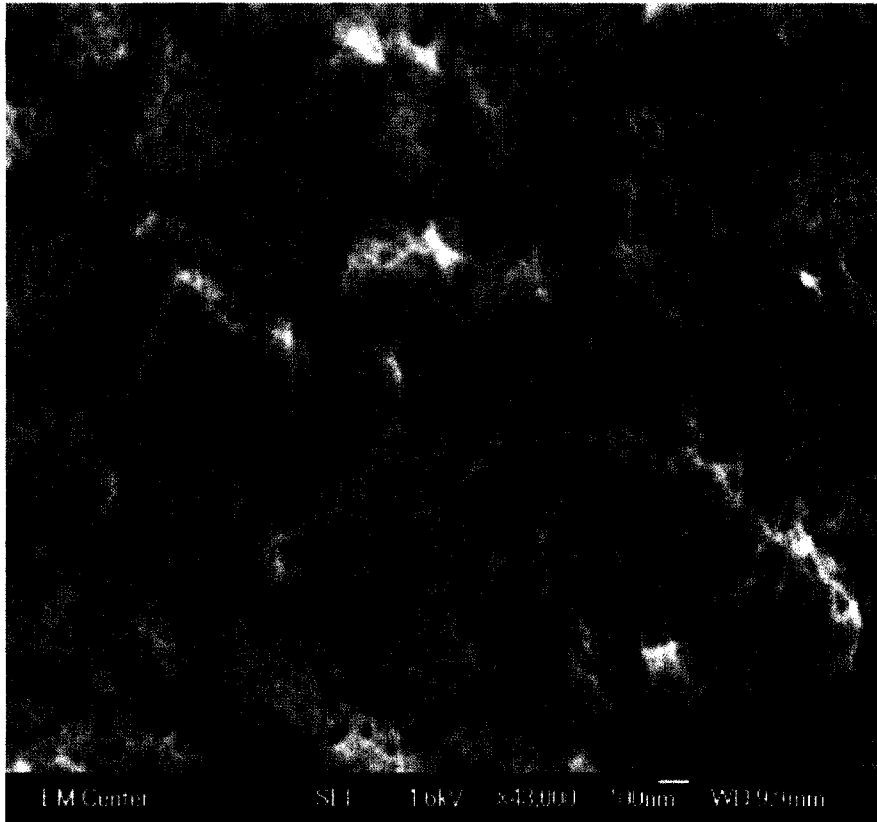


**Figure 3.4. SEM image of the bright area shown in the photocurrent scan of Figure 3.2D showing that in this area the metal oxide film is a porous film overlaying the conductive SnO<sub>2</sub>:F substrate.**

Areas of the printed patterns that show promising photocurrent response can have their composition and morphology determined. A pure crystalline compound, mixtures of crystalline compounds, solid solutions of metal oxides, and amorphous oxide materials are all possible outcomes from mixing and pyrolysis of the printed precursors. Thin film X-ray diffraction can be used to examine crystalline phases that may be present as was used to identify CuO and Fe<sub>2</sub>O<sub>3</sub> in the internal standards. Simply mixing larger amounts of the nitrate salt precursors and pyrolyzing them at the same temperature allows the preparation of larger samples for bulk analysis. Pyrolysis temperature is another important variable that will determine which phase or phases are produced; however, we are limited to a maximum temperature of 550 °C by the stability of the conducting glass substrate.

SEM coupled with EDX analysis can quantify the presence and proportion of the elements in a particular spot on the sample as was done on the area in Figure 3.3. More detailed characterization of the band gap of a promising composition can be obtained by measuring the photocurrent spectrum of that area of the triangle. Figure 3.5 shows the photocurrent spectrum of the area identified in the Co-Al-Fe triangle shown in Figure 3.3D and 3.3F (central triangle) and repeated as an inset in Figure 3.5. The photocurrent spectrum, taken in the area of the green circle in the inset of Figure 3.5, shows that this phase produces photocurrent at wavelengths out to about 785 nm or 1.58 eV. A band gap lower than ~1.8 eV makes this material a candidate p-type material for a p-n photoelectrolysis system. Further and more detailed examination of the behavior and phase composition of this new material is currently underway and will be presented elsewhere<sup>22</sup>.

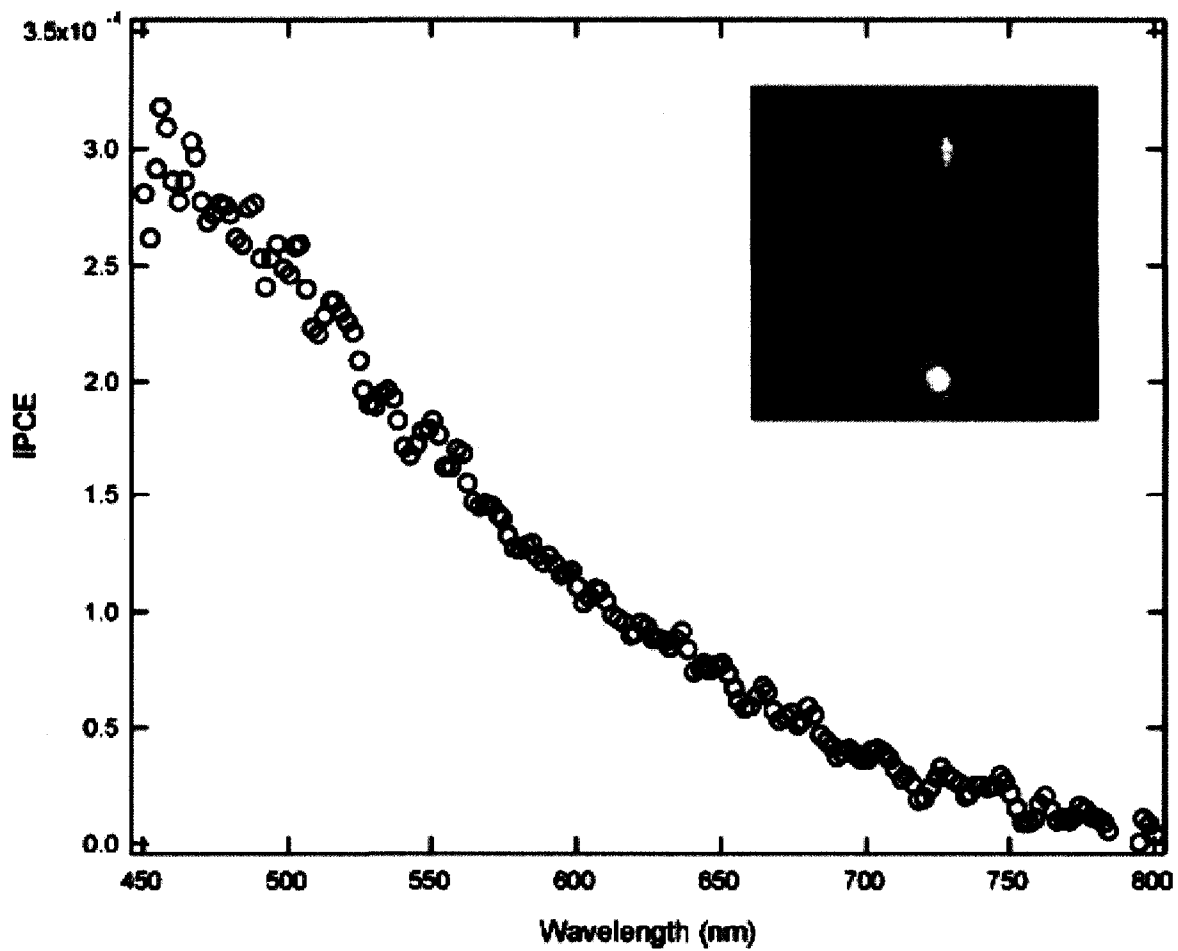


Figure 3.5. Photocurrent action spectrum measured in the area of the bright spot seen in Figure 3.3C and 3.3E and outlined with a green circle in the inset. The spectrum was measured in a 0.5M NaOH solution at a bias of -0.5 V.

Any discovered materials must be configured to achieve useful energy conversion efficiencies. The low IPCE values ( $10^{-4}$  to  $10^{-5}$ ) measured for the phases in Figures 3.1 and 3.2 are a result of the thin film of material allowing most of the light to pass through without being absorbed. This is because transitions involving d and f levels on the metal atoms, that impart color to the oxides, generally are forbidden transitions and do not have high absorption coefficients. The low absorption coefficients result in the incident light penetrating deep into the material and, since the carrier mobilities in oxides are generally much lower than in conventional solar cell materials, recombination of photogenerated carriers occurs before they can reach the semiconductor/electrolyte interface. Even good single crystals of transition metal oxides have energy conversion efficiencies that are not useful due to their inherently short diffusion lengths<sup>23</sup>.

Problems of low light absorption and small carrier mobilities were overcome by the dye-sensitized nanocrystalline TiO<sub>2</sub> photovoltaic cell, also known as the Grätzel solar cell<sup>24</sup>. The light absorption was improved by creating a high surface area porous TiO<sub>2</sub> electrode so that the incident light traverses many dye/oxide interfaces. When light absorption does occur, the carriers are always created at the interface so that carrier diffusion lengths do not limit performance. The electron lifetime in the porous TiO<sub>2</sub> network was long enough that they could diffuse to the back contact and be collected as photocurrent. The Grätzel cell contains relatively cheap materials and has reached solar to electric conversion efficiencies of up to 11%<sup>25</sup> with a demonstrated stability over many

thousands of hours<sup>26</sup>. We anticipate increasing the photoelectrolysis efficiency of any discovered materials either by combining them with a nanocrystalline TiO<sub>2</sub> or deploying them as nanocrystalline thin films. The coating on titanium dioxide will be only several nanometers thick or be made up of nanometer-sized particles so that photogenerated carriers will reach the electrolyte interface despite their low mobilities. Low absorption coefficients will not limit device efficiencies since the total path length of light through the absorbing oxide can be large enough to absorb virtually all of the incident solar light.

The “Grätzel configuration” also provides additional device efficiency advantages for a photoelectrolysis system. The high surface area results in lower microscopic current densities thereby reducing overpotential losses for hydrogen and oxygen generation. Low current densities will also contribute to electrode stability since corrosion reactions are often multielectron. Backside illumination, rather than through the electrolyte, will reduce any scattering of incident solar radiation from evolving gas bubbles, a problem that plagues the most efficient front-side illumination photoelectrolysis devices<sup>3</sup>.

## **3.6 Conclusions**

We have demonstrated a new high throughput combinatorial method to search for materials capable of the photoelectrolysis of water. Ink jet printing was shown to be an inexpensive, rapid and versatile method of patterning metal oxide precursors onto a conductive glass substrate. Subsequent pyrolysis yielded electrodes with patterns of metal oxide compositions that, when immersed in an electrolyte, could be easily screened for photoelectrolysis activity using a simple scanning laser system. We have shown that promising compositions can be identified using our approach. The throughput of a combinatorial search is limited by the slowest step in the process. In our case we have determined that the screening step is rate limiting. Higher laser power and/or building additional scanning systems can dramatically increase throughput for this step and both are currently being implemented in our lab. The knowledge base derived from the increasing number of printed and screened compositions should also begin to suggest new combinations and further refine the compositions and properties needed to solve this important problem.

## **Acknowledgements**

We appreciate useful discussions with Dave Schut. Michael Woodhouse acknowledges financial assistance from the Maciel Fellowship and assistance with LabView<sup>®</sup> programming from Dr. Michael Kramer. Partial support from the DOE under contract #DE-F603-96ER14625 is also acknowledged.

## References

- (1) Fujishima, A.; Honda, K. *Bull. Chem. Soc. Japan* **1971**, *44*, 1148-1150.
- (2) Fujishima, A.; Honda, K. *Nature* **1972**, *238*, 37-38.
- (3) Khaselev, O.; Turner, J. A. *Science* **1998**, *280*, 425-427.
- (4) Nozik, A. J. *Appl. Phys. Lett.* **1977**, *30*, 567-569.
- (5) Reddington, E.; Sapienza, A.; Gurau, B.; Viswanathan, R.; Sarangapeni, S.; Smotkin, E. S.; Mallouk, T. E. *Science* **1998**, *280*, 1735.
- (6) Wang, J.; Yoo, Y.; Gao, C.; Takeuchi, I.; Sun, X.; Chang, H.; Xiang, X.-D.; Schultz, P. G. *Science* **1998**, *279*, 1712-1714.
- (7) Sun, X.-D.; Gao, C.; Wang, J.; Xiang, X.-D. *Appl. Phys. Lett.* **1997**, *70*, 3353-3355.
- (8) Danielson, E.; Devenney, M.; Giaquinta, D. M.; Golden, J. H.; Haushalter, R. C.; McFarland, E. W.; Poojary, D. M.; Reaves, C. M.; Weinberg, W. H.; Wu, X. D. *Science* **1998**, *279*, 837-839.
- (9) Danielson, E.; Golden, J. H.; McFarland, E. W.; Reaves, C. M.; Weinberg, W. H.; Wu, X. D. *Nature* **1997**, *389*, 944-948.
- (10) Dover, R. B. v.; Schneemeyer, L. F.; Fleming, R. M. *Nature* **1998**, *392*, 162-164.
- (11) Jaramillo, T. J.; Ivanovskaya, A.; McFarland, E. W. *J. Comb. Chem.* **2002**, *4*, 17-22.
- (12) Cong, P.; Doolen, R. D.; Fan, Q.; Giaquinta, D. M.; Guan, S.; McFarland, E. W.; Poojary, D.; Self, K.; Turner, H. W.; Weinberg, W. H. *Angew. Chem. Int. Ed.* **1999**, *38*, 484-488.

- (13) Baeck, S. H.; Jaramillo, T. F.; Brandli, C.; McFarland, E. W. *J. Comb. Chem.* **2002**, *4*, 563-568.
- (14) Sirringhaus, H.; Kawase, T.; Friend, R. H.; Shimoda, T.; Inbasekaran, M.; Wu, W.; Woo, E. P. *Science* **2000**, *290*, 2123-2126.
- (15) MacBeath, G.; Schreiber, S. L. *Science* **2000**, *289*, 1760-1763.
- (16) Takeda, N.; Parkinson, B. A. *J. Am. Chem. Soc.* **2003**, *125*, 5559-5571.
- (17) Iwanski, P.; Curran, J. S.; Gissler, W.; Memming, R. *J. Electrochem. Soc.* **1981**, *128*, 2128.
- (18) Leygraf, C.; Henderwerk, M.; Somorjai, G. A. *J. Phys. Chem.* **1982**, *86*, 4484-4485.
- (19) Kennedy, J. H.; Anderman, M.; Shinar, R. *J. Electrochem. Soc.* **1981**, *128*, 2371-2373.
- (20) Houlihan, J. F.; Armitage, D. B.; Hoovler, T.; Bonaquist, D.; Madacsi, D. P.; Mulay, L. N. *Mat. Res. Bull.* **1978**, *13*, 1205-1212.
- (21) Hardee, K. L.; Bard, A. J. *J. Electrochem. Soc.* **1977**, *124*, 215-224.
- (22) Woodhouse, M.; Parkinson, B. A. *In Preparation* **2007**.
- (23) Jarrett, H. S.; Sleight, A. W.; Kung, H. H.; Gilson, J. L. *J. Appl. Phys* **1980**, *51*, 3916-3925.
- (24) Regan, B. O.; Gratzel, M. *Nature* **1991**, *353*, 737.
- (25) Nazeeruddin, M. K.; Kay, A.; Rodicio, I.; Humphry-Baker, R.; Muller, E.; Liska, P.; Vlachopoulos, N.; Gratzel, M. *J. Am. Chem. Soc.* **1993**, *115*, 6382-6390.
- (26) Kohle, O.; Meyer, A.; Meyer, T.; Gratzel, M. *Adv. Mater.* **1997**, *9*, 904-906.

# Chapter 4: Challenges in the Development of the Method for the Optimization of Newly Discovered Photoelectrolysis Materials

## 4.1 Preface and Abstract

In this chapter I will discuss several supplementary details related to the results in Chapter 5 that have been submitted for publication in *Chemistry of Materials*. The first section of this chapter is meant to give a more thorough account of the history, procedures, equipment, and development of appropriate precursor materials formulations and substrate pretreatment for effectively printing materials with the piezoelectric-based Dimatix printer.

I will also discuss some of the surprisingly difficult obstacles that were encountered to find an appropriate substrate and electrolyte for the deployment of the optimized catalyst as a large-area thin film photoelectrode. The problems that were encountered in this development will probably be typical to anyone attempting to extend the search protocol to other, perhaps more promising, *p*-type materials and it is for this reason that this discussion is in order. The results highlight the need for finding an appropriate substrate for any newly discovered material and that this potentially challenging step should not be taken for granted.

## 4.2 The Development of an Appropriate Precursor Formulation for Printing and Substrate Pretreatment

After the publication that comprises Chapter 3<sup>1</sup>, one question became immediately evident: how can one precisely determine the composition of the best performing compounds? Although the Hewlett-Packard Deskjet printer proved to work very well at rapidly producing large numbers of materials to screen, it is difficult to know the exact stoichiometry of a promising area. Initially it was hoped that the triangular patterns used to deposit the precursors had a linear relationship between the drop density and the grayscale values selected within the drawing program, leading to a reasonable estimate of the composition in a region within the quasi-ternary phase diagrams. However, it was not clear how one could explicitly know the density of drops within a printed region since one needs to know the number of nozzles actually printing for each material cartridge, whether the drop volumes are consistent from one cartridge to the next, and how the problems of pooling and melting affect the distribution of the materials.

Fortuitously, it was at about this same time in the fall of 2005 that the research-grade Dimatix Materials Deposition printer was released at the Digital Fabrication Conference in Baltimore, Maryland. While systems with the same capabilities to determine the number of nozzles jetting and the drop volumes had existed before, the cost (typically in the hundreds of thousands of dollars) would have made it difficult to obtain this more flexible hardware.

Ink formulations were initially prepared for this printer using the same additives as for the Hewlett-Packard printer (ammonium nitrate and nitric acid). Almost all attempts at printing with these additives proved unsuccessful, leading to the realization that different fluid characteristics were needed due to the different ink jetting mechanisms. Piezoelectric printers, such as the one manufactured by Dimatix, differ from the HP thermal inkjet printers produced in that the primary problem is not the clogging of nozzles due to hydroxide formation as a result of the rapid heating at the nozzles, but instead the requirements that the “ink” have a specific viscosity and surface tension to properly facilitate proper droplet formation as the nozzle opens in response to the applied voltage. Surfactants have to be added in order to properly regulate the surface tension. If the surface tension is too high, as in the pure aqueous based solutions used for thermal inkjet printing, firing is impeded because the drops do not easily break free from the bulk solution, whereas a surface tension that is too low leads to ink leaking out of the nozzles. Several different surfactants are used by the ink jetting industry including sodium sulfonate, alkyl sulfonates, and diethylene glycol monobutyl ether<sup>2</sup>. Likewise, agents to increase the viscosity, including 2-pyrillodone and several different polyalcohols, are also and the need for these additional additives presented even more variables. Unfortunately, the only details that were given with the printer was that the viscosity and surface tension values for printable fluids needed to be close to 11-cP and 33-dyn/cm, respectively, but very few details or suggestions as to how to obtain these values were provided as working formulations are considered to be proprietary.

A large number of solutions were prepared containing variable concentrations of metal nitrates, viscosity agents, and surfactants to test for printing performance. The viscosity of each was determined with a glass viscometer immersed in a temperature controlled water bath using 2-pyrillidone as the reference fluid. No clear pattern emerged from the observed printing performance, except for the lack of consistent printing. Therefore, the Material Data Safety Sheet (MSDS) for the model fluid solution provided by the equipment manufacturer was requested. It was from this sheet that diethylene glycol and diethylene glycol monobutyl ether were revealed to be the most appropriate viscosity agent and surfactant, respectively, and this led to several serial trials to determine the optimal amount of each that needs to be added to the printer cartridges.

The new inks also presented some new problems, such as substrate adhesion and feature resolution, because they wet the FTO substrate differently than the earlier solutions with viscosity and surface tension values closer to that of water. The typical problem, presumably due to the lower surface tension relative to pure aqueous solutions, was that the printed patterns would spread out over the substrate resulting in very poor resolution. As partial evaporation of the solvent by heating the substrate during printing (another advantageous feature of the Dimatix printer) did not alleviate this problem, the only remaining option was to perform a surface pretreatment on the substrate in order to maintain printing resolution. Several treatments were tried including soaking in a saturated KOH in isopropanol solution (the so-called "base bath"), applying dilute sulfuric and nitric acid solutions with a Kimwipe, immersing the substrates in a 3:1

mixture of concentrated sulfuric acid and 30% hydrogen peroxide (the so-called “Piranha” treatment), simply rinsing with water and then ethanol, and rendering the surface highly hydrophobic by applying the Siliconizing Fluid<sup>®</sup> manufactured by Pierce Chemical with a Kimwipe. The siliconizing fluid made the most hydrophobic surface that allowed the small feature sizes necessary for printing the template shown in Figures 5.2 and 5.3. It was judged that the successful completion of both inkjet formulation and surface treatment was achieved when the test pattern shown in Figure 4.1 became possible. The pattern was created by Dimatix engineers to establish a benchmark for the printing resolution of their product.

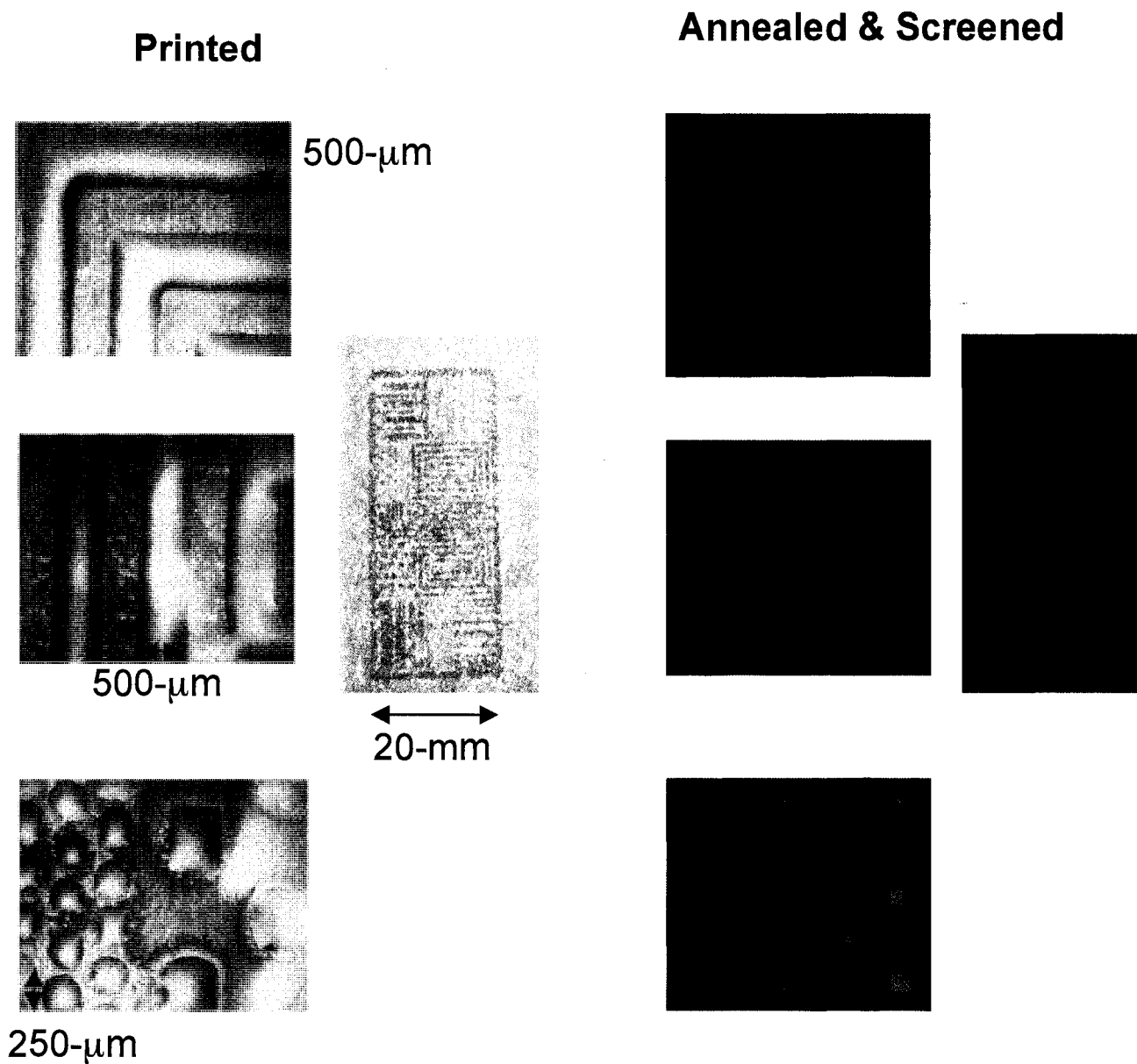


**Figure 4.1: Hypothetical circuit patterns created by printing and screening  $\alpha\text{-Fe}_2\text{O}_3$  precursors.** These patterns represent the achievement of printing industry standard line widths and small feature sizes. It also shows how the resolution of the scanning can be fine-tuned down to the diameter of the laser beam (notice how the smallest squares in the bottom picture cannot be resolved by the approximately 1-mm diameter laser beam). As described in the text, both the printable solution formulation and the substrate had to be optimized to achieve this result. The screening was performed in 0.1-M NaOH solution with a 532-nm laser in a short-circuit two-electrode configuration.

### 4.3 Substrate and Electrolyte Optimization for the Fe-Co-Al Oxide

One thing that would seem obvious is that, since the Fe-Co-Al Oxide functioned as a *p*-type photoelectrode (performing the proton reduction half-reaction), higher current densities should be expected by using an electrolyte with a higher concentration of protons compared to that obtained in basic electrolyte. 50 mM HClO<sub>4</sub> was chosen as a logical entry as the anion is expected to be electrochemically inert. 2 cm x 2 cm “large-area” photoelectrodes were prepared with the optimized stoichiometry on FTO with a precursor printing density of approximately 906 drops/ mm<sup>2</sup>, based upon the results shown in Figure 5.6 where the near-optimal thickness was determined, and calcined as usual for 2 hours in air at 500 °C. The HClO<sub>4</sub> solution was degassed for at least ten minutes by bubbling with nitrogen gas, the sample was immersed into the electrolyte, and a steady flow of nitrogen was maintained by placing the nitrogen gas flow just above the solution. The cyclic voltammetry curves shown in Figure 4.2 (and subsequent figures) were obtained with a computer-controlled CompactStat potentiostat manufactured by Ivium Technologies with a Pt basket counter electrode and either a saturated calomel (SCE) or saturated sodium calomel (SSCE) reference electrode, as indicated in the respective figures. The first scan (the blue dotted curve) was obtained without any external illumination except that provided by the lights in the laboratory, which should be negligible relative to the 150-W

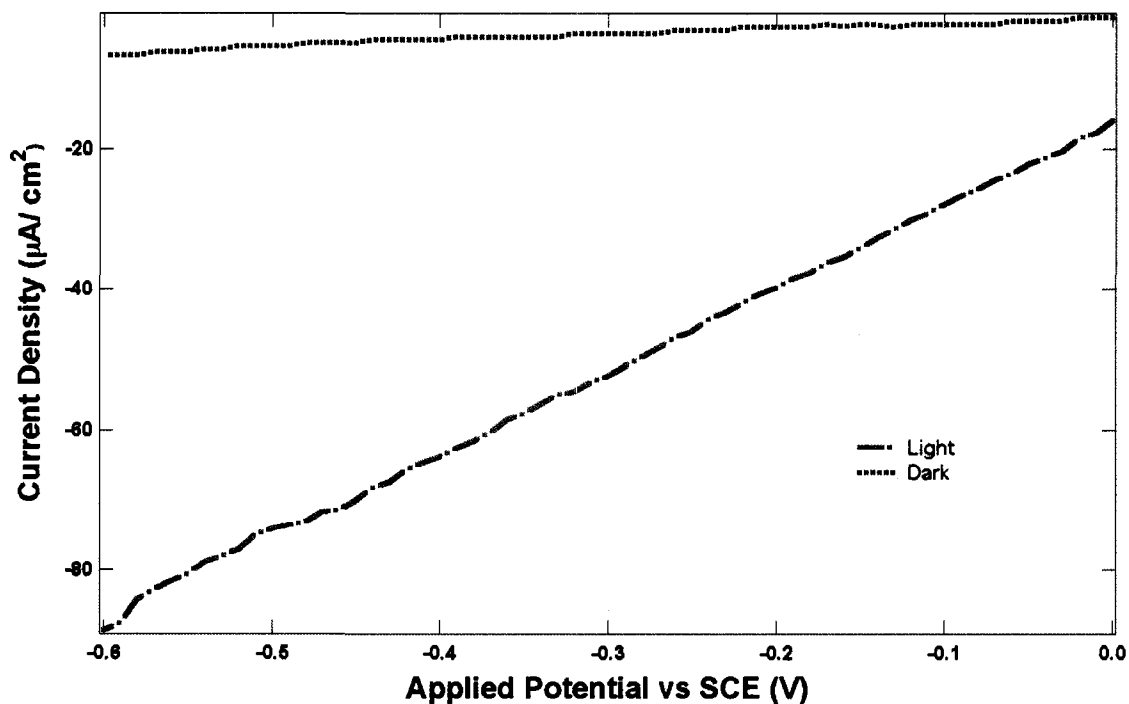


**Figure 4.2:** The *first* (and unstable) dark and photocurrent-voltage curves obtained for a 2 cm x 2 cm film printed onto an FTO substrate immersed in deoxygenated 50-mM HClO<sub>4</sub>. The sweep rate was 0.5 mV/s. Illumination is provided by a 150-W Xe lamp.

Xe lamp that was focused onto the printed sample to obtain the illuminated curve. The reverse scans are not shown as no hysteresis was evident.

As shown, the initial results of Figure 4.2 certainly appeared promising and so it was decided to further improve the system by depositing catalytic platinum nanoparticles onto the surface with the hope that, by lowering the activation barrier needed for proton reduction, more current could be produced over the range of potentials investigated. The method of photoelectrodeposition of catalytic nanoparticles must be

optimized with respect to the size and areal surface coverage<sup>3,4</sup>. In particular, the photoconversion of sunlight to hydrogen from aqueous solutions can be made more efficient only when the diameters of electrodeposited catalyst islands on the surface are small relative to the wavelength of light illuminating the sample. Also, the surface coverage of the semiconductor by the metal must be tailored such that the growth of the Pt islands proceeds until the compromise is reached between the light absorption loss caused by a high density and size of catalyst islands and a spacing that is still smaller than the minority carrier surface diffusion length in order for an improved electron-hole pair separation efficiency to occur.

While all of the requirements mentioned would make it seem that *multiple* iterations of deposition and SEM would be necessary, the optimal catalyst size and density is best obtained empirically<sup>4</sup>. Quite simply, one immerses the semiconductor photoelectrode into a solution containing a Pt-group metal salt in the working electrolyte of interest and performs multiple cyclic voltammetry cycles under illumination until the maximum photocurrent and/ or fill factor is achieved. One should expect an increase in the photocurrent as the catalyst nanoparticles are deposited until the size (and/ or density of surface coverage) becomes too large. This concept is roughly demonstrated in Figure 4.3 in which a total of 12 cyclic voltammetry curves obtained in deoxygenated 50-mM HClO<sub>4</sub> containing 100- $\mu$ M H<sub>2</sub>PtCl<sub>6</sub> are shown. The current at each potential within the range studied was observed to continually increase from the first scan (the solid red line) to the seventh scan (the dot-dashed green line showing the maximum current achieved)

and then began to decrease until the current was actually smaller than it was before immersion into the platinization solution (scan 11, the purple dashed-triple dotted line).

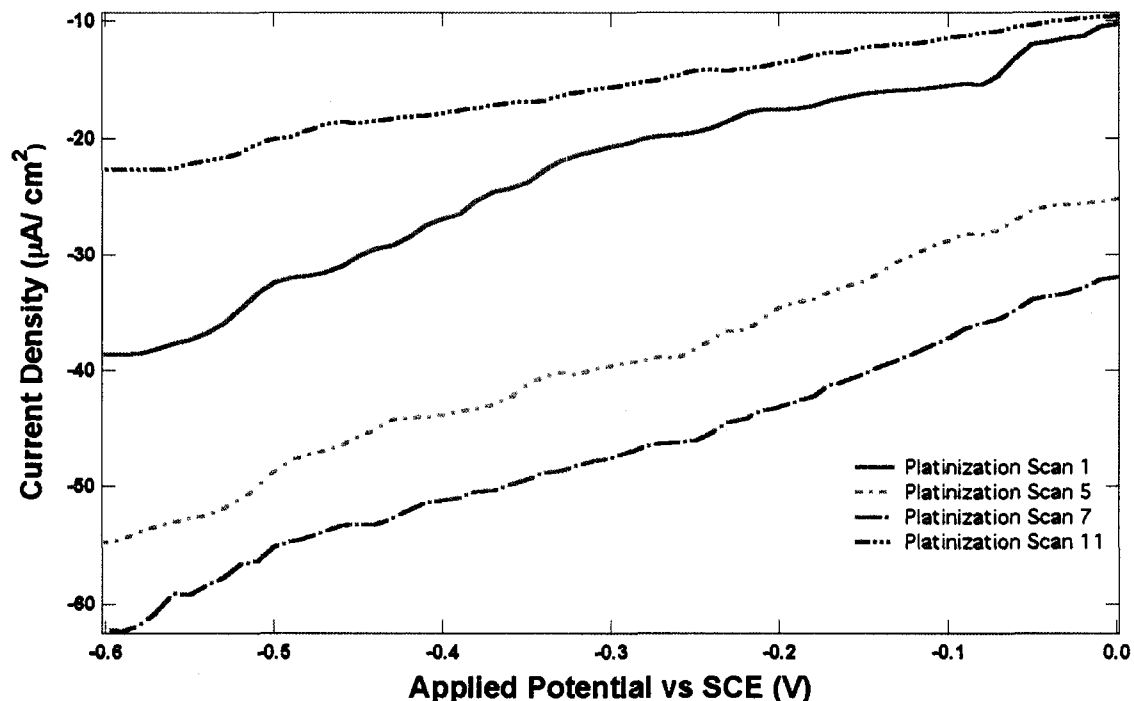


**Figure 4.3:** Selected cyclic voltammetry curves for the photoelectrodeposition of platinum metal onto for a 2 cm x 2 cm film printed onto an FTO substrate. The sample was immersed in deoxygenated 50-mM HClO<sub>4</sub> containing 100-mM H<sub>2</sub>PtCl<sub>6</sub> and the sweep rate was 0.5 mV/s. Illumination is provided by a 150-W Xe lamp. The reverse scans are not shown for the sake of clarity in the figure and because no hysteresis was evident.

For the sample immersed into the HClO<sub>4</sub> and H<sub>2</sub>PtCl<sub>6</sub> solution, an SEM study was done to investigate the size and distribution of the Pt islands after the 11-cycle deposition shown in Figure 4.3. The top image in the figure is a piece of Al-Co-Fe oxide on FTO before immersion into any solution. The middle and bottom images show the areal density and size of the islands, respectively after too much Pt had been deposited. As

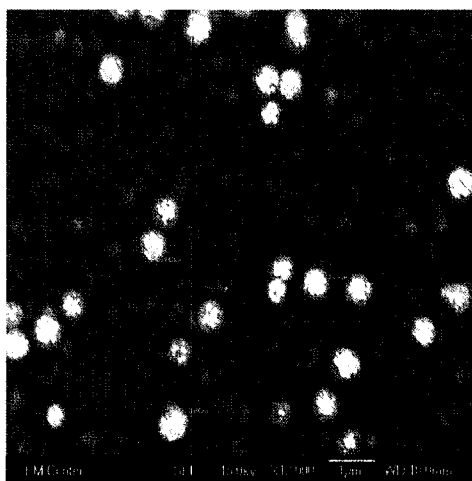
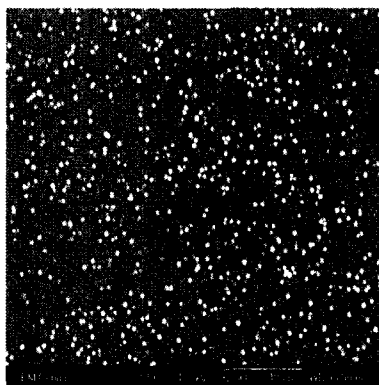


**Figure 4.4:** Selected scanning electron microscope (SEM) images of a freshly prepared Al-Co-Fe oxide sample on FTO (top image) and after all 11 of the Pt deposition cyclic voltammetry cycles shown in Figure 4.3. The middle image gives an overview of large-scale ordering and spacing of the islands on the semiconductor surface and the bottom image can be used to estimate the particle size. Notice that the size of the particles is approximately that of light within the visible spectrum.

shown, the diameters of the Pt islands have grown to be within the visible wavelength range, a physical property that interferes with the passage of light to create photoexcited electron-hole pairs. The optimal surface coverage is also unknown, however, as are the carrier diffusion lengths in this particular material (although they are probably less than 100-nm) so there may be additional factors to explain the effects of depositing too much platinum.

Conceptually, one could use the information obtained in this particular example to prepare optimized samples by stopping after seven cycles. Such a procedure was used in deciding how best to deposit platinum for the successful sample shown in the published figure 5.9. Unfortunately, further work carried out on other Fe-Co-Al oxide samples on FTO in  $\text{HClO}_4$  presented several issues that superceded the optimization of catalyst islands. The next three identically prepared samples were immersed into the same 50-mM  $\text{HClO}_4$  solution but, unlike the initial results shown above in Figure 4.2, six voltammetry cycles (alternating between dark and illuminated) were carried out instead of just two. In all cases, both the illuminated and dark currents decreased from the first cycle to the last and the material delaminated from the FTO substrate. It appeared that photoelectrodeposition of Pt could help to improve the efficiency of hydrogen generation, when the material adhered to the substrate, but delamination was also occurring to negate those gains.

It was postulated that film delamination was due to corrosion from the overly acidic electrolyte, as using 50 mM  $\text{H}_2\text{SO}_4$  also gave similar problems, so several buffers

of higher pH were studied. Diluted pH 4 buffers were prepared from glacial acetic acid and sodium hydroxide and diluted pH 7 and 12 buffers were prepared from phosphoric acid and the appropriate amounts of sodium hydroxide. Pure NaOH solutions were also attempted again. Months of disappointing experiments were carried out, with only a couple of patterns emerging.

If stability was not an issue, and assuming that the working solution was thoroughly degassed to prevent photocurrent from electrochemical reduction of oxygen, then multiple cyclic voltammetry cycles should have produced curves with no hysteresis. This was not the case for the pH 4 buffer, as shown in Figure 4.5, with similar patterns seen in multiple experiments for all electrolytes studied. In this experimental design, the first curve was obtained while the sample was illuminated. The second, without illumination, was obtained immediately after. The subsequent scans were also alternated between light and dark. As can be seen in the figure, there is a gradual reduction in current after *each* cycle and, at times, the dark current appears to be as large as the photocurrent (as a side note, manually blocking the light during an illuminated scan and then illuminating again did produce significant spikes in current so we can say that the material was photoactive under these conditions).

The sequential decay of the photocurrent in the buffered solutions indicates that a deleterious irreversible process occurred during the course of the potential cycling.

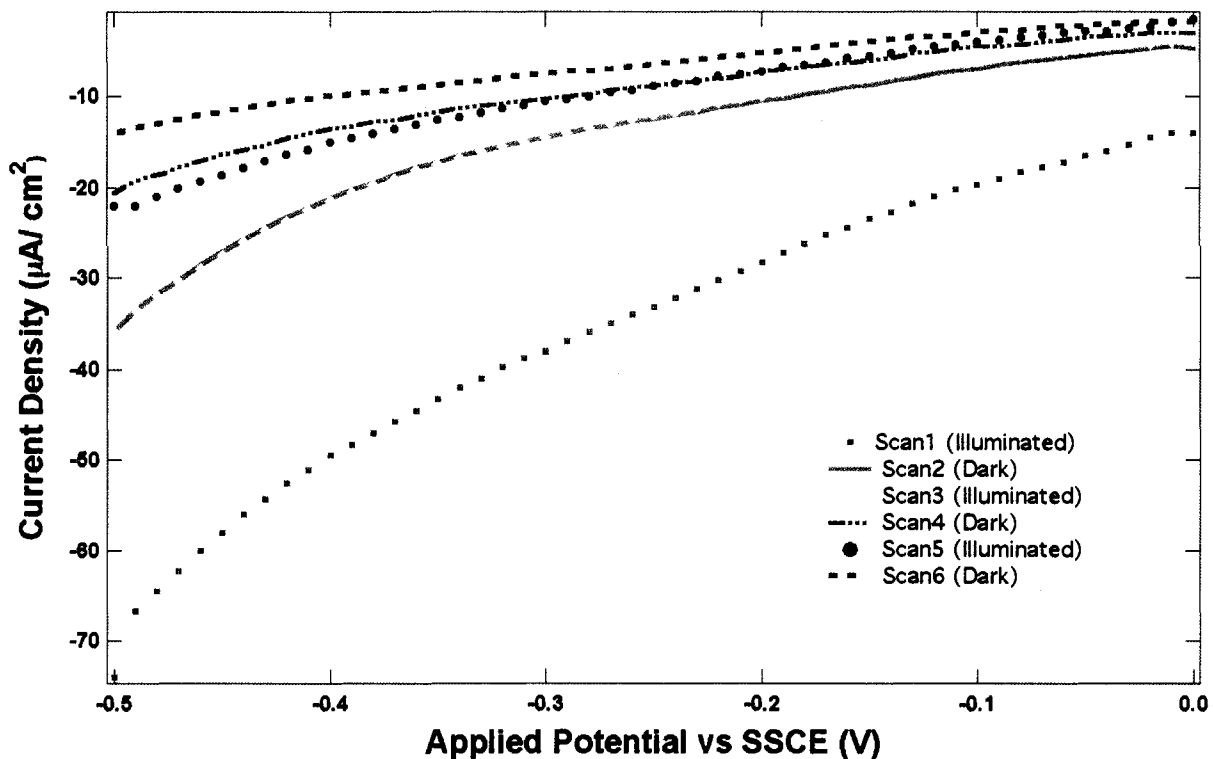


**Figure 4.5:** Current-Voltage curves for a 2 cm x 2 cm photocatalyst film printed on an FTO substrate. The sample was immersed in a deoxygenated  $\text{HC}_2\text{H}_3\text{O}_2/\text{NaC}_2\text{H}_3\text{O}_2$  pH 4 buffer and the sweep rate was 5 mV/s. Illumination is provided by a 150-W Xe lamp. The reverse scans are not shown for the sake of clarity in the figure and because no hysteresis was evident. See text for a discussion of the degradation of current pattern with potential cycling, a trend also seen in  $\text{HClO}_4$ ,  $\text{H}_2\text{SO}_4$ , pH 4, pH7, and pH 12 solutions.

The delamination of the film was obviously a significant factor, but the film usually adhered to the substrate in NaOH solutions. A representative set of data obtained in this electrolyte is shown in Figure 4.6.

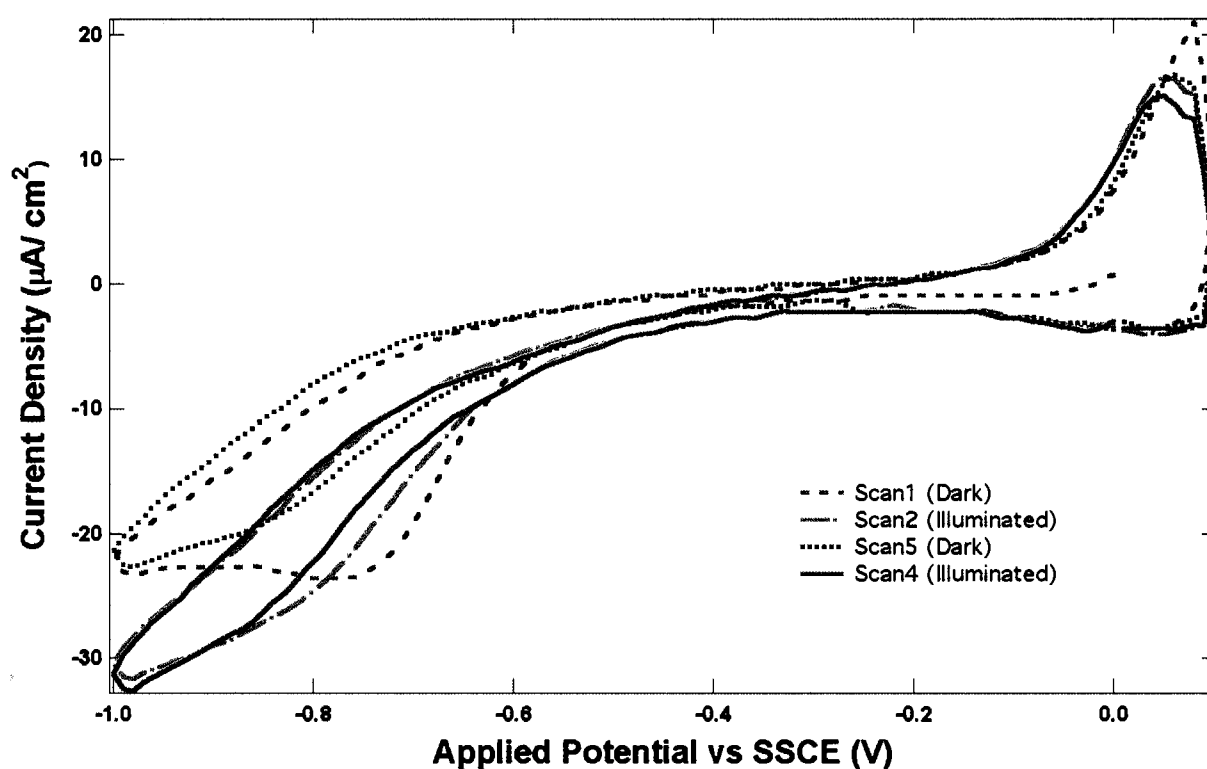


**Figure 4.6:** Current-Voltage curves for a 2 cm x 2 cm photocatalyst film printed on an FTO substrate immersed in a deoxygenated 0.1 M NaOH solution. The sweep rate was 5 mV/s. Illumination is provided by a 150 W Xe lamp. See text for a discussion of the degradation of current with potential cycling.

In this experiment, six cycles were performed, alternating between illuminated and dark, as above. The most noteworthy observation in figure 4.6 is that of the reduction process occurring at approximately  $-0.8$  V vs SSCE (thermodynamically about  $0.2$ -V positive of dark hydrogen production) that is present in both the illuminated and dark curves. The oxidation peaks positive of  $0.0$  V vs SCE could be due to the partial reoxidation of the species or the onset of dark oxygen production that could occur at  $+0.22$  V vs. SSCE in this electrolyte. The dark reduction peak current is highest for the first dark scan and diminishes over subsequent cycles. The photocurrent curves also seem to be affected by the dark reduction process as the most significant difference between the first and later scans (numbers two and four) occurs near  $-0.8$  V vs SSCE. As can be seen from the figure, the semiconductor was typically stable in this electrolyte (other experiments did, however, often show a slight decline in the maximum current near  $-1.0$  V vs SSCE although not nearly as significant as in the acid and buffer solutions), but the large amount of dark current that was present is not desirable for a demonstration of the effectiveness of the newly discovered material.

To elucidate the role of the substrate in the overall electrochemical process, a series of blank experiments were carried out where only the FTO (no printed semiconductor) was immersed in the electrolytes that had been used previously. The results shown in Figure 4.7 unequivocally demonstrate that the substrate contributes a significant amount of current to the overall redox process. Moreover, because the scans

were alternated between light and dark, and because no effect from illumination was observed on the curves, we can also say that the photocatalyst was responsible for the photoactivity that was seen.

The position of the peak in the reduction curves has a clear pH dependence with a shift to more negative potentials with increasing pH. In all cases, the peak does occur before the thermodynamic onset of dark hydrogen production (-0.47 for pH 4, -0.65 for pH7 and -1.0 V for 0.1 M NaOH) and so the peaks correspond to some redox process within the substrate. The most likely explanation of the peak is the reduction of the tin oxide layer and the shift in peak positions is very close to the theoretical value of 0.059 V per pH unit<sup>5</sup>.

Due to the reduction of the SnO<sub>2</sub> and subsequent delamination of the Fe-Co-Al oxide film, it was decided that FTO was not an appropriate substrate when negative potential scans are needed, as is the case for *p*-type semiconductors. Therefore, several other substrates were tried including printing thin films onto glassy and reticule carbon electrodes or titanium foil, and pressing a powder into Indium foil. No photocurrent was detectable on any of these substrates. In the hopes that different doping characteristics might mitigate the problem, printing onto Indium-doped tin oxide (another very common transparent conducting oxide) was also attempted and current-voltage analysis was performed in both neutral (pH 7) buffer and NaOH. Trends very similar to FTO were present for this substrate as well.

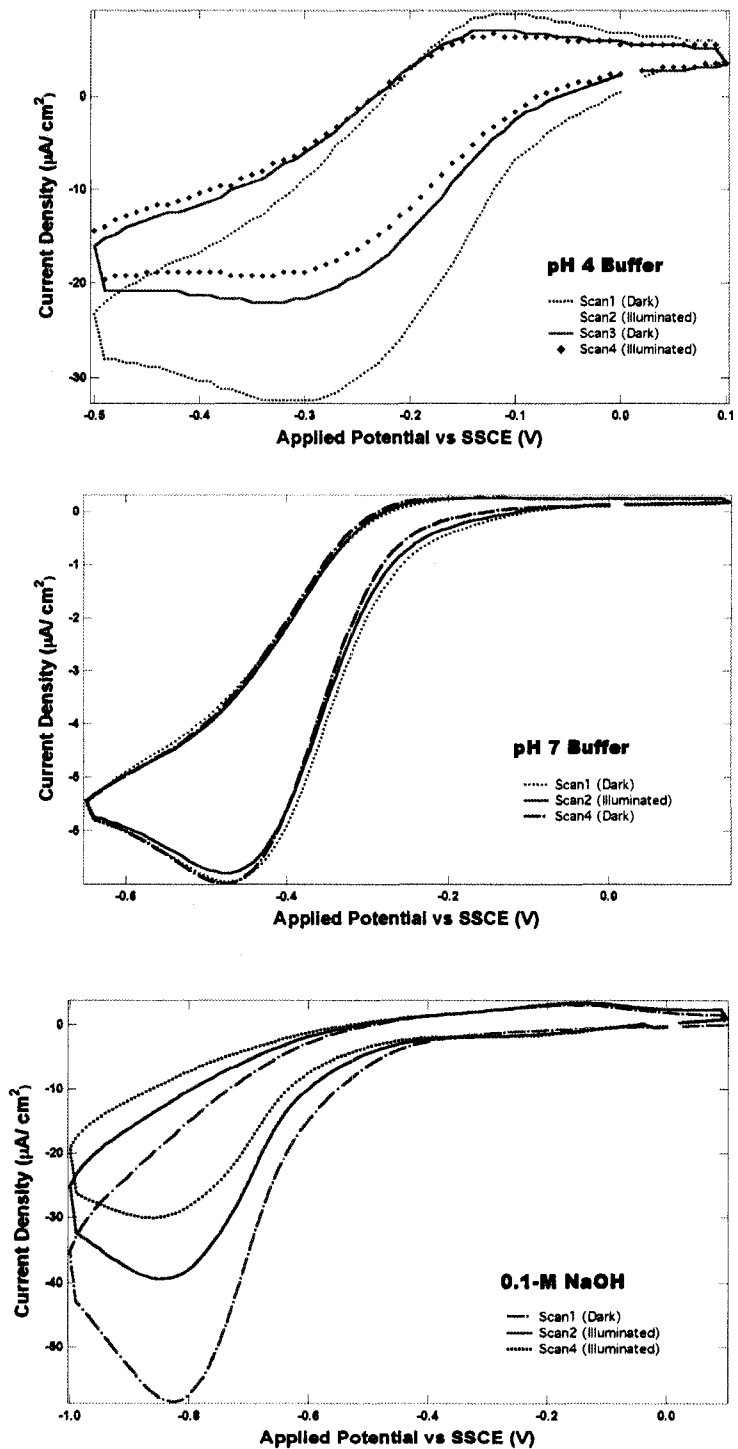


**Figure 4.7:** A sampling of cyclic voltammetry curves for pure FTO immersed in several of the electrolytes studied. The sweep rate was 5 mV/s for all experiments. Illumination was provided by a 150 W Xe lamp. See text for a possible explanation of the cause of the cathodic peak and the degradation of current with potential cycling.

An inert, flat, and large area substrate that has a large hydrogen overpotential was needed. Gold-on-mica was ultimately found to meet these criteria and can be readily made in a metal evaporator. To contrast the performance of the catalyst on this substrate relative to the others discussed in this chapter, it is useful to examine Figure 4.8. One can see that no obvious dark reduction peaks exist and that the curves essentially retrace themselves. These curves were obtained *before* those in the published figure 5.9 and on a different day. In addition, the sample was also placed into the solution described for the electrodeposition of Pt and then the last curves of Figure 5.9 (showing the *greatest* amount of current) were obtained. Finally, the catalyst was also subjected to more than 30 minutes of -1.0 V applied bias to test the longevity of the photocurrent, which varied less than  $\pm 0.5\%$  during the entire illumination time. Calculation of the total amount of charge collected due to current after all of the cyclic voltammetry and steady-state measurements is much more than an order of magnitude greater than that corresponding to the complete reduction of the metal oxide film. This calculation demonstrates that the material was catalytic- something that was impossible to tell on FTO because of the large amount of dark current.

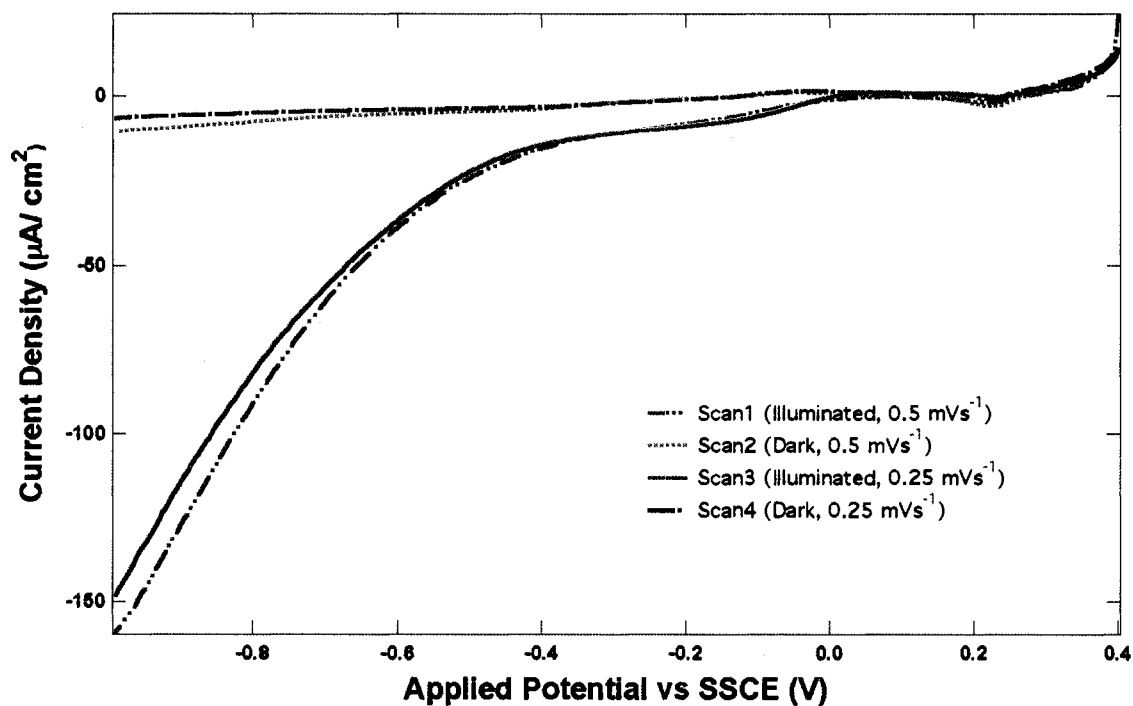


**Figure 4.8:** Dark and photocurrent-voltage curves for a 2 cm x 2 cm film printed onto a gold-on-chromium-on-mica substrate immersed in deoxygenated 0.1 M NaOH. The sweep rate for the different scans is indicated in the legend. Illumination is from a 150W Xe lamp. This shows the stability of the catalyst for this substrate- especially in light of the fact that these curves were obtained *in addition* to those of figure 5.9.

In conclusion, the second section of this chapter really highlights how significant of a problem the substrate might be in the design of an effective photoelectrolysis system. In particular, fluorine-doped tin oxide is the substrate of choice for virtually every recent paper related to the deposition and characterization of photoelectrolysis materials in thin-film form. To my knowledge, the materials that have been characterized on this substrate have been *n*-type for which current-voltage curves are obtained by scanning under potentials that are positive of the SnO<sub>2</sub> reduction. The work outlined here illustrates why any literature reports of current-voltage curves obtained under negative potentials on FTO in aqueous solutions (probably for the rarely characterized *p*-type materials) should be carefully reviewed.

## References

- (1) Woodhouse, M.; Herman, G.; Parkinson, B. A. *Chem. Mater.* **2005**, *17*, 4318.
- (2) Calvert, P. *Chem. Mater.* **2001**, *13*, 3299-3305.
- (3) Heller, A. *Science* **1984**, *223*, 1141-1148.
- (4) Heller, A.; Aharon-Shalom, E.; Bonner, W. A.; Miller, B. *J. Am. Chem. Soc.* **1982**, *104*, 6942.
- (5) Tan, M. X.; Laibinis, P. E.; Nguyen, S. T.; Kesselman, J. M.; Stanton, C. E.; Lewis, N. S. *Prog. Inorg. Chem.* **1994**, *41*, 21-145.
- (6) Bard, A. J.; Faulkner, L. R. *Electrochemical Methods*; 2 ed.; John Wiley & Sons, Inc.: New York, 2001.

## **Chapter 5: Combinatorial Discovery and Optimization of a Complex Oxide with Water Photoelectrolysis Activity**

### **5.1 Preface**

The work in this chapter was recently accepted for publication in *Chemistry of Materials*. All experimental data shown were obtained by me, except the XRD which was obtained by Dr. Sandeep Kohli.

## 5.2 Abstract

A ternary oxide, containing cobalt, aluminum and iron and not previously known to be active for the photoelectrolysis of water, was identified using a high throughput combinatorial technique. The technique involves ink jet printing overlapping patterns of oxide precursors onto fluorine doped tin oxide conductive glass substrates. Subsequent pyrolysis yields patterns of mixed oxide compositions that were screened for photoelectrolysis activity by scanning a laser over the material while immersed in an electrolyte and mapping the photocurrent response. The composition and optimum thickness for photoelectrochemical response of the newly identified material was further refined using quantitative ink jet printing. Chemical analysis of bulk and thin film samples revealed that the material contains cobalt, aluminum and iron in a  $\text{Co}_3\text{O}_4$  spinel structure with Fe and Al substituted into Co sites with a nominal stoichiometry of  $\text{Co}_{3-x-y}\text{Al}_x\text{Fe}_y\text{O}_4$  where  $x$  and  $y$  are about 0.18 and 0.30 respectively. The material is a  $p$ -type semiconductor with an indirect band gap of around 1.5 eV, a value that is nearly ideal for an efficient single photoelectrode for water photoelectrolysis. Photoelectrochemical measurements indicate that the onset of hydrogen evolution is about 0.9-V negative of the thermodynamic value but the photocurrent is limited by slow kinetics for hydrogen evolution.

## 5.3 Introduction

Efficient and inexpensive production of hydrogen from water and sunlight has been the “holy grail” of photoelectrochemistry since Fujishima and Honda first demonstrated the feasibility of the process with rutile crystals<sup>1-4</sup>. Realistically, however, single crystal oxide materials will most likely not be efficient or cost effective photoelectrolysis materials due to the expense of single crystal growth, the low absorption coefficients of metal *d-d* transitions and the low mobility of charge carriers in metal *d*-bands. Nonetheless, nanostructured oxide semiconductors are promising materials for this purpose due to their inherent stability, increased absorption capabilities relative to bulk materials, and potential for low cost. A porous nanostructure of titanium dioxide has already proven to be worthwhile as a scaffold and electron collecting phase for dye sensitized photovoltaic devices that could potentially be highly efficient and made at low cost<sup>5, 6</sup> and a nanotubular TiO<sub>2</sub> morphology has substantially increased the efficiency of water photoelectrolysis using ultraviolet wavelengths<sup>7,8</sup>.

The nanostructuring of a metal oxide for solar photoelectrolysis provides several advantages. First, as mentioned above, it can be produced at low cost. Second, as in a dye-sensitized solar cell, all photons are eventually absorbed and the photogenerated carriers are produced near an interface where the photoelectrolysis reactions occur and so high carrier mobilities are not essential. Third, the lower microscopic current density of a high surface area nanostructured material will reduce the overpotential needed to drive

the oxidation and reduction of water at acceptable rates, resulting in higher conversion efficiencies. Lastly, a nanostructured oxide can be deposited on a transparent conducting substrate that allows for back illumination, as in the dye sensitized solar cell, reducing the scattering of the incoming solar radiation by bubbles generated at the electrode surface.

The roadblock for the realization of such a system has been that no semiconducting material is known that simultaneously satisfies all of the criteria needed for efficient photoelectrolysis: The material must be stable for many years under illumination in aqueous electrolyte solution, have a band gap within the range where it can absorb a large fraction of the solar photons (1.5-2.0 eV for a single photoelectrode system), have conduction and valence band positions that straddle the oxidation and reduction potentials of water and be catalytic for water reduction or oxidation<sup>9,10</sup>.

We believe that the material will most likely be an oxide semiconductor in order to be stable for many years in sunlight while immersed in an electrolyte. There are many oxide materials that have been evaluated for their ability to photoelectrolyze water<sup>10, 11</sup>.  $\alpha$ -Fe<sub>2</sub>O<sub>3</sub> has recently<sup>12-14</sup>, and in the past<sup>15</sup>, received a lot of attention for its water photooxidation activity, however its band gap (2.2 eV) is larger than the optimum for a single band gap device to efficiently use the solar spectrum for water photoelectrolysis<sup>16</sup>. We contend that a more suitable oxide material will contain multiple metals that will each contribute to the required properties of stability, light absorption, and being catalytic for hydrogen or oxygen evolution. Therefore we developed a high throughput combinatorial approach to prepare and rapidly screen many multiple-metal containing oxides for

photoelectrolysis activity<sup>17</sup>. Briefly our method involves ink jet printing metal oxide precursors (to date primarily nitrate salts) in overlapping patterns onto conducting glass substrates. Subsequent pyrolysis of the substrate yields multiple oxide phases that can be screened for photoelectrolysis activity by measuring the photocurrent generated by scanning a laser over the material while it is immersed in an electrolyte. To date we have printed and screened almost 500 combinations of four metals taken three at a time and have identified a number of previously unrecognized materials that have photoelectrolysis activity. In this paper we discuss how we have developed a methodology to follow up on “hits” in the high throughput screening and attempt to understand and optimize a new material’s water photoelectrolysis activity.

## 5.4 Experimental

Precut fluorine-doped tin oxide coated glass (TEC 8, 8-ΩR, 3.0 mm thickness) was obtained from Pilkington Industries. CsNO<sub>3</sub>, Fe(NO<sub>3</sub>)<sub>3</sub>, Cu(NO<sub>3</sub>)<sub>2</sub>, Co(NO<sub>3</sub>)<sub>2</sub>, and Al(NO<sub>3</sub>)<sub>3</sub> were obtained from Sigma Aldrich (Fe, Cu, and Co) or Baker (Al) and were used as received. TiCl<sub>4</sub> packaged under argon was obtained from Alfa-Aesar and placed into an oxygen and moisture-free glovebox prior to opening. A 2-M aqueous solution (which is surprisingly stable under ambient conditions) of the titanium precursor was prepared by filling a syringe with the appropriate amount of TiCl<sub>4</sub> in the glovebox and carefully adding it dropwise to distilled water immersed in an ice bath with continuous

stirring. This aqueous solution was diluted to the same concentration as the other precursors, 0.5-M, just prior to printing.

The triangular gradient ink jet patterns were produced as described previously using a Hewlett Packard Deskjet 1220C thermal ink jet printer<sup>17</sup>. The combinatorial template with quantitative stoichiometries was printed with a Fujifilm Dimatix Model DMP-2800 piezoelectric ink jet printer. A formulation suitable for the Dimatix inkjet printer used solutions of the appropriate metal nitrate salts (0.50 M) with 35%, by volume, diethylene glycol and 1%, by volume, diethylene glycol monobutyl to serve the respective roles of viscosity agent and surfactant. The solutions were sonicated for 10 minutes to insure complete dissolution and were then injected through a 2-mm syringe filter into empty 10-pL drop volume Fujifilm Dimatix printer cartridges. Prior to printing, a cleaning cycle was run on each cartridge to ensure that printing was uniform as verified by a print head camera that is built into the Fujifilm Dimatix printer. The printer also allows an accurate determination of drop volumes, the number of nozzles firing, the piezoelectric jetting waveform for individual nozzles, and the frequency of nozzle firing, all important for a quantitative determination of the amount of each component printed within the combinatorial template. Prior to printing the glass was soaked in a piranha solution followed by rinsing with copious amounts of distilled water. The SnO<sub>2</sub>:F glass was then taped to the printer platen that was heated to 50 °C. Methanol was rubbed onto the substrate to make it slightly hydrophobic in order to minimize spreading of the “inks” and to maintain separation between the printed squares. The

metal precursor solutions were often over printed up to three times in order to achieve the appropriate metal oxide thickness.

The printed metal precursor patterns were then pyrolyzed in air for approximately 2 hours at 500 °C in a ThermoLyne Type 1300 furnace to convert the precursors into metal oxides. For initial screening of the metal oxide candidates, the printed films were connected to a Princeton Applied Research 174A Potentiostat as the working electrode with a platinum basket functioning as both the counter and reference electrodes in a two-electrode configuration. A 0.10-M NaOH solution was typically used as the electrolyte. The sample was irradiated with a 532 nm frequency doubled Nd:YAG laser (model LAGR20 from Information Unlimited) with a beam diameter of ca 1-mm and a typical illumination intensity of approximately 2500 mW/ cm<sup>2</sup>. The laser beam was modulated with a PTI OC-4000 chopper operating at 31-Hz and was rastered over the film by applying stepwise voltages to a two-mirror galvanometer (CLS-200 from Intelite, Inc). The resulting photocurrent at each pixel (generally around 10 μA/cm<sup>2</sup> at short-circuit, zero bias for the working materials) was measured after 300-ms illumination times with a Stanford Research Systems SR530 Model Lock-In Amplifier and this data was used to generate the false color photocurrent images.

Glancing angle X-ray diffraction (GAXRD) measurements were performed with a Bruker D-8 Discover instrument using Cu K-α radiation. GAXRD measurements were performed in the 2Theta range from 5-80 degrees, at an angle of incidence of 0.5 degree, a step size of 0.02 degree, and time-per-step of 10-s. Search match analysis for

identification of crystalline phases was performed using Bruker EVA software. Bulk samples for powder X-ray diffraction were prepared by mixing the appropriate amounts of nitrate salts to a total concentration of 0.5-M in distilled water with 35%, by volume, diethylene glycol and 1%, by volume, diethylene glycol monobutyl ether and pyrolyzing at 500°C. Powder X-ray diffraction measurements were performed by using a Scintag-X2 diffractometer equipped with a Peltier detector and Cu-X-ray tube. XRD scans were performed over the 2Theta range from 5-80 degrees with a step of 0.02 degree and time-per-step of 1-s. Photocurrent spectroscopy was done using an apparatus that has been described previously<sup>18</sup> while SEM and EDS images were taken with a field emission JEOL 6500F electron microscope.

Larger area photoelectrodes were made by printing from a cartridge containing a solution of precursors mixed at the optimized bulk catalyst composition onto mica substrates coated with evaporated layers of Au (250-nm) with a 50 nm Cr adhesion layer. Current voltage analysis was performed with a computer-controlled CompactStat potentiostat made by Ivium Technologies using a saturated sodium calomel electrode (SSCE) as the reference electrode and a platinum basket as the counter electrode. The sweep rate was 0.5 mV/ s for the electrodes immersed in a 0.1-M NaOH solution deoxygenated with nitrogen. The sample was irradiated with a 150 W Xe arc lamp for the photocurrent-voltage curves. The lamp was placed approximately 25-cm from the sample as this was the optimum working distance for focusing the unfiltered light onto the 2.5-cm x 2.5-cm printed sample. Platinization was accomplished by sweeping the

potential of the illuminated electrode at 5 mV/s for six cycles between +0.1-V and -0.3-V vs SSCE in a deoxygenated pH 4 acetic acid/sodium acetate buffer containing 100-mM  $\text{H}_2\text{PtCl}_6$ .

## 5.5 Results and Discussion

We have used a consumer level ink jet printer to print and screen hundreds of different material combinations using the four-metals-taken-three-at-a-time pattern used to screen fuel cell catalysts<sup>19</sup>. Most of the material combinations show no or very little photoresponse while a few have performed significantly better than the internal reference materials ( $\alpha\text{-Fe}_2\text{O}_3$  and CuO for *n*- and *p*-type photoactivity, respectively<sup>20</sup>). One of the materials discovered in our search has reproducibly shown substantial *p*-type photactivity. Figure 1 shows the photocurrent map done in 0.1-M NaOH without an externally applied bias of a “four-metals-three-at-a-time” printed and fired film using Fe, Co, Al and Cs. The dark regions represent areas where the photocurrent is in the anodic direction whereas the bright regions show areas of *p*-type photocurrent response that are 2 to 2.5 times larger than the CuO internal standard (upper left triangle). The regions of high activity are found in the Co rich regions of the Co-Al-Fe and Co-Al-Cs triangles. Although we can tell from the gradient printing that the active phase is cobalt rich, the exact proportions of the metal components in the active mixture are unknown since we do not know the exact amounts of the various “inks” delivered by the printer driver software as its usual function has been optimized for visual aesthetics when printing conventional inks.

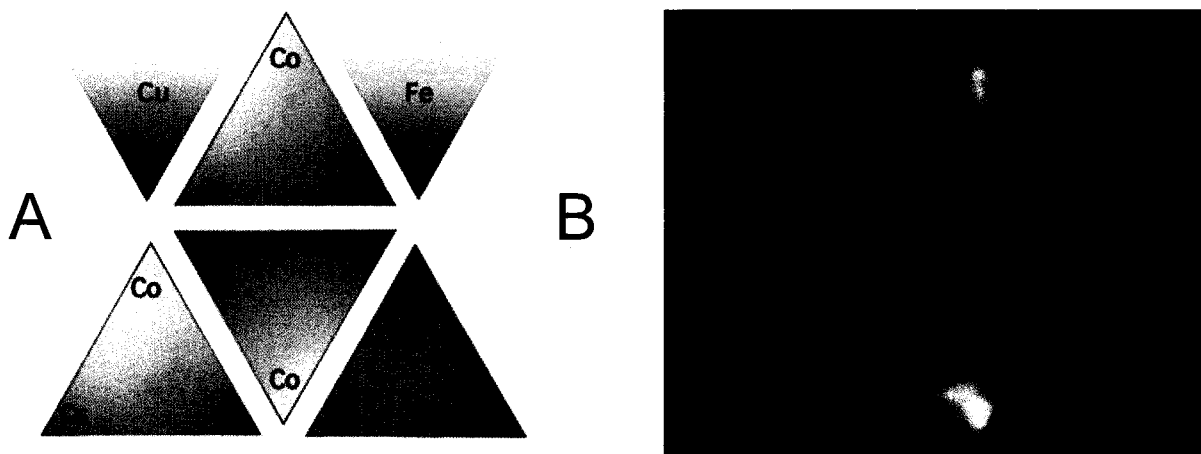


**Figure 5.1:** A. Template showing the gradient pattern used for printing the metal nitrate precursors for the Al-Co-Cs-Fe system (Fe and Cu triangles are internal standards for n- and p- type photoactivity, respectively). B. Laser screening at 532 nm with no applied bias in a 0.1-M NaOH solution. Qualitatively, it can be seen that the highest activity is associated with primarily Co and small amounts of Fe and Al. The printed triangles have a height of 1.9-cm.

To more quantitatively refine the composition of the photoactive phase we focused on the Co-Fe-Al containing semiconducting oxide and employed a research grade inkjet printer that allows quantification of the ink-jetted volumes and dot densities. A printing template was created, similar to patterns used for combinatorial phosphor discovery<sup>21, 22</sup>, where an array of squares is printed that each contain a predetermined amount of the three oxide precursors as shown in Figure 5.2A. The total amount of precursor deposited into each square is determined from the concentration of metal nitrate in the printing solution, the drop volume for a printed drop, the number of layers printed, and the number of drops ink jetted per unit area, an amount that is determined by the density of dots and the number of ink-jetting nozzles firing from each cartridge. A series

of the internal standards,  $\alpha$ -Fe<sub>2</sub>O<sub>3</sub> and CuO, of different dot densities (thicknesses) are also printed at the top of the pattern. In this pattern, four different densities of Co and Fe were printed as double horizontal and double vertical rows, respectively. Different amounts of Al were deposited in a repeating pattern within groups of four squares containing identical Fe and Co amounts as shown in the dashed inset in the upper left-hand corner of Figure 5.2A.

Controlling the density of the printed drops allows the production of a broad or narrow compositional range containing known stoichiometries within each square when the other factors mentioned above are held constant. Table 5.1 contains the values of drop spacing and density used in Figure 5.2 for the Fe and Cu internal standards and the Fe-Co-Al Oxide precursors. For illustrative purposes, the bottom square on the far left, labeled Fe<sub>D</sub>Co<sub>A</sub>Al<sub>B</sub>, was printed with a drop spacing of 40  $\mu$ m, 160  $\mu$ m, and 120  $\mu$ m for Fe, Co, and Al, respectively. The drop density is then calculated by dividing the area of the square (9 mm<sup>2</sup>) into the corresponding number of drops of each material printed within that square with small corrections when the width of the square is not an integer value of the drop spacing. As the relative stoichiometry of each material would be directly proportional to the relative density of material deposited, this square corresponds to a nominal stoichiometry of Fe<sub>14.4</sub>Co<sub>1</sub>Al<sub>1.7</sub>. As another example, the brightest square in Figure 5.2B, third square from the right, third row down, is given the label Fe<sub>B</sub>Co<sub>D</sub>Al<sub>A</sub> which correlates to Fe<sub>1.7</sub>Co<sub>14.4</sub>Al<sub>1</sub> (In atomic percentages 10% Fe, 84% Co, and 6% Al) and this composition was used in future experiments where bulk samples were prepared.

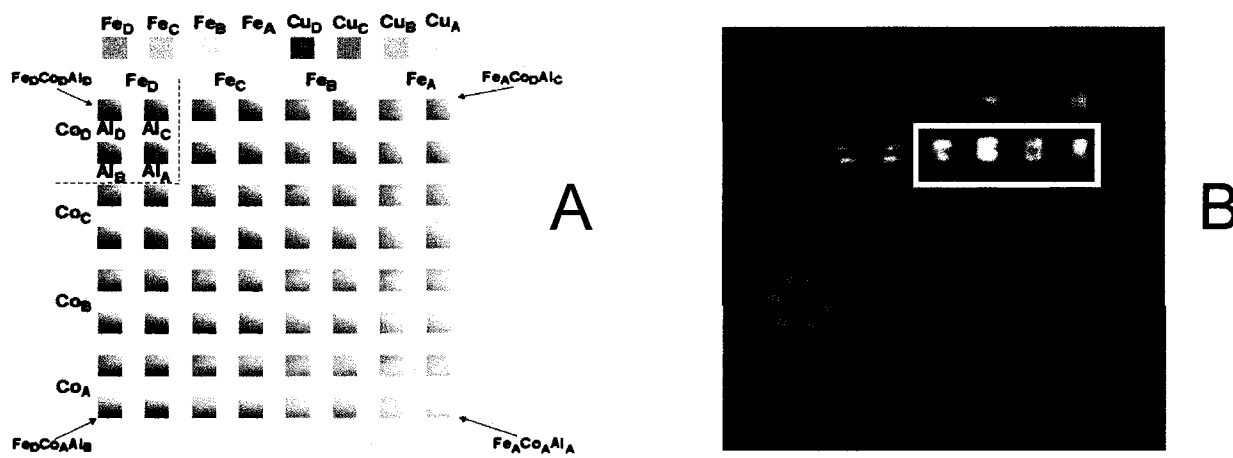


**Figure 5.2:** A. Printing template used for quantifying the optimal stoichiometry in the Co-Al-Fe system where known amounts of the components are printed into individual 3 mm x 3 mm squares. The density of precursor drops (and the resulting stoichiometry) is shown in Table 1. B. False color photocurrent map with no applied bias at 532 nm in a 0.1-M NaOH solution. The cathodic photocurrent measured by laser scanning the brightest square of the film is nearly three times that generated by the best pure CuO internal standard labeled Cu<sub>D</sub>. The compositions within the solid white box were expanded in Figure 5.3. The materials within the dashed blue and dotted orange circles were used for the action spectra shown in Figure 5.4.

**Table 5.1:** Density of printed precursor drops used to produce the mixtures shown in Figure 5.2.

Label	One-Dimensional Drop Spacing ( $\mu\text{m}$ )	Drops per $\text{mm}^2$	Relative Stoichiometry
A	160	45	1
B	120	75	1.7
C	80	169	3.7
D	40	642	14.4

To further refine the optimal composition of the photocatalyst, another template was created that encompasses stoichiometries outlined by the white box in figure 5.2B as well as some similar stoichiometries. The template, and the result of the photocurrent screening, is shown in Figure 5.3. In this pattern the amount of cobalt was kept constant (labeled  $\beta$  in the figure with a drop spacing equal to that of all mixtures within the white box of figure 5.2B) while the Fe and Al contents (labeled w, x, y, and z) were varied and calculated using the rationale described previously. The internal standards were printed with the same drop densities described in Table 5.1 as A, B, C, D (note that the overall amount of printed internal standard material relative to the working mixtures is approximately the same between Figures 5.2 and 5.3 in order to not overestimate the contribution of sample thickness to performance). The resulting photocurrent is within  $\pm 20\%$  for all squares indicating flexibility in the stoichiometries of photoactive compositions. Indeed, the Fe and Al content can vary by as much as a factor of two (between  $\text{Co}_{17.8}\text{Fe}_1\text{Al}_{2.1}$  and  $\text{Co}_{17.8}\text{Fe}_{2.1}\text{Al}_1$ ) and still produce a material with comparable photoactivity.

The band gaps of the photoactive materials can be determined by measuring the photocurrent spectrum of the individual printed areas. Figure 5.4B shows *normalized* photocurrent spectra for several compositions identified in Figure 5.4A and illustrates that the iron-rich compositions have a photocurrent onset of about 2.2 eV, consistent with

$\alpha$ -Fe<sub>2</sub>O<sub>3</sub> being the active phase in these regions (note the photocurrent in this case was anodic). The gradual onset of the photocathodic current with increasing photon energy

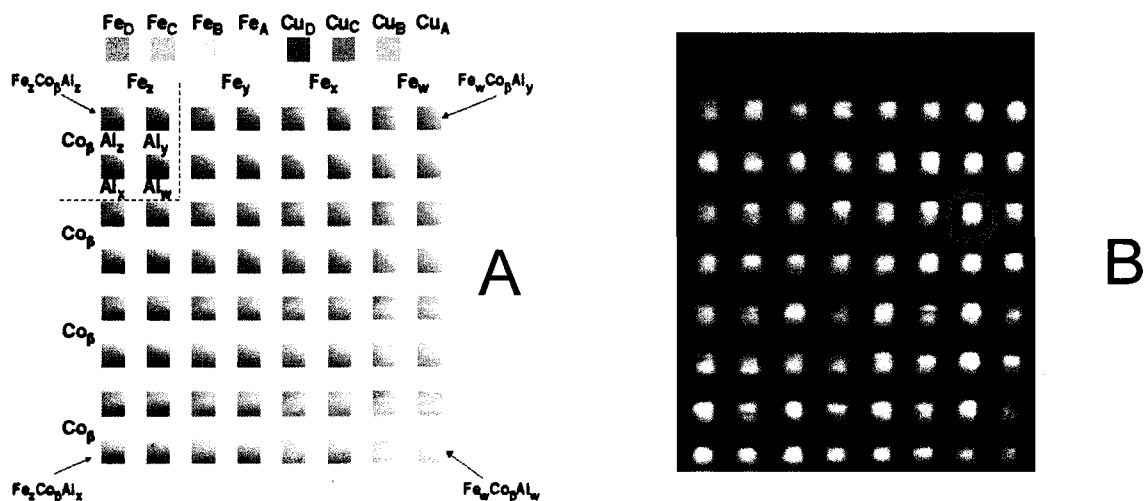


**Figure 5.3:** Compositional library produced by expansion of the compositional region outlined by the white box in Figure 5.2. The template shown in A was created by including all of the mixtures created within the inset of Figure 1 as well as some intermediate stoichiometries. The actual densities are shown in Table 2, while the pure Fe and Cu internal standards were printed as in Figure 2. B. Photocurrent map of the array of 3 mm x 3 mm squares measured in 0.1-M NaOH with a 532-nm laser. The compositions within the solid green and dashed-dotted red circles were used for the action spectra shown in Figure 4.

**Table 5.2:** Density of printed precursor drops used to produce the mixtures shown in Figure 5.3.

Label	One Dimensional Drop Spacing ( $\mu\text{m}$ )	Drops per $\text{mm}^2$	Relative Stoichiometry
w	180	36	1
x	160	45	1.25
y	140	54	1.5
z	120	75	2.1
$\beta$	40	642	17.8

for the Co-Al-Fe phase indicates that the band gap is indirect and this is confirmed by plotting  $(\text{IPCE})^{0.5}$  against photon energy where a linear dependence with an intercept of about 1.5 eV is obtained (inset of Figure 5.4). Since the printed film is so thin, we assume that the photocurrent, and subsequently the IPCE, is directly proportional to the absorption coefficient ( $\alpha$ ) for the material and that carrier diffusion length plays no role in the photocurrent. The band gap of the new *p*-type phase appears to be essentially independent of composition over the range  $\text{Co}_{3.7}\text{Al}_1\text{Fe}_1 - \text{Co}_{17.8}\text{Al}_{2.1}\text{Fe}_1$ . There are several interpretations for this observation. Either there is a very stable stoichiometry that forms even when there is an excess of one or two of the components present and variations in the photoresponse are the result of variations in the doping level of this phase or the band gap is not a strong function of the Fe or Al content of the phase in this composition region.

Once the near optimum initial composition was determined (~84% Co, 10% Fe, and 6% Al) a bulk solution containing a total metal ion concentration of 0.5M, including the appropriate amount of viscosity agent and surfactant, was prepared for printing. The combined solution was then printed onto a  $\text{SnO}_2\text{:F}$  substrate and fired in a furnace at 500 °C for two hours. A larger volume was also pyrolyzed at the same temperature to prepare a bulk powder sample. The printed film was examined with glancing angle x-ray diffraction and the bulk sample with powder x-ray diffraction as shown in Figure 5.5. Diffractograms from both methods show the same lines with additional lines from the tin oxide substrate appearing in the thin film sample. Indexing the x-ray pattern reveals that

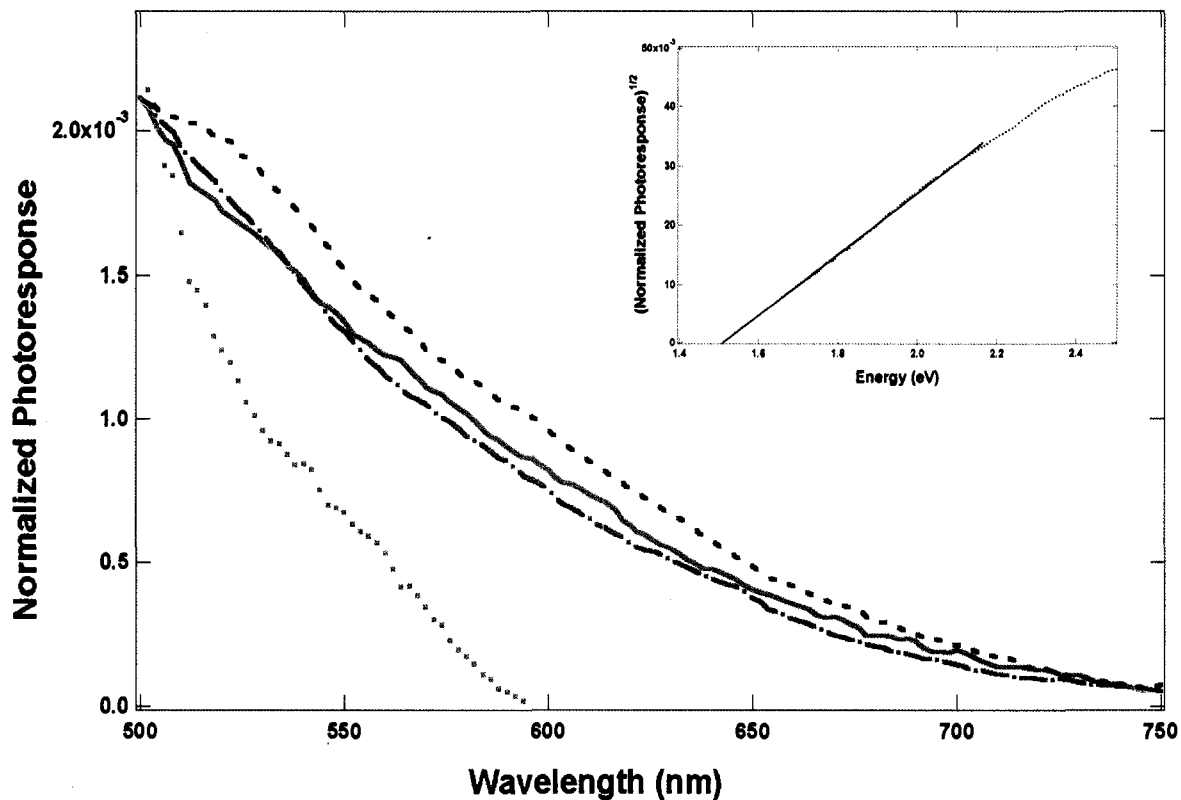


**Figure 5.4:** Action spectra normalized to a constant value at 500-nm for the dotted orange data and dashed blue data obtained from the compositions outlined in figure 5.2 and the solid green and dashed-dotted red data obtained from the compositions outlined in figure 5.3. The direction of the photocurrent was also inverted for the iron rich composition (outlined by the orange dotted circle in Figure 5.2). The inset shows a linear extrapolation to approximate the band gap of the *p*-type materials from the average IPCE values fit to an indirect transition.

the material has the same x-ray pattern as  $\text{Co}_2\text{AlO}_4$ <sup>23</sup>,  $\text{CoAl}_2\text{O}_4$ <sup>24</sup> and  $\text{Co}_3\text{O}_4$ <sup>25</sup>. Surprisingly there are only very small shifts (0.1-0.2 degrees) in the major diffraction peaks for all of these compounds where  $\text{Al}^{3+}$  substitutes for  $\text{Co}^{3+}$  in  $\text{Co}_3\text{O}_4$  through the entire composition range to  $\text{CoAl}_2\text{O}_4$ <sup>26, 27</sup>. Since the shifts are so small x-ray diffraction does not provide a good estimate of the amount of Al substitution into our cobalt rich active phase. Iron substituting into the  $\text{Co}_3\text{O}_4$  phase for either  $\text{Co}^{3+}$  or  $\text{Co}^{2+}$ , due to its similar ionic radius, would also not shift the diffraction peaks very much. Due to iron having one fewer electron than cobalt, it may be acting as a dopant and imparting the *p*-type behavior. Noticeably absent in the diffractogram are peaks assignable to either  $\alpha$ - $\text{Fe}_2\text{O}_3$  or  $\text{Al}_2\text{O}_3$ , suggesting that iron may replace some cobalt in the lattice or the presence of amorphous oxide phases for the remaining constituents within the sample.

Recent theoretical work performed by Walsh et al.<sup>28</sup> on a number Co-Al-Fe spinel stoichiometries predicts that the electronic band gap of  $\text{Co}_3\text{O}_4$  remains largely unchanged as Al is substituted for cobalt into the lattice to form  $\text{Co}_2\text{AlO}_4$  but does increase noticeably for  $\text{CoAl}_2\text{O}_4$  as the all octahedral metal sites are replaced with Al. Additionally,  $\text{CoAl}_2\text{O}_4$  has been identified as a likely direct gap binary oxide candidate with properties suitable for photoelectrolysis if its otherwise large band gap is reduced by, for example, doping, local cation disorder, or crystal defects. The potential role of Fe to induce such changes appears to be corroborated by experiments where samples prepared with only Co-Al binary oxide compositions showed lower photoactivity than the optimal stoichiometry by more than a factor of two.

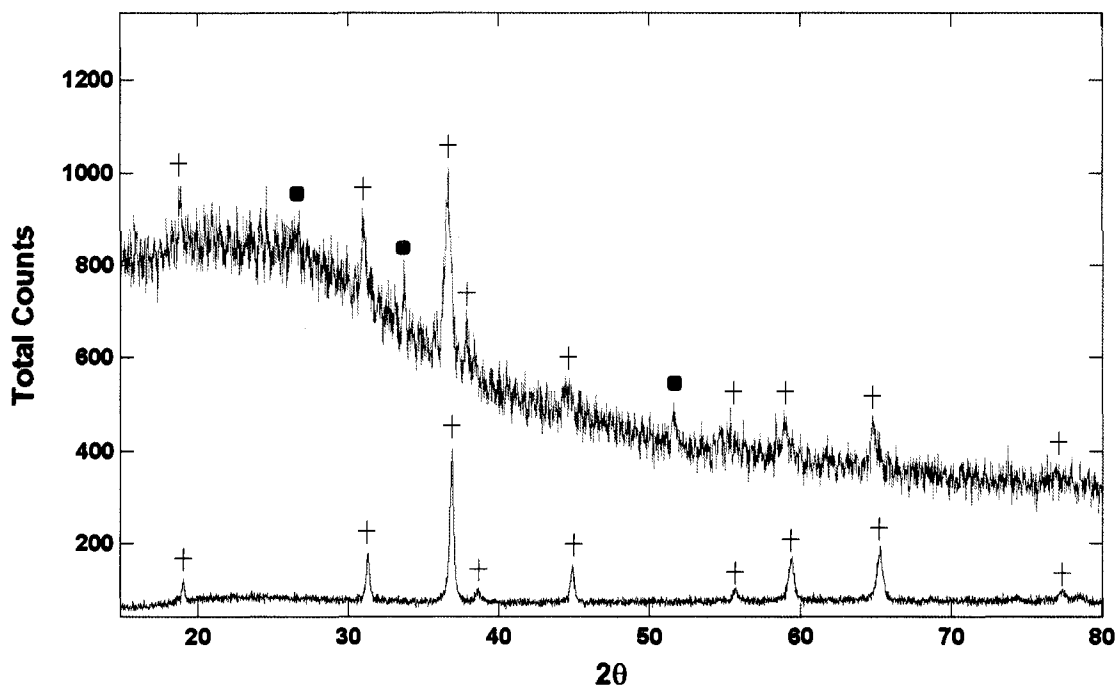


**Figure 5.5:** Glancing Angle XRD (top curve in red) for a film printed onto a fluorine-doped tin oxide substrate and powder XRD for the 84% Co, 10% Fe, and 6% Al bulk sample (bottom in blue). The 2Theta axis was truncated in order to display the flatter regions of the GAXRD curves and because no features were present below that range. The filled circles are the major peaks corresponding to tin oxide while the crosses correspond to the major peaks for  $\text{Co}_3\text{O}_4$  and/or  $\text{Co}_2\text{AlO}_4$  to  $\text{CoAl}_2\text{O}_4$ .

To further optimize the performance of the Co-Fe-Al oxide system we prepared cartridges containing the nitrate salts near the optimal composition ratio with a total concentration of 0.50M. The single cartridge could then be used to print different spot densities or to print multiple layers in order to vary the thickness of the resulting multicomponent oxide film. Figure 5.6 shows the results of such a study.

Assuming that the density of the final material is close to that of  $\text{Co}_3\text{O}_4$ , we can estimate the sample thickness shown in Figure 5.3. The area labeled 1 is the thickest film and shows very little photocurrent except for the thinner areas around the periphery. The printed area labeled 2 is the best thickness produced in this experiment since it has the highest photocurrent yield. The thickness of the film is further decreased from areas 3 and 4 in the figure and the photocurrent also decreases.

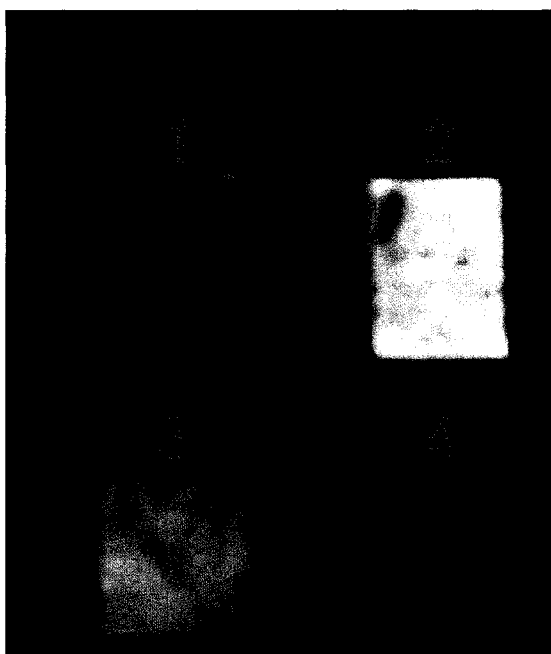


**Figure 5.6:** Thickness optimization for the optimized stoichiometry printed onto a fluorine-doped tin oxide substrate. The four larger squares were printed with the differing dot densities (shown in Table 3) inside of 1.5 cm x 1.5 cm squares. Each was printed from a single cartridge containing, in atomic percentages, 84%Co, 10% Fe, and 6% Al. The iron and copper internal standards (smaller squares at the top of the image) were printed as in Figures 5.2 and 5.3. The photocurrent mapping was done in 0.1 M NaOH at 532 nm. See the text for a more complete description.

**Table 5.3:** Drop spacing and calculated average thickness for the four squares printed and mapped for photoactivity in figure 5.6.

Label	One Dimensional Drop Spacing ( $\mu\text{m}$ )	Drops per $\text{mm}^2$	Calculated Average thickness (nm)
1	10	10,013	560
2	30	1,115	60
3	50	403	24
4	70	205	12

Another advantage of printing optimized films from a single cartridge is that it provides a method for adding a fourth component to the material. Figure 5.7 shows an example of adding a fourth metal to our optimized composition. Of course we are only sampling a line within a complex four-dimensional phase diagram but such a study may still reveal even more directions for optimizing composition. In Figure 5.7 a small alkali metal cation (Li), a large alkali cation (Cs), some metal ions with ionic radii near that of Co and Fe (Mg, Zn) and Ti were added to the optimal composition. The upper row of five squares is the optimized ternary Co-Fe-Al phase and the fourth component has decreasing concentrations in the lower squares. It is clear that in this case the fourth component decreases the photoresponse in all cases except for the smallest added amounts that have very little effect on the photoresponse. This technique could also be used for adding a catalyst layer by firing the optimal composition before printing a layer of catalyst for water oxidation or reduction that can itself be optimized for thickness and composition.

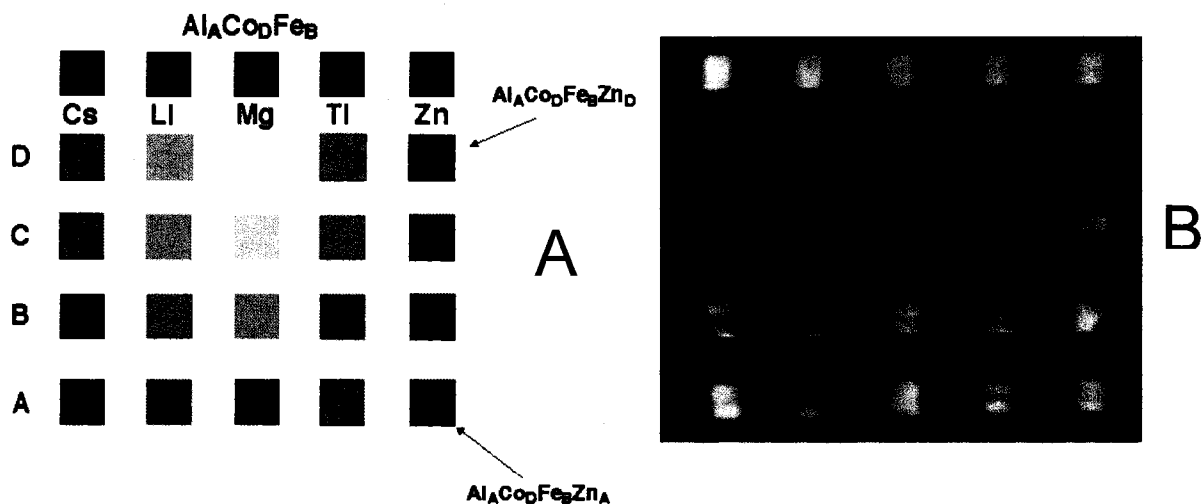


**Figure 5.7:** Adding a fourth component to the optimized ternary composition into individual 4 mm x 4 mm squares. A. Template used for mixing Cs, Li, Mg, Ti and Zn with the optimized Al, Co, and Fe stoichiometry discussed earlier. The letters correspond to the same drop densities as in Figure 2. B. Photocurrent map of the compositions in 0.1-M NaOH using a 532-nm laser.

Larger area films near optimal composition and thickness were then printed to measure their current-voltage behavior. Although deposition of the material onto the usual fluorine-doped tin oxide substrate would have been consistent and convenient, there were problems with this substrate when polarized in electrolytes at cathodic potentials. We eventually determined that the reduction and reoxidation of the tin oxide underlayer during potential cycling in the electrolyte led to delamination of the printed film from the transparent conductive oxide surface, perhaps due to lattice strain at the interface. After trying a number of other substrates, evaporated gold on mica, with a thin chromium adhesion layer, showed the best behavior for printed film adhesion, low dark currents and electrochemical stability. Evaporated Au on mica films are known to give a flat,

polycrystalline but predominately (111) orientated film<sup>29</sup>. The morphology of the pyrolyzed film was significantly different on Au than it is on FTO as can be seen in the SEM images on the two substrates in Figure 5.8. The film printed and fired on the Au substrate is discontinuous and, based upon the drop spacing set within the printer software as compared to the spacing of the catalyst islands seen in the SEM, it appears that a number of printed drops coalesce during annealing and do not wet the gold substrate. We estimate that less than 50% of the area of the gold layer is covered by the photocatalyst. EDS analysis (see supporting information) of the dark and light regions of figure 5.6B confirm that the catalyst is confined to the dark islands and that the expected metal stoichiometry is measured within the islands. The film appears to be more continuous when printed on FTO but has a more porous appearance at higher magnifications.

The films printed onto Au on mica were stable for multiple voltammetric cycles in basic electrolytes and so the dark and photocurrent response for hydrogen evolution was investigated in deoxygenated 0.1 M NaOH solution. Less than 40  $\mu\text{A}/\text{cm}^2$  of dark current was generated near the onset for dark hydrogen production (-0.98 V vs SSCE). When the printed area containing the photocatalyst is illuminated a photocurrent onset at about -0.10 volts is observed with a plateau region followed by an increase in the photocurrent as the thermodynamic potential for the onset of dark hydrogen production is reached. The photocurrent onset indicates an onset of hydrogen evolution about 0.9 volts positive of the thermodynamic potential in 0.1M NaOH, very respectable for a material

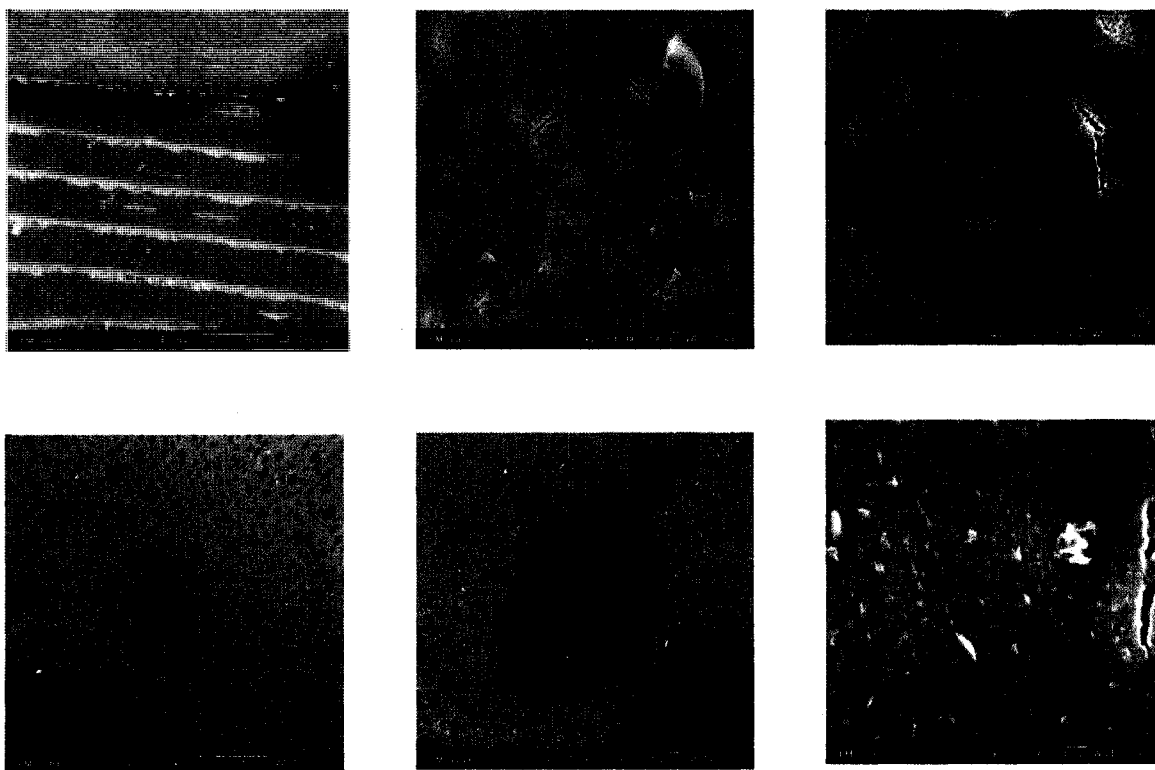


**Figure 5.8:** SEM images at different magnifications for the film used for measurement of the current-voltage curves (below) and sample printed on FTO (above). Substrate wetting and morphology are clearly different for the two substrates. EDS results confirm the designed and printed atomic percentages of Co, Fe, and Al within the dark islands of the bottom images.

with a band gap of 1.5 eV. The photocurrent near the thermodynamic potential of the hydrogen electrode is about  $170 \mu\text{A}/\text{cm}^2$  and remained steady (within  $\pm 0.5\%$ ) for illumination times of over thirty minutes.

Calculation of the total amount of charge collected due to photocurrent at short circuit is about an order of magnitude greater than needed for the complete reduction of the deposited oxides to their metallic form indicating that the material is catalytic for

photoreduction of water since water is the only reducible species present in the electrolyte.

The poor fill factor in the power curve for hydrogen production could be due to poor electrode kinetics for the hydrogen evolution reaction. Previously photocathodes with little catalytic activity for hydrogen evolution could be significantly improved by the deposition of Pt nanoparticles onto their surface<sup>16, 30, 31</sup>. In an attempt to produce more photocurrent for hydrogen production, the sample was immersed into a platinizing solution and islands of Pt metal were deposited by illuminating the electrode during six

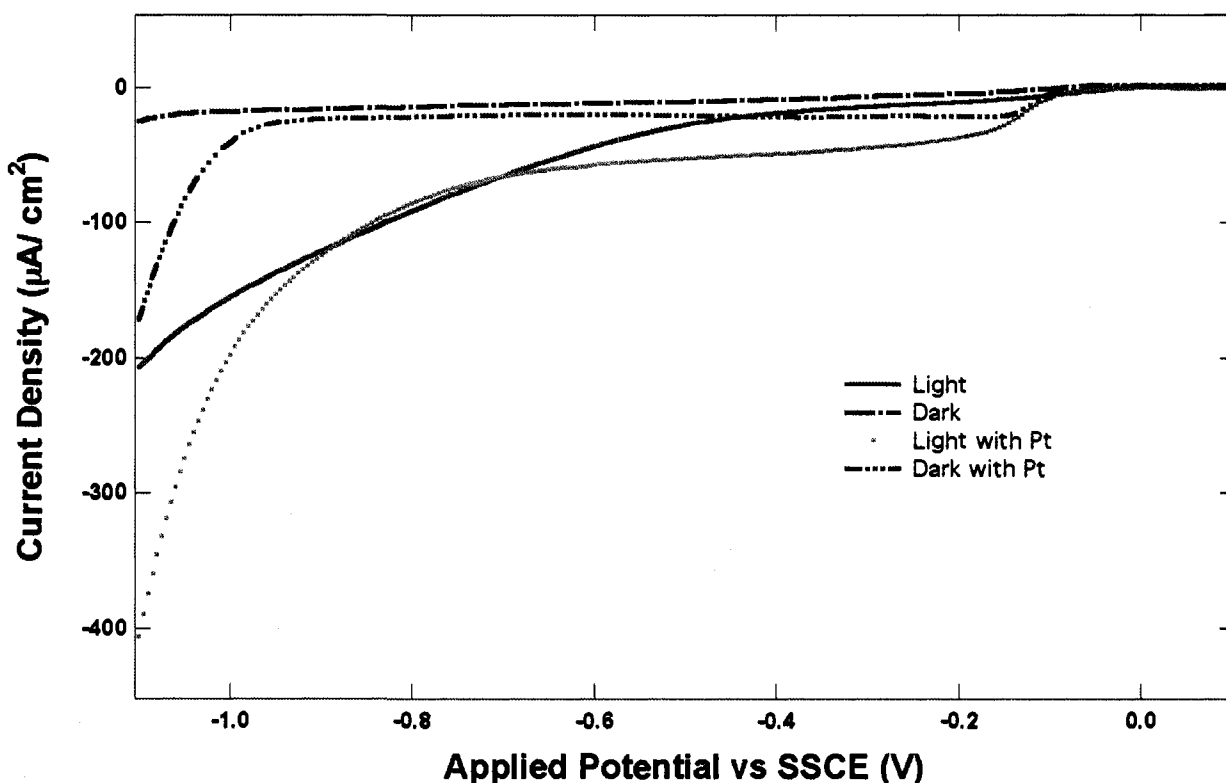


**Figure 5.9:** Dark and photocurrent-voltage curves for a 2 cm x 2 cm film printed onto a gold-on-chromium-on-mica substrate immersed in deoxygenated 0.1-M NaOH. The sweep rate was 0.5 mV/s. Illumination is from a 150 W Xe lamp. Platinization was done by immersing the electrode in a pH 4 acetic acid/ sodium acetate buffer containing 100- $\mu$ M  $H_2PtCl_6$  and cycling three times between -0.3 and +0.1 V vs SSCE at a sweep rate of 5 mV/s.

cyclic voltammetry cycles from 0.1 to -0.3 volts. Upon re-immersing the sample into the NaOH solution, the photocurrent was observed to increase as the platinum deposition reduced the overpotential needed for hydrogen production both in the light and in the dark as can be seen by the earlier onset of bulk hydrogen production. The increase and plateau of the photocurrent in the potential region between -0.2 and -0.6 may be due to the presence of catalytic sites for hydrogen evolution but the smaller photocurrent compared to the response at -0.9 indicates that the Pt catalyst is not optimally configured to supply a catalytic path for all photogenerated carriers. Photocurrents at both of these potentials are dependent on the light intensity and so the rate of the catalytic reaction through the catalytic sites is not rate limiting. Further work is needed to optimize the size and distribution of Pt on the surface to improve the photogenerated hydrogen evolution.

The incident photon to current efficiency on the printed films is very low (on the order of  $10^{-6}$  -  $10^{-5}$  when using a high power 532-nm laser in a short-circuit two electrode configuration) because, in addition to the poor hydrogen generation kinetics, we purposely print very thin layers of material where most of the incident photon flux passes through the film and is not absorbed or, in the case of the films printed on Au, is reflected from the regions where there is no film (Figures 5.8C and 5.8D). Thin nanostructured films reduce the influence of carrier transport on the measured photocurrent. Carrier mobilities in transition metal oxides are quite low and, when coupled to the low absorption coefficients associated with forbidden d-d optical transitions, would result in

low carrier collection in even a single crystal of a semiconducting photoelectrode. Therefore a thick high surface area nanocrystalline film, reminiscent of the dye sensitized solar cell, will most likely be the most efficient and cost-effective way to configure a photoelectrolysis device based on transition metal oxides. In this configuration the film will be thick enough to absorb all of the light and the size of the particles will be near or smaller than the carrier diffusion length resulting in all of the photogenerated carriers making it to the electrolyte interface to carry out the photoelectrolysis reactions. Therefore the optimization of the configuration of a combinatorially discovered photoelectrolysis system is the second, and equally challenging, step in building a practical system. However, as previously discussed, the purpose of this paper is not to configure the newly discovered photocatalysts for optimum efficiency but rather to investigate the path from discovery of an oxide semiconductor to understanding both the optimal composition, photoelectrochemistry, stability and the solid state chemistry of the newly discovered materials.

## 5.6 Conclusions

We have developed a methodology to discover new materials useful for the photoelectrolysis of water. In this paper we concentrated on determining the optimum composition and solid-state structure of one newly identified potential photocatalyst. The material contains cobalt, aluminum and iron in a  $\text{Co}_3\text{O}_4$  spinel structure with Fe and Al substituted into Co sites with a nominal stoichiometry of  $\text{Co}_{3-x-y}\text{Al}_x\text{Fe}_y\text{O}_4$  where  $x$  and  $y$  are about 0.18 and 0.30 respectively. It is a  $p$ -type semiconductor with an indirect band gap of around 1.5 eV, a value that is nearly ideal for the efficient single photoelectrode photoelectrolysis of water. This new cobalt iron aluminum oxide is most likely not the “holy grail” of photoelectrochemistry that we seek. Nonetheless, concentrating efforts on newly discovered lower band gap oxides appears to be a fruitful endeavor and our methodology gives a rational approach for future discovery and optimization of such materials. Our results have highlighted the difficulty of developing a new material from its discovery to its deployment in an optimized, efficient and useful device. Not only will the composition and nanostructure need to be optimized but, in addition, inexpensive, stable, and perhaps transparent substrates that are compatible with the material’s morphology and chemical makeup must also be found.

## Acknowledgements

This work was supported by the Office of Basic Energy Sciences of the United States Department of Energy under Grant# DE-FG02-05ER15750. We thank Dr. Sandeep Kohli for assistance with the x-ray diffraction experiments. Helpful discussions and theoretical work done by John Turner, Yanfa Yan, Aron Walsh, Su-Huai Wei, and M. M. Al-Jassim at NREL are acknowledged as is a discussion about the printed titanium precursor solution with Jordan Katz at the California Institute of Technology. Additionally, we are grateful to Greg Herman and David Punsalan with the Hewlett-Packard Corporation for continued discussions.

## References

1. Fujishima, A.; Honda, K., *Nature* **1972**, 238, 37-38.
2. Fujishima, A.; Honda, K., *Bull. Chem. Soc. Japan* **1971**, 44, 1148-1150.
3. Fujishima, A.; Kohayakawa, K.; Honda, K., *J. Electrochem. Soc.* **1975**, 122, 1487.
4. Gratzel, M., *Nature* **2001**, 414, 338.
5. Nazeeruddin, M. K.; Kay, A.; Rodicio, I.; Humphry-Baker, R.; Muller, E.; Liska, P.; Vlachopoulos, N.; Gratzel, M., *J. Am. Chem. Soc.* **1993**, 115, 6382-6390.
6. Regan, B. O.; Gratzel, M., *Nature* **1991**, 353, 737.
7. Grimes, C. A., *J. Mater. Chem* **2007**, 17, 1451-1457.
8. Grimes, C. A., *Nanotechnology* **2007**, 18, (6).
9. Tan, M. X.; Laibinis, P. E.; Nguyen, S. T.; Kesselman, J. M.; Stanton, C. E.; Lewis, N. S., *Prog. Inorg. Chem.* **1994**, 41, 21-145.
10. Rajeshwar, K., *J. Appl. Electrochem.* **2007**, 37, 765-787.

11. Jarrett, H. S.; Sleight, A. W.; Kung, H. H.; Gilson, J. L., *J. Appl. Phys* **1980**, 51, (7), 3916-3925.
12. Cesar, I.; Kay, A.; Martinez, J. A. G.; Gratzel, M., *J. Am. Chem. Soc.* **2006**, 128, 4582-4583.
13. Duret, A.; Gratzel, M., *J. Phys. Chem. B* **2005**, 109, 17184-17191.
14. Kay, A.; Cesar, I.; Gratzel, M., *J. Am. Chem. Soc.* **2006**, 128, 15714-15721.
15. Leygraf, C.; Henderwerk, M.; Somorjai, G. A., *J. Phys. Chem.* **1982**, 86, 4484-4485.
16. Heller, A., Hydrogen Evolving Solar Cells. *Science* **1984**, 223, 1141-1148.
17. Woodhouse, M.; Herman, G.; Parkinson, B. A., *Chem. Mater.* **2005**, 17, 4318.
18. Takeda, N.; Parkinson, B. A., *J. Am. Chem. Soc.* **2003**, 125, 5559-5571.
19. Reddington, E.; Sapienza, A.; Gurau, B.; Viswanathan, R.; Sarangapeni, S.; Smotkin, E. S.; Mallouk, T. E., *Science* **1998**, 280, (5370), 1735.
20. Koffyberg, F. P.; Benko, F. A., *J. Appl. Phys* **1982**, 53, (2), 1173-1177.
21. Danielson, E.; Devenney, M.; Giaquinta, D. M.; Golden, J. H.; Haushalter, R. C.; McFarland, E. W.; Poojary, D. M.; Reaves, C. M.; Weinberg, W. H.; Wu, X. D., *Science* **1998**, 279, 837-839.
22. Wang, J.; Yoo, Y.; Gao, C.; Takeuchi, I.; Sun, X.; Chang, H.; Xiang, X.-D.; Schultz, P. G., *Science* **1998**, 279, 1712-1714.
23. *International Centre for Diffraction Data*. Newton Square, PA, JCPDS-ICDD Card No. 38-814; p JCPDS-ICDD Card No. 44-160.
24. *International Centre for Diffraction Data*. Newton Square, PA, JCPDS-ICDD Card No. 44-160; p JCPDS-ICDD Card No. 44-160.
25. *International Centre for Diffraction Data*. Newton Square, PA, JCPDS-ICDD Card No. 42-1467; p JCPDS-ICDD Card No. 44-160.
26. Stangar, U. L.; Orel, B.; Krajnc, M., *J. Sol-Gel Sci. Tech.* **2003**, 26, 771-775.
27. Zayat, M.; Levy, D., *Chem. Mater.* **2000**, 12, 2763-2769.
28. Walsh, A.; Wei, S.-H.; Yan, Y.; Al-Jassim, M.; Turner, J. A.; Woodhouse, M.; Parkinson, B. A., *Phys. Rev. B*, **2007**, 76, 165119.

29. Higo, M.; Fujita, K.; Tanaka, Y.; Mitsushio, M.; Yoshidome, T., *Appl. Surf. Sci.* **2006**, 252, (14), 5083-5099.
30. Heller, A.; Aharon-Shalom, E.; Bonner, W. A.; Miller, B., *J. Am. Chem. Soc.* **1982**, 104, 6942.
31. Deutsch, T.; Koval, C. A.; Turner, J. A., *J. Phys. Chem. B* **2006**, 110, 25297-25307.

## Chapter 6

### Ongoing and Developing Work: Spatial Mapping of the Absorbed-Photon-to-Current Collection Efficiency

The values recorded for the incident-photon-to-current conversion efficiency (IPCE) for all laser scanning measurements have typically been very low. Specifically, at zero applied bias, these efficiencies have been on the order of  $10^{-5}$  for the lowest functioning, but still detectable, printed materials to  $10^{-3}$  for the best films deposited by spray pyrolysis. Although these low values might make it seem at first that the materials are not worthy of further investigation, several important points are in order. The printed films are very thin, a better morphology and crystallinity (which has *dramatic* effects upon performance even for the same material<sup>1-3</sup>) is not yet addressed, and the majority of the high-intensity laser light, typically tens of mW, passes directly through the material.

To resolve the discrepancy in efficiencies between the sample preparation methods (i.e. printed films and more strongly absorbing films produced vis-à-vis a better photocatalyst morphology or a higher transparent conducting oxide surface area), a more valuable figure of merit for the screening measurements is the quantum conversion efficiency of the photons that are actually absorbed. To explore how this experimental construct can be developed, it is useful to first define how this efficiency is calculated.

The absorbance of a material is defined as<sup>4</sup>:

$$A = \log (I_0/ I)$$

Where  $A$  is defined as absorbance,  $I_0$  is the incident light intensity, and  $I$  is the transmitted light intensity. The light-harvesting efficiency (LHE) is related to absorbance by:

$$\text{LHE} = 1 - 10^{-A}$$

Which, with Beer's Law, can be arranged to give:

$$\text{LHE} = 1 - I/I_0$$

The absorbed photon-to-current conversion efficiency (APCE) is then related:

$$\text{APCE} = \text{IPCE} / \text{LHE}$$

$$= \text{IPCE} / (1 - I/I_0)$$

The additional data that is needed for this determination is the incident and transmitted laser intensity as the IPCE is the parameter that is normally recorded. To measure these light intensities, a standard silicon photodiode is employed as the auxiliary piece of photosensitive equipment to the screening system used throughout the previous chapters. A converging (plano-convex) lens is used to focus the rastered laser light onto the photodiode and a neutral density filter(s) is needed to prevent electrical overload. A lock-in amplifier with phase-detection input from the same function generator used to modulate the laser is used to measure the appropriate photodiode response. A schematic of the equipment is shown in Figure 6.1.

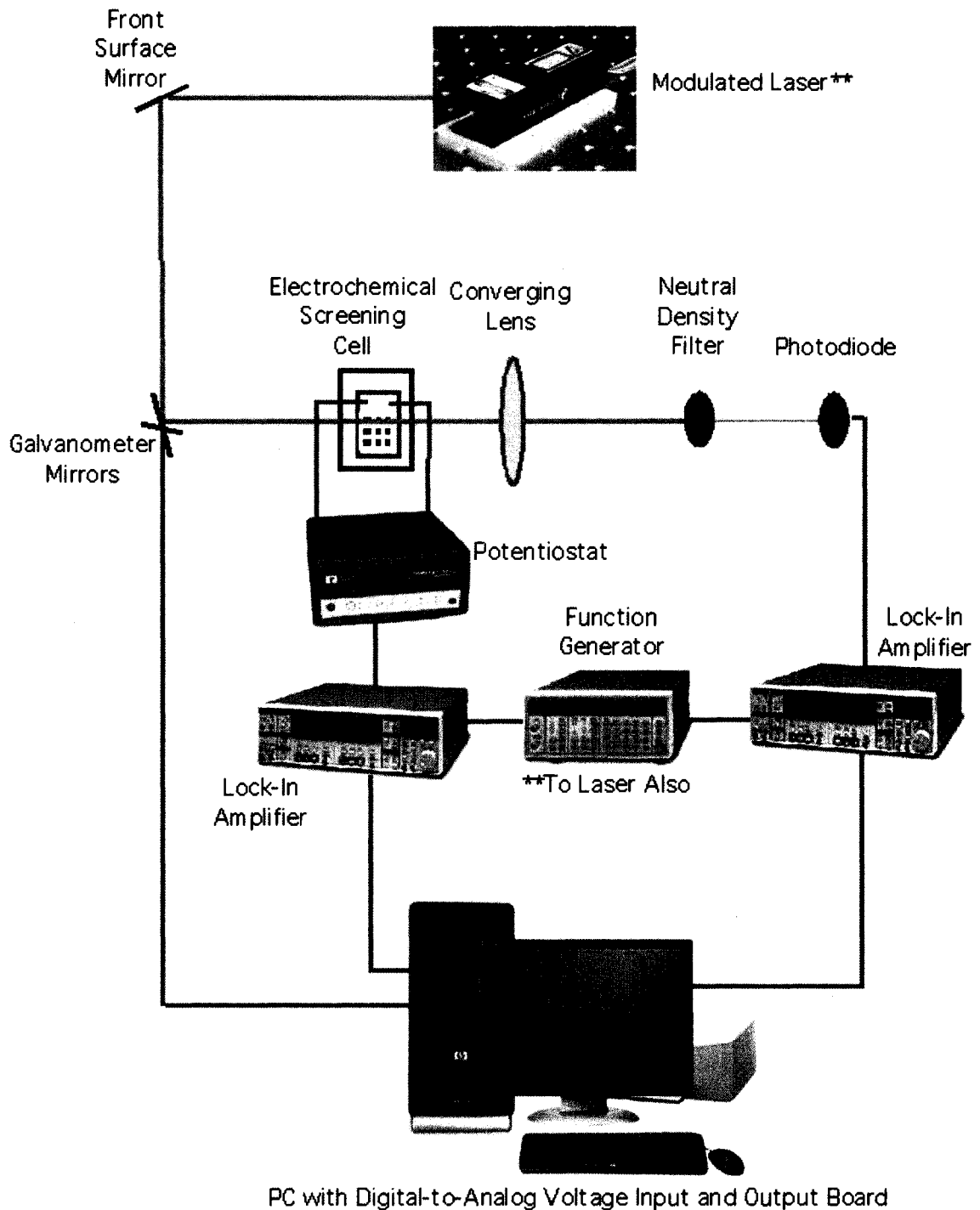


**Figure 6.1:** Schematic of the equipment used to spatially record photocurrent, incident photon-to-current conversion efficiency (IPCE), and/ or absorbed photon-to-current conversion efficiency (APCE). An auxiliary silicon photodiode connected to a lock-in amplifier is incorporated into the equipment used previously and an additional software program was written to record its output simultaneously with that of the sample being screened.

Spatial maps of the APCE are obtained by dividing the array of the LHE derived from the photodiode response into the corresponding array of the IPCE obtained for the sample. A Labview<sup>®</sup> program was written to simultaneously record the sample and photodiode signals and to create a two-dimensional array of values for each. An output directly proportional to the transmitted light intensity is obtained from the photodiode while the printed samples are scanned for IPCE. In the present configuration, slight pixel-by-pixel variations (<5%) in the incident light intensity, due to angular reflections and refractions of the laser beam by the glass sample holder, can be seen and so the program is run again with a blank substrate. The NIH funded public domain, Java based image processing program ImageJ (<http://rsb.info.nih.gov/ij>) is then used to calculate the LHE in three steps. First, if necessary, the arrays from the photodiode signal are cropped and the incident (blank) text image is divided into the transmitted (sample) text image. One is then subtracted from that resultant array and that array is multiplied by negative one. The last step is to divide the resulting array (LHE) into the IPCE array picture to obtain the spatial map of the APCE.

An informative example of the visual display of the data and some issues that have arisen during the data manipulation is shown in Figure 6.2. The upper left shows a study designed to examine the optimal thickness for the Al-Co-Fe Oxide stoichiometry as described earlier in Chapter 5. The area enclosed by the white box was chosen to

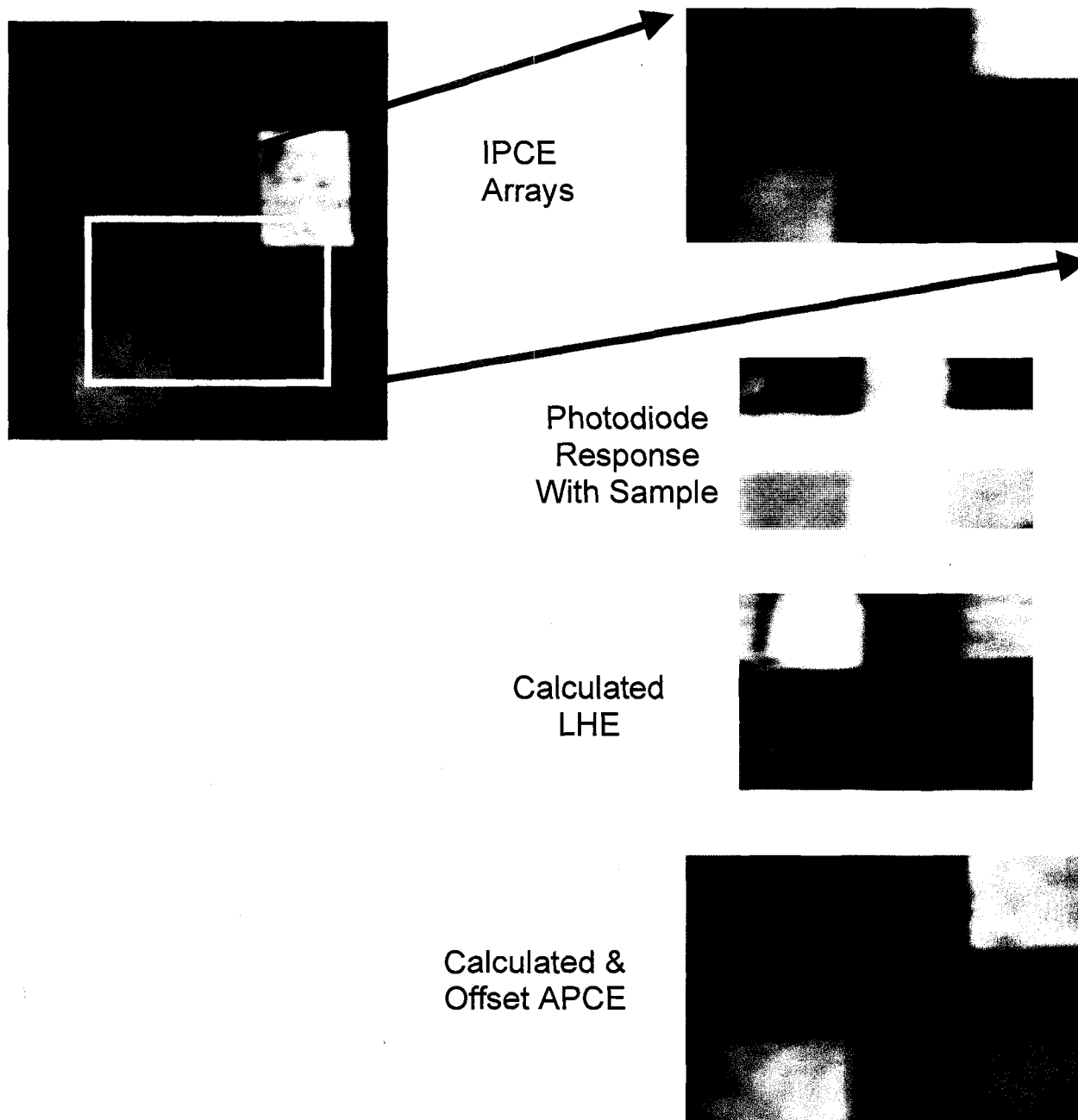


**Figure 6.2:** Example of the spatial mapping of APCE for a region of the thickness study described in Figure 5.6. The transmitted array (substrate only in the path of the laser beam) is not shown as the response is fairly even (<5% variation). Screening of the optimized Al-Co-Fe oxide stoichiometry was done with no applied bias in 0.1 M NaOH with a 32 mW 532 nm laser. See text for an interpretation of the results.

investigate how the thickness also effects the carrier collection as a function of absorption (the entire film could not be examined due to the limited size of the converging lens). As expected, the photodiode response (transmitted intensity) scales inversely with the sample thickness with the highest signal obtained where there is no printed material. The approximate average light harvesting efficiencies vary considerably for the printed regions (0.9, 0.7, 0.5, and 0.4 in order of decreasing thickness) and this has a dramatic effect on the IPCE and APCE values. Comparing the APCE of the thickest rectangle in the upper-left to that for the thinnest film in the lower right reveals that the APCE is within 10% of the IPCE for the thick film while the APCE is more than double the IPCE for the thinnest film. This is to be expected if carrier transport is limiting the carrier collection in the thicker film.

This example reveals two problems that have surfaced when this procedure is applied to printed films. First, as one would expect, there are many pixel values within the two arrays obtained from the photodiode for transmitted light where the response is essentially the same for the unprinted regions as it is for the blank substrate. This results in light harvesting efficiencies that approach zero and, in turn, creates pixel values within the APCE array that tend towards infinity (One might reason that this should not be a problem because the IPCE should also be zero at those pixels but *reflections* from the glass surfaces in our cell can hit the photoactive materials resulting in a small photocurrent, even when the direct laser beam is directed at unprinted regions). These spurious pixels create severe problems when trying to adjust the brightness and contrast

for the false-color images. There are several ways to correct this problem; by using the “remove outliers” function within the data analysis software or by offsetting the LHE a constant amount with the understanding that this affects the overall result. The offset option can be achieved by adding or subtracting a constant from the LHE array or by obtaining the blank (incident) array without the substrate in the glass sample holder (as was done to obtain the image in Figure 6.2). Although not formally correct for the entire derived array, these corrections are necessary to obtain reasonable values within the unprinted regions but still provide good images of the *relative* APCE values for the various film thicknesses.

Another problem in deriving valid conclusions relating APCE to “thickness” for printed films becomes immediately obvious when examining the films under an optical microscope. Ideally, the printed precursors would cover the substrate evenly and the decreased drop density would directly translate to “thinner” films. In reality, after annealing, a decreased thickness is indeed a probable result but there are also larger distances between segregated islands of material. And so it becomes difficult to directly comment on the precise effect of sample thickness when the areal surface coverage of the substrate can change.

While a confident determination of APCE for printed films would certainly be a desired result, the primary intention of this method was to examine the effect for samples of monodisperse nanoparticles with uniform, ideally monolayer, coverage of the substrate. This study is interesting from the perspective that the absorption coefficient

should have a strong dependence upon size in the nanometer regime<sup>5</sup>. More inspiring, there is also the possibility that multiple excitons can be created from a single photon (resulting in hypothetical conversion efficiencies in excess of 100%) if the particles are sufficiently small and the incident light is at least twice as great as the optical band gap<sup>6-8</sup>. As an entry into this exciting area of research, a postdoctoral fellow working in the group, Jianghua He, has expanded upon the initial synthesis results of Michelle Romanishan and has obtained very promising  $\alpha$ -Fe<sub>2</sub>O<sub>3</sub> nanoparticles, as shown in Figure 6.3. These particles were synthesized with an intended size of 50-nm (see scale bar). Statistical analysis performed on a sample of these nanoparticles in the TEM instrument at CSU revealed an average particle size of 55 nm with a standard deviation of only 0.5 nm, thus achieving the normal definition of “monodispersity” as the standard deviation is less than 10% of the average diameter.

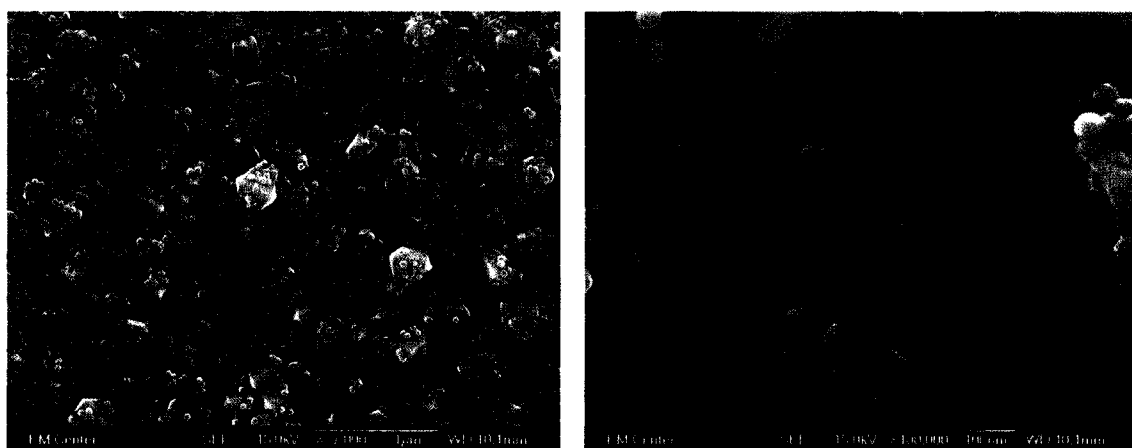
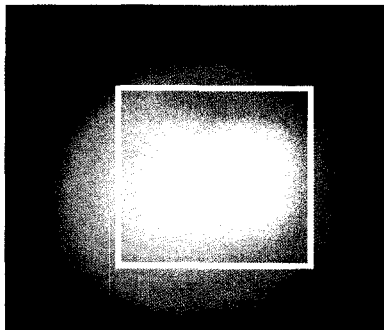


**Figure 6.3:** SEM images showing synthesized “monodisperse” 55-nm nanoparticles of  $\alpha$ -Fe<sub>2</sub>O<sub>3</sub> drop coated on FTO (courtesy of Jianghua He).

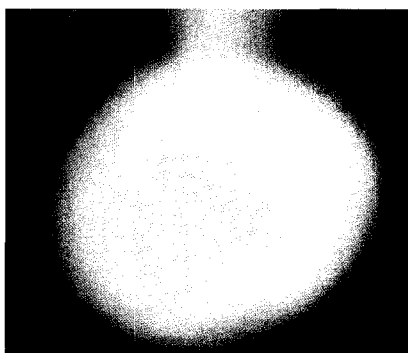
A more continuous coverage of the substrate has been a clear advantage of the deposited nanoparticle films relative to that for printed films. While the example shown was drop-cast onto FTO, films have also been deposited by spray-pyrolysis of aqueous and organic-based nanoparticle suspensions and Dr. He has been trained on that particular deposition technique. Preliminary results for the spatial mapping of APCE for the SEM sample are shown in Figure 6.4. The images were extrapolated as described earlier, with no offset correction necessary when the APCE array was obtained by cropping the larger data sets to the area outlined by the white box in the top image to prevent the problem of pixels that might approach infinity where there is no material. In this data set, the partial ring around the center displays the highest LHE value of approximately 0.7. Overall, the values obtained for the most promising regions in the center of the circle display an APCE that is more than three times of the IPCE.

The general design for this series of experiments is to prepare several monodisperse samples of varying size, deposit monolayer coverages of the substrate for each sample, and interrogate how the APCE and photoelectrochemical characteristics (current-voltage and photocurrent-wavelength) vary for each. Every procedural step in that experimental design is well within our group's capabilities, as can be seen within this thesis and the work of others in the group. However, it remains to be organized into specific parameters, executed, and collected into a complete data set.

IPCE



LHE



Cropped APCE

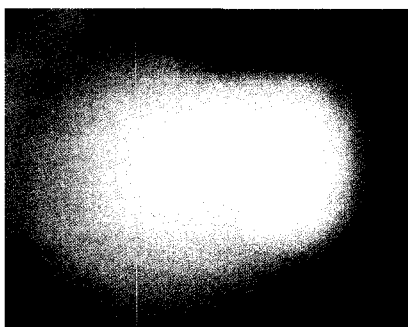


**Figure 6.4:** Example of spatial mapping of APCE for a sample of  $\alpha$ -Fe<sub>2</sub>O<sub>3</sub> nanoparticles drop-cast onto FTO. Screening was done with a 32 mW, 532 nm laser in 0.1 M NaOH with no applied bias.

## References

- (1) Duret, A.; Gratzel, M. *J. Phys. Chem. B* **2005**, *109*, 17184-17191.
- (2) Cesar, I.; Kay, A.; Martinez, J. A. G.; Gratzel, M. *J. Am. Chem. Soc.* **2006**, *128*, 4582-4583.
- (3) Kay, A.; Cesar, I.; Gratzel, M. *J. Am. Chem. Soc.* **2006**, *128*, 15714-15721.
- (4) Harris, D. C. *Quantitative Chemical Analysis*; Sixth ed.; W. H. Freeman and Company: New York, 2003.
- (5) Letherdale, C. A.; Woo, W. K.; Mikulec, F. V.; Bawendi, M. G. *J. Phys. Chem. B* **2002**, *106*.
- (6) Schaller, R. D.; Klimov, V. I. *Phys. Rev. Lett.* **2004**, *92*, 186601.
- (7) Ellingson, R. J.; Nozik, A. J.; al., e. *Nano. Lett.* **2005**, *5*, 865-871.
- (8) Nozik, A. J. *Inorg. Chem.* **2005**, *44*, 6893-6899.

## Chapter 7: Conclusions and Research Directions Needing Further Development

### Conclusions

A general route has been achieved for the high-throughput production and screening of novel and standard metal oxide photocatalysts for their ability to split water with visible light. As described in Chapter Two, the materials are first digitally fabricated with commercially-available ink-jet printers and screened for their ability to carry out the water splitting half-reactions in a custom-made system. The materials are initially printed in triangular gradient patterns that mimic a ternary phase diagram with multiple mixtures prepared on one substrate. Using this template, the constituents of promising materials can be discovered but the optimal stoichiometry is not yet known.

Promising combinations are subsequently printed using a different template consisting of arrays of squares, each with a quantifiable stoichiometry. Multiple iterations can be carried out to converge on the optimal mixture. Once this is found, larger area photoelectrodes can be prepared by a method of choice (printing, spin coating, spray pyrolysis, etc.). An Al-Co-Fe oxide with a spinel structure ( $\text{Co}_3\text{O}_4$ ), not previously known to be active for the photoelectrolysis of water, was identified and investigated in detail in Chapter Five. The physical properties, phase composition, and morphology was investigated using a variety of analytical techniques including optical SEM and XRD,

and the overall photoelectrochemical performance was evaluated with photocurrent-potential and photocurrent-wavelength measurements.

## Possible Directions for Future Research

There are *many* aspects of this project remaining to be initiated, or more thoroughly investigated, and, with sufficient funding, could continue for many years to come. As sure as I am in knowing that more work remains to be done, I am equally confident that future discoveries will be even more successful than mine.

A primary task will be to discover a more efficient material than the Al-Co-Fe oxide that was discovered and developed in this thesis. Although its measured quantum yield was more than twice that of the previously known *p*-type material, CuO, and its reproducibility made it a great material for the development of the protocols described throughout this thesis, it is not convincing that it will necessarily provide the breakthrough that is needed for efficient photoelectrolysis with metal oxides. It may, however, appear to be more attractive if a better morphology for the material is also developed in the future).

Using the procedures designed within our group provides a logical, and cost-effective, starting point for an exhaustive search for a better photoelectrolysis material. However, while the resultant methodology has proven to be quite simple (even if its *development* was not), it is not appropriate for a future graduate student thesis to be solely based on the very Edisonian processes of printing and screening. It would, however, be a great undertaking for undergraduate students and I believe that the research should be

extended to involve them at CSU and other institutions. Not only would it be mentally challenging to set up the equipment and replicate and improve upon the protocol, but it would also get students involved in solving a problem that is very important to their future. There is a very real chance that their involvement might lead to an important discovery, and I think it is helpful from the standpoint of sharing the workload of the combinatorial search.

Some very promising preliminary results have been achieved in this direction. A very bright and motivated undergraduate student, Aaron Wolfe, has assembled a robotic printing system with a Lego Mindstorms<sup>®</sup> kit using the paradigm for the Dimatix printing template. Another undergraduate student, Damian Manda, has assisted in the writing of an Excel macro to simultaneously control the TIPS printer driver. Finally, as a proof of concept that the protocol can be used in a classroom setting, four other undergraduate students have printed and screened novel materials using the kit developed by Aaron and discovered a potentially promising compound in the process (a Bi-V-Cu Oxide). With more financial support and organization, it should be an extraordinary opportunity to incorporate undergraduate “outsourcing” into the search for more promising materials, and several professors from other institutions as well as some funding agencies have expressed interest.

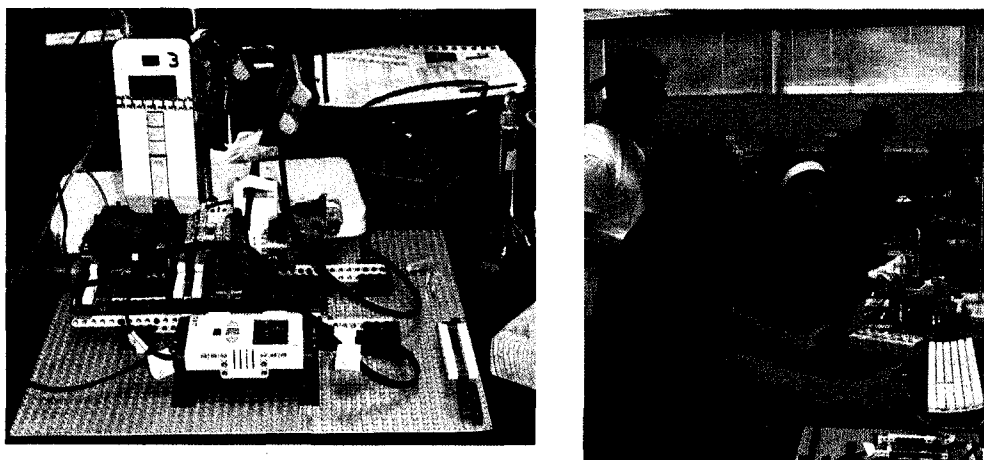


**Figure 7.1:** Pictures showing how the materials search program has been extended to undergraduate research. The picture on the left is the robotic printing system designed by undergraduate student Aaron Wolfe after learning the basic protocol and equipment used in the project. The template used for materials printing is the same as that shown in Chapter 5, with the potential for *much* lower equipment cost relative to the Dimatix printer. The picture on the right is of students working during a semester-long “Many Minds” undergraduate research class in the Spring of 2007. The students replicated the system designed by Aaron and discovered a promising photoelectrolysis material in the process.

The other, more technically challenging, ideas for future work involve a collaboration with Dr. Calvin Curtis at the National Renewable Energy Laboratory. He has an unparalleled level of experience and knowledge relevant to each of the following ideas I will discuss.

First, it may be useful to address the challenge of creating bulk, large area films that actually rival the best literature reports from the standpoint of efficiency. While this will eventually be achieved by optimizing the morphology of new materials

discovered from the combinatorial search, it is probably best to start with  $\alpha\text{-Fe}_2\text{O}_3$  **only** because the material is well characterized and so the performance of the different preparation methods can be compared. The first promising technique for creating more efficient films, with nanoparticles, is *well* underway as described in Chapter 6 and more thorough characterizations will soon follow. To the author's knowledge, that proposed direction of research outlined in Chapter 6 has not been published. The other possibility for creating a more effective material morphology is to replicate the technique of ultrasonic spray pyrolysis (USP) described in Chapter 2<sup>1-3</sup>. USP has the advantage over deposition with an airbrush in that the sonication ensures very small droplets sometimes leading to nanoparticle crystal grains. Very preliminary work has been done using a similar system at Dr. Curtis's Lab where iron oxide precursors were sprayed as well as the optimized Al-Co-Fe Oxide stoichiometry. Unfortunately, I believe the films were too thin and they were not as effective as the ones created at CSU as measured by scanning spot analysis and current-potential measurements.

There are also several different materials that should be straightforward to print with the Dimatix system or the Hewlett Packard printers depending upon the stability of the precursors in the different inkjet formulations. First, the  $\alpha\text{-Fe}_2\text{O}_3$  nanoparticles prepared by Jianghua He might be best deposited by inkjet printing and may give more continuous films than the other deposition techniques that have been tried so far. The only foreseeable problem might be the agglomeration of nanoparticles from the solution additives that may lead to clogging of the printheads.

Although it would be preferable to avoid the added materials cost, it was shown in Figure 5.9 that depositing small amounts of precious metal catalysts can greatly assist the performance of materials for photoelectrolysis. It was also discussed in Chapter 4 how redox processes within the FTO substrate occur simultaneously with the cathodic deposition of catalyst islands and that the corrosion can be exacerbated in the acidic environments necessary to dissolve the precious metal precursors. For this, and other, reasons it may be more beneficial to deposit the catalyst islands by inkjet printing. Curtis *et al*<sup>4</sup> and other groups<sup>5</sup> have printed metallic Ag, Cu, and Ni for contact lines on solar cells and thin film transistors, respectively, and at least one example, including synthesis, is well described for printing silver nanoparticles with a mean particle size as small as 6 nm<sup>6</sup>. The Mallouk group has also printed precious metal precursors<sup>7</sup>. The approach used to print these organometallic precursors could very easily be extended to other materials such as Pd, Pt, Rh, etc. and the control of drop spacing with the printer should provide a much greater uniformity and command of the areal coverage of the semiconductor by the catalyst compared to photoelectrodeposition.

Finally, a variant of the Grätzel scaffold used to create high efficiency solar cells with ruthenium-based dyes on TiO<sub>2</sub> nanoparticle substrates<sup>8,9</sup> is to use a high surface area transparent *conducting* oxide underneath the wide band gap metal oxide in a core-shell configuration<sup>10,11</sup>. To a first approximation, this variation on the theme will be necessary for an effective photoelectrolysis system. Using the paradigm of increased surface area for light absorption, penetration of the mesoporous layer with electrolyte, etc. makes as

much sense for a photoelectrolysis system as it does for a dye-sensitized solar cell, but there is absolutely no reason to assume that the same special kinetic advantages enjoyed by an organometallic ruthenium dye bound to TiO<sub>2</sub> (e. g. rapid photoexcited exciton separation, slow recombination of injected electrons with the electrolyte, etc.), and favorable band alignments, would also be present for a semiconductor photocatalyst covering TiO<sub>2</sub> in aqueous solution. Instead, a thin photocatalyst film draped over a nanoparticulate transparent conducting oxide core-shell system is a much more probable architecture and should be thoroughly investigated as a possible means to improve the efficiency.

While many reports exist for the creation of readily dispersable nanoparticulate tin oxide conductive solutions<sup>12-14</sup>, it may be more fruitful to try printing, or fabricate by other methods, another material that would (hopefully) be a more robust substrate for *p*-type semiconducting materials that are active at negative potentials. Specifically, transparent conducting zinc oxides may be excellent candidates since they lack the redox chemistry of tin and indium systems. A general synthesis method of these metal oxide nanoparticles has been presented<sup>15</sup> and there is at least one account of printing that material in continuous lines for thin-film electronics by an industrial collaborator, Dr. Greg Herman<sup>16</sup>.

Regardless of specific future direction of the group, the search for a cost-effective means to produce hydrogen from water and sunlight will continue throughout the world because of the potentially huge economic and environmental impact. I would like to end my thesis by saying that I am proud to have been involved in the development of a method that I believe has so much potential to help solve this very important problem.

## References

- (1) Duret, A.; Gratzel, M. *J. Phys. Chem. B* **2005**, *109*, 17184-17191.
- (2) Cesar, I.; Kay, A.; Martinez, J. A. G.; Gratzel, M. *J. Am. Chem. Soc.* **2006**, *128*, 4582-4583.
- (3) Kay, A.; Cesar, I.; Gratzel, M. *J. Am. Chem. Soc.* **2006**, *128*, 15714-15721.
- (4) Curtis, C. J.; Kaydanova, T.; Hest, M. F. v.; Miedaner, A.; Garnett, E.; Ginley, D. S. In *Digital Fabrication*; Stasiak, J., Ed.; The Society for Imaging Science and Technology: Baltimore, MD, 2005, p 160-163.
- (5) Wu, Y.; Li, Y.; Ong, B. S. *J. Am. Chem. Soc.* **2007**, *129*, 1862-1863.
- (6) Wu, Y.; Li, Y.; Ong, B. S. *J. Am. Chem. Soc.* **2006**, *128*, 4202-4203.
- (7) Reddington, E.; Sapienza, A.; Gurau, B.; Viswanathan, R.; Sarangapeni, S.; Smotkin, E. S.; Mallouk, T. E. *Science* **1998**, *280*, 1735.
- (8) Nazeeruddin, M. K.; Kay, A.; Rodicio, I.; Humphry-Baker, R.; Muller, E.; Liska, P.; Vlachopoulos, N.; Gratzel, M. *J. Am. Chem. Soc.* **1993**, *115*, 6382-6390.
- (9) Regan, B. O.; Gratzel, M. *Nature* **1991**, *353*, 737.
- (10) Chappel, S.; Grinis, L.; Ofir, A.; Zaban, A. *J. Phys. Chem. B* **2005**, *109*, 1643-1647.
- (11) Chappel, S.; Chen, S.-G.; Zaban, A. *Langmuir* **2002**, *18*, 3336-3342.
- (12) Burgard, D.; Goebbert, C.; Nass, R. *J. Sol-Gel Sci. Tech.* **1998**, *13*, 789-792.
- (13) Kim, K. Y.; Park, S. B. *Mat. Chem. Phys.* **2004**, *86*, 210-221.
- (14) Ederth, J.; Heszler, P.; Hultaker, A.; Niklasson, G. A.; Granqvist, C. G. *Thin Solid Films* **2003**, *445*, 199-206.
- (15) Pinna, N.; Garnweitner, G.; Antonietti, M.; Niederberger, M. *J. Am. Chem. Soc.* **2005**, *127*, 5608-5612.
- (16) Lee, D.-H.; Chang, Y.-J.; Herman, G. S.; Chang, C.-H. *Adv. Mater.* **2007**, *19*, 843-847.

# **Appendix A: Independent Research Proposal Optimization of the Charge Transfer Kinetics For A Quantum-Confined Photoelectrode Material**

## **Abstract**

The flurry of interest and hope for quantum-sized structures to solve age-old problems is compelling. But fundamental to many of the potential applications of these novel materials is the necessity of effective charge transfer to and from the system. An opportunity exists to apply the fundamental principle of charge transfer, Marcus Theory, to systems composed of quantum dots. Specifically, it is proposed to examine more comprehensively how the photoexcited charge transfer kinetics can be optimized with respect to a system's free-energy difference and reorganization energy, as evidenced by the presence of an "inverted region" if the system follows the classical model.

To examine this question, or to possibly elucidate a phenomenon that is presently unknown, we would like to first construct photoelectrodes made by electrodepositing CdSe quantum dots onto Au (111) surfaces, with and without an electrical insulating layer, and onto nanocrystalline-TiO<sub>2</sub> surfaces in order to interrogate the excited charge carrier dynamics of these systems. The material that will be studied, CdSe, is a very promising next-generation photovoltaic material as it is a photoelectrochemically efficient material that can be fabricated from inexpensive precursors and techniques- which makes further study of this system even more compelling for its potential to become a commercially viable device.

## A.2 Background and Significance

Although the demonstrated and potential applications of quantum confined materials are almost too numerous to mention, they have already shown promise as biological sensors<sup>1</sup>, LED's<sup>2</sup>, wavelength-tunable lasers<sup>3</sup>, and solar cells<sup>4,5</sup>. Of particular interest to photovoltaic energy conversion is that, while single band gap semiconductors have a Shockley-Queisser calculated maximum theoretical thermodynamic efficiency limit of 32%, quantum dot solar cells have a theoretical efficiency limit that approaches 66%<sup>6</sup>. There are several factors that can contribute to their higher efficiencies relative to bulk materials including the augmented surface area of nanostructures<sup>7</sup>, the potential to vary the band gaps of the materials for optimal solar spectrum collection via precise control of the size of the nanostructures<sup>8</sup>, and the longer excited state lifetimes that result when carriers are confined to regions of space that are small compared to their deBroglie wavelength or excitonic Bohr radius<sup>6</sup>. The longer excited state lifetimes lead to the unique phenomenon of "carrier multiplication" known to occur within quantum confined structures; energy in excess of the bandgap is dissipated as heat as one incident photon produces only one charge carrier in bulk-sized materials, but *multiple* charge carriers having potential energy greater than or equal to the band gap can be created from a *single* absorbed photon by the inverse Auger process of impact ionization when the light absorber is less than ca. 10-nm in one dimension<sup>9-12</sup>. Any one of these possibilities hints that a more exhaustive study of excited state charge transfer for these systems may be a very profitable endeavor.

Marcus Theory has evolved over the past fifty years to become the standard approach to examine the mechanism of charge transfer as applied to a wide variety of applications<sup>13-15</sup>. The theory is based upon consideration of the Frank-Condon factors affecting the free energy surfaces of the reactants and products, as well as solvational effects. Although more extensive discussions of the theory can be found elsewhere<sup>14-16</sup>, we will *very* briefly summarize a few of the basic relevant premises below.

Charge transfer rate constants can be correlated with the Arrhenius description,  $k = A\exp(-\Delta G^*/kT)$ , when the total activation barrier,  $\Delta G^*$ , includes the electron transfer event,  $\Delta G^\circ$ , as well the effects of the reorganization energy,  $\lambda$ , which incorporates outer-sphere and inner-sphere solvation and vibration effects<sup>17</sup>:

$$\Delta G^* = \frac{\lambda}{4} \left( 1 + \frac{\Delta G^\circ}{\lambda} \right)^2$$

A few of the qualitative results of the model can be simply and readily explained with the following picture:

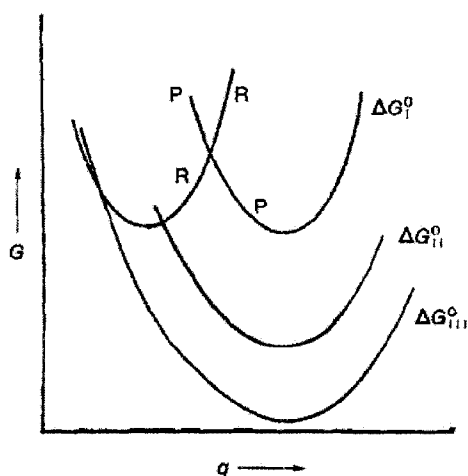


**Figure 1:** Plots of the free energy,  $G$ , versus reaction coordinate,  $q$ , for reactants ( $R$ ) and products ( $P$ ), for three different values of  $\Delta G^\circ$ .  $\Delta G_1^\circ$  is the point at which the forward and reverse charge transfer rates are equal.  $\Delta G_{11}^\circ$  is near the point of maximal exoergicity where the smallest activation barrier translates to the fastest forward electron transfer rate.  $\Delta G_{111}^\circ$  is an example of a free-energy difference producing an "inverted effect"<sup>16</sup>.

A particularly interesting novelty of this picture is the prediction of an “inverted region”, whereby for all points having a free energy difference *greater* than the point of maximal exergonicity (when the trough of the reactant’s curve is intersected by the product’s curve), the activation barrier gets larger and the charge transfer rate is actually expected to *decrease* even though the free-energy difference is *increased*. The prediction of this point of diminishing returns implies that there is an optimal free-energy difference between the Fermi level of an electrode and the redox potential of the solution. The equations given above also lead to the expectation that the logarithm of the electron transfer rate constant versus  $(1 + \Delta G^0)^2 / 4\lambda k_B T$  should be linear with a slope of -1. To this author’s knowledge, the most recent verification of this relationship was a rigorous study on a bulk ZnO electrode carried out by Lewis, et. al.<sup>14,15</sup>.

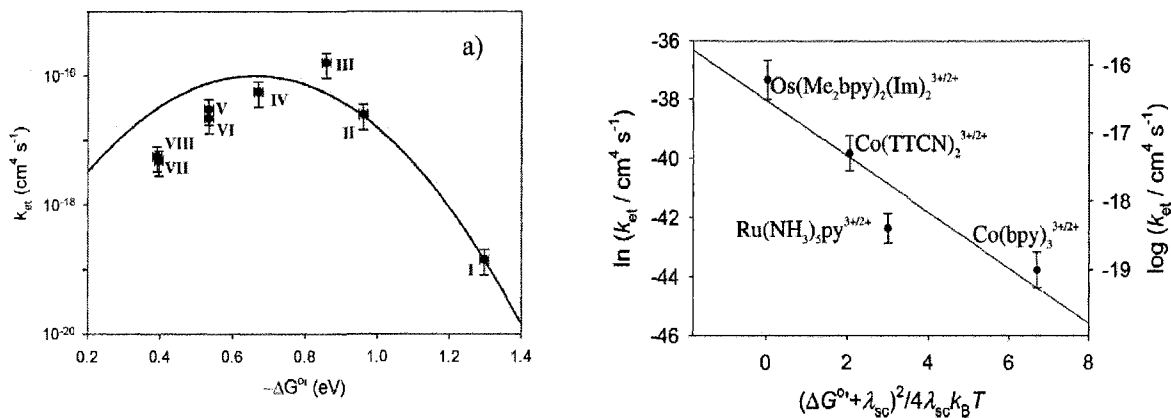


**Figure 2:** Recent Experimental Observations displaying the expected dependence of single electron transfer rate constant on free energy difference (left figure<sup>14</sup>) and reorganization energy (right figure<sup>15</sup>).

Although the Marcus model has become the dominant single charge transfer dogma, it would be fascinating to see if the tenets of the model are broad enough to encompass quantum-confined systems. The most fascinating hype of quantum-sized systems is that they display disparate physical qualities relative to bulk materials. This begs the question: are there quantum effects to charge transfer? It is already known that, for bulk materials, the high density of electronic and vibration/ rotation states leads to fast nonradiative relaxation rates. In quantum dots, however, the situation is quite different as the energy spacing within electronic energy levels exceeds phonon energies by at least an order of magnitude<sup>8</sup>. This leads to a limited relaxation rate, commonly called the “phonon bottleneck”, which should make charge transfer more competitive relative to recombination. It may also be possible to observe discretized effects that would not be expected for bulk materials. We would like to contribute to the body of knowledge that will spur on developing theories, experiments, and models of quantum dot systems based upon charge transfer. For the sake of future applications of benefit to society, we would like to optimize the charge transfer kinetics for two prototypical quantum dot photoelectrode systems- one involving a flat electrode and another representative of a nanocrystalline assembly.

## A.3 Original Research Design, Methods, and Analysis

### A.3.1: Construction of Flat Quantum Dot Photoelectrodes

Although it may be more useful to someday deposit CdSe nanocrystals onto conductive glass substrates such as fluorine-doped tin oxide<sup>18,19</sup> for the goal of commercial viability, more thorough characterization and control of the material structural quality has been carried out on dots electrochemically deposited onto Au (111) surfaces<sup>20-23</sup> which have been produced by evaporation of the gold onto glass or mica substrates. In this method, the first layer is epitaxial with the gold substrate (less than 0.6% lattice mismatch) and, as growth proceeds, the crystals are subjected to increasing mismatch strain and the growth eventually terminates. Nanocrystals are thus produced that are typically around 4 nm in diameter with a narrow size distribution. The as produced films are composed of the direct bandgap wurtzite phase of CdSe<sup>24,25</sup>. Precise control over the shape, thickness, aspect ratio, morphology and crystallinity can be achieved by establishing the relationship between these quantities and the cathodic current density<sup>18,25</sup>.

Paramount to the success of this system is the ability of a thin film of CdSe quantum dots on gold to preferentially transfer *one* of the photoexcited charges (the hole in this case) to the electrolyte and to separate it from the counter charge carrier, which must diffuse to the Au substrate. Charge separation in this manner must compete with electron-hole recombination at the Au substrate and within the QD itself. This ability to function as a liquid junction photoelectrode has been demonstrated when the thickness of the deposited CdSe is such that the grain boundaries between layers augment the barrier for charge recombination at the gold substrate, but is not so thick as to cause

recombination within the quantum dot<sup>20</sup>. Thus, although it is perhaps counterintuitive, a limited number of grain boundaries actually *improve* the photocurrent collection for this particular system in contrast to the usual situation for bulk and other nanocrystalline solar cells. This optimal thickness can be consistently produced by carefully monitoring the amount of charge passed during the deposition.

Unfortunately, the as-prepared films mentioned above are not expected to be continuous and less than 50% coverage of the gold is predicted. This limits the usefulness of this system to electrolytes that are not redox active with gold. As the present accounts of those electrodes do not include a diverse group of redox couples, it may be necessary to form an electrically blocking layer over the gold substrate without taking away the system's ability to function as a photoelectrode. There are several routes to pursue in order to accomplish that end. In one route, a self-assembled monolayer (SAM) of CdSe QD's capped with thiol ligands can be anchored onto the gold substrates. Under such a configuration, the charge transfer tunneling rates should depend exponentially upon the tunneling distance (i.e. the size of ligand)<sup>26,27</sup>. Alternatively, CdSe nanoparticles on gold can be prepared by the use of molecular templates<sup>28</sup>. In this approach, a well-ordered SAM is first deposited by dipping the gold substrate into a thiolated  $\beta$ -cyclodextrin solution. Cavities within this template SAM are then filled with QDs by a two-step process: reduced selenium ( $\text{Se}^0$ ) is deposited by the reduction of  $\text{HSeO}_3^-$  ions and then this Au/ $\beta$ -cyclodextrin/ $\text{Se}^0$  film is transferred to a selenium-free solution dosed with  $\text{Cd}^{2+}$  ions where the selenium layer is cathodically stripped to generate  $\text{Se}^{2-}$  which goes on to form CdSe films *in situ*<sup>29</sup>. The ability of both of these described systems to function as photoelectrochemical cells has been well demonstrated

with the additional benefits of a much more continuous coverage over the entire gold surface and the formation of an electrically-blocking layer onto any exposed areas of the gold substrate<sup>26,28,30</sup>. As with the bare electrodeposited films, an extensive examination of electrolyte optimization has not been carried out on these systems and the electrolytes involved to date have frequently included the use of hole scavengers, which essentially act as “sacrificial reagents”.

The contribution of surface states to the mechanism(s) of charge transfer within these system will ultimately need to be quantified in order to establish the legitimacy of this study within the context of traditional Marcus Theory. Notably, it is extremely important that the effect of defect densities at the semiconductor/ liquid interface be mitigated<sup>14</sup>. Simple inorganic methods<sup>31</sup>, or the use of ligands such as thiolates<sup>32,33</sup>, have already been demonstrated to passivate the surface atoms of CdSe quantum structures and their effectiveness has been analyzed from luminescence quenching<sup>34,35</sup> or conductive tip AFM experiments<sup>21,36</sup>. Following passivation, emission from trapped carrier recombination has shown to be substantially quenched while the conductive tip AFM work has revealed only direct band-to-band absorption. To put our system within the same framework, collaboration with the groups cited above would be invaluable.

Finally, it should also be mentioned that, based upon the magnitude of current that can be expected, that the rate of mass transfer to the electrode is not at all expected to limit the performance for this system<sup>37,38</sup>. This can and will be verified by replacing the quantum dot photoelectrode as the working electrode with a metallic electrode such as Pt, which *will* be mass-transport limited, and comparing their current-potential characteristics<sup>39</sup>.

### **A.3.2: Construction of a Quantum-Dot-Sensitized Nanocrystalline Scaffold**

Draping a layer of quantum dots over a high surface area nanocrystalline  $\text{TiO}_2$  film has numerous simultaneous advantages and offers a logical entry into the practical implementation of these materials. In analogy to the sensitization of  $\text{TiO}_2$  with organometallic dyes, the conduction band offset between CdSe quantum dots and  $\text{TiO}_2$  allows for rapid charge separation from the photoexcited sensitizer into the conduction band of  $\text{TiO}_2$ <sup>40</sup> and the metal oxide underlayer has been shown to increase the photostability of CdSe<sup>40,41</sup>. This configuration is also known to retain the oft-cited advantages of increased quantum efficiency resulting from an increased optical cross-section relative to flat electrodes, a porous structure that allows penetration of the electrolyte, and effective electron transport to the conductive substrate that are usually recognized in dye-sensitized solar cells<sup>7,42</sup>. In addition, quantum dot sensitization also offers the advantage that, just as in the flat electrodes, the band gap of the sensitizer can be tuned to match the spectral distribution of sunlight by size control and the oscillator strength (which is directly proportional to the absorption coefficient) is known to increase as the particle size decreases due to strong overlapping wave functions of confined charge carriers<sup>43,44</sup>. Efforts to deploy CdSe on a nanocrystalline scaffold have already produced success worthy of note; incident photon-to-electron conversion efficiencies (IPCE's) of between 10 to 20% at 500 nm appear to be reproducible<sup>40,45,46</sup>. We hope to further increase the efficiency of these films by examining the choice of charge relay from the counter electrode.

We propose to deposit optically transparent layers of nanocrystalline titanium dioxide onto conductive glass substrates using the well-established alkoxide partial-hydrolysis technique<sup>47</sup>. Using prior results obtained for a CdSe on TiO<sub>2</sub> system<sup>45</sup> we will manipulate the synthesis conditions with the aim of producing TiO<sub>2</sub> particle sizes of around 25-nm with a thickness around 3.5- $\mu$ m as this has been shown to possess the best carrier transport properties. The CdSe QD's will be prepared using the same chemical solution deposition technique and precursors used above with the expectation that, depending upon the amount of cathodic charge that is passed, QD's from 2 - 6 nm in diameter will be formed on top of the TiO<sub>2</sub><sup>45,48</sup>. With the experience gained from the experiments on flat electrodes, we will then interrogate the photoelectrochemical behaviour of this system.

Finally, in order to investigate a phenomenon that has, to this author's knowledge, only been reported for flat electrodes, we will examine if the system displays a multiple exciton generation effect. As the threshold for multiple carrier generation by optical excitation is twice the band gap of the nanocrystalline light absorber<sup>10,12</sup>, we can still access that photon energy with our designated light source. The existence of this effect can be revealed by quantum yields greater than 100% after a particular wavelength is reached in a photoaction spectrum.

### A.3.3 Analysis of the Photoelectrodes (Original Design)

The flat-band potential of the photoelectrodes must first be determined in order to establish the relative energetics between the band edges and the redox couples and to ensure that the electrode is protected against the possibility of corrosion that would be expected if the redox potential were outside of the material's band gap. Unfortunately, this cannot be determined *in situ* by the conventional Mott-Schottky method, as the typical height of these nanostructures (~10 nm) is less than the expected depletion region required for an impedance measurement. However, that same shortcoming also becomes the solution in translating the flatband determination by photoemission<sup>49</sup> to that in solution as near flatband conditions can be assumed because, even with band bending, field effects would be negligible due to the thin width of the quantum well<sup>50,51</sup>.

With the band edge positions established, we will choose two homologous series of nonadsorbing outer sphere redox couples that span the band gap of our photoelectrode in a methanol<sup>38</sup> or acetonitrile<sup>52</sup> solvent. To probe the existence of an inverted region, the first series of redox couples will have similar reorganization energies but different formal redox potentials. The second series of experiments will have a series of redox couples that have similar formal reduction potentials yet have different reorganization energies. By precedent, metallocenes and their associated cations are believed to fulfill this need<sup>17,52,53</sup>. A series of bipyridinium viologen couples<sup>38,39</sup> can also fulfill these requirements. The reorganization energies of the charge transfer complexes can be determined from NMR experiments<sup>14</sup> and from curve-fitting the rate constant as a function of free-energy plots<sup>39</sup>. For the sake of electrode stability and avoiding other

spurious redox processes, we will carry out our photoelectrochemistry experiments inside an atmosphere-controlled glovebox.

The experimental property of interest is the current generated as a function of the wavelength of light that is incident upon the sample. The photocurrent signal under monochromatic radiation can be isolated from dark current by passing the beam from a xenon arc lamp through a monochromator and modulating the beam at a chosen frequency to be measured by a lock-in amplifier. From this, the band gap of the material will be determined *in situ* in a three electrode quartz cell by using the sample as a photoelectrode in a liquid junction<sup>20</sup>.

With the ability to measure a photocurrent in place, there exists a relatively simple method to equate an observable quantity to the electron transfer rate constant. If the metallic underlayer has been blocked, and if the surface of the light-absorbing semiconductor has been completely passivated, only electrons that have been promoted to the conduction band need to be considered for charge transfer to the electrolyte. With these conditions in place, the charge transfer process should be a bimolecular reaction, which is first order with respect to the concentration of ions in solution and in the surface concentration of electrons. The relationship between the current density,  $J(E)$ , the concentration of the charge acceptor species in solution,  $A$ , and the charge transfer rate constant is given by<sup>38,54</sup>:

$$J(E) = -qk_{et}n_s[A]$$

The population of surface electrons,  $n_s$ , follows a Boltzmann relationship described by<sup>17</sup>:

$$n_s = n_b \exp(-q(V_{bi} + V)/kT)$$

where  $n_b$  is the number of electrons within the bulk, a constant that can be determined from a measurement of the sample resistivity and the mobility of carriers in the solid<sup>37,38,55</sup>,  $V_{bi}$  is the equilibrium voltage drop across the semiconductor that is established with the redox couple, and  $V$  is the applied potential. Unlike electron transfer across a metal/ liquid interface, the surface electron concentration,  $n_s$ , is affected by the potential that is applied to the electrode but the electron transfer rate constant is not<sup>37,38</sup>. Thus, it is not explicitly necessary to calculate the surface and bulk concentration of electrons, nor the built in voltage, as the values will remain constant at all applied potentials. It is, however, a necessary control to establish a linear dependence of  $\ln J$  versus  $V$  with a slope near 59-mV per decade of current density as well as a linear relationship between the current density and concentration of acceptor species in solution<sup>39</sup>. With these controls in place, we can assert that it is only the driving force of reaction, that is, the difference between the conduction band edge of the quantum dot and formal reduction potential of the redox couple, that affects the charge transfer rate constant. From there, the systems can be optimized with respect to the best possible outer-sphere redox couple.

### A.3.4 Revised Research Design, Methods, and Analysis

We will purchase the “lumidot” CdSe and CdS QD kits from Sigma Aldrich. This kit contains six colloidal, monodispersed (<5% standard deviation in size) solutions of quantum dots with excellent quantum-confined optical properties. For CdSe in particular, the quantum dots range in size from 1.6 - 7.7 nm with corresponding emission peaks between 370 and 650 nm and so we can interrogate a large portion of absorption wavelengths within the visible spectrum. All of these dots are also reported to have the same quantum yield. Using these dots, the TiO<sub>2</sub> will be sensitized following procedures outlined in a multitude of papers- some of which were referenced in the original proposal.

The basic steps are as follows:

1. Exchange the TOPO-capped QD's with a thiol and carboxylate linker molecule (mercaptopyrionic acid) by adding it dropwise to a 50/50 THF/ EtOH solution with the TOPO-capped QDs.
2. Prepare a TiO<sub>2</sub> colloid by hydrolyzing titanium isopropoxide in a glacial acetic acid solution followed by autoclaving the suspension at 497 K for 12 h.
3. Sonicate the TiO<sub>2</sub> and apply it to an FTO film via the doctor blading technique.
4. Anneal these electrodes at 673 K and immerse them into the solution, once they have safely cooled, for approximately four hours.
5. Do the photoelectrochemical experiments after washing with acetonitrile and toluene.

We will then obtain (or synthesize if necessary) a homologous series of outer-sphere one-electron redox couples that have formal potentials spanning the band gap of the QD. To cite an example, a homologous series of Ru-coordination compounds shown by an earlier publication matches these desired characteristics<sup>56</sup>. There are certainly other compounds we could use as well, but we will also try a Na<sub>2</sub>S/ polysulfide redox couple because that has been used in a lot of papers about CdSe quantum dots and so using it as well will help to serve as a reference point for results to be compared to those papers. In order to establish the formal redox potentials for the compounds, we will simply use the

cyclic voltammetry peak potentials obtained using a Pt wire or glassy carbon working electrode in conjunction with a Pt gauze counter electrode and an SSCE or Ag/AgCl reference electrode. A supporting electrolyte (e. g. 1-M activity  $\text{LiClO}_4$ ) will also be employed and the same solution recipe (including purging with Ar or  $\text{N}_2$ ) will be used as in the subsequent experiments involving QD's.

CdSe quantum dots are electrochromic and, therefore, the bandedge positions can estimate by monitoring the IR and/ or visible absorbance as a function of applied potential within a 3-electrode spectroelectrochemical cell<sup>3</sup>. We will study absorption transitions *within* the excited state (1S to 1P) with a mid-IR probe while applying progressively more energetic potentials in order to extrapolate the most telling results for the conduction band edge. When the energy of the electrons supplied by the potentiostat is sufficiently high (by sweeping progressively more negative), electrons are eventually injected into the conduction band of the quantum dot and the absorption begins.

We will obtain an H-NMR spectrum for each redox species.

We will do steady-state photocurrent spectroscopy, in order to get a broad picture of what's going on and to determine the most overall efficient architecture in terms of power conversion efficiencies, which will include dark and illuminated cyclic voltammetry as well as obtaining the action spectrum. We will use a computer-controlled potentiostat for the CV's and a custom-made system for the action spectrum (the Parkinson lab has such equipment). We will immerse the photoelectrodes in a three-armed cell, with a Pt-gauze counter-electrode and an SSCE reference electrode, filled with a toluene solution containing a supporting electrolyte. We will do this for a total of 30 systems:

1. 24 systems with variable redox potentials but containing a consistent QD size (that's 6 sizes to work with from the kits and 4 redox couples to try for each one).
2. 6 systems with one redox couple but different QD sizes. We'll use the results from step 1 to estimate the best redox couple in terms of power conversion efficiencies.

We will purchase a Clark-MXR 2010 laser system and an optical detection system provided by Ultrafast Systems (Helios) for our transient absorption studies as well as an SLM-S 8000 spectrofluorimeter to record our emission spectra. As an initial probe of charge transfer processes to a redox mediator it is useful to look at the emission profiles with and without the reduced form of the mediator as well as with and without TiO<sub>2</sub>. We will also look at the absorbance and the change in absorbance as a function of wavelength following laser pulse excitation for each system mentioned above in order to derive the best wavelength to probe transient CdSe bleaching (each QD size will need to be probed at its own characteristic wavelength). We will obtain traces of  $\Delta A$  vs. time (ps scale) for each redox couple using a fixed QD size and for all of the different sizes of CdSe-on-TiO<sub>2</sub> with and without the redox couple as well as  $\Delta A$  vs. time (ps scale) for pure CdSe solutions (after the appropriate ligand exchange).

We will use UV light that has photons more than twice the energy of the band gap of the pure QD to do photocurrent-voltage curves (dark curves too). We will illuminate pure TiO<sub>2</sub> and compare this to an illuminated sample of a QD sensitized TiO<sub>2</sub> system (this is to look for the possibility of multiexciton generation measured as photocurrent).

## A.5 Discussion of Possible Results (Revised Design)

If the charge transfer process of interest is the rate-limiting step, then the estimation of the charge-transfer rates of interest can come from the relative amount of current collected (steady-state determinations) after altering the controlled variables of choice. However, it is also possible that other factors may contribute to the overall observed behavior and we wish to look at several variables and so rigorous piecemeal kinetic studies will also have to be done. So Let's get into some of those possibilities and how the results might play out.

First, we were going to determine the relative band-edge or redox positions, on the vacuum scale, for the  $\text{TiO}_2$ , the QD, and the redox mediators. Fortunately, we have literature values for each of these but we should check that we're on the right track with the cyclic voltammetry and electrochromic experimental setup described above. The band edge position can be estimated as the sharp change in absorbance after electron injection through  $\text{TiO}_2$  into the QD at a known potential. We will expect the 7.0-nm CdSe QD on nanoparticle  $\text{TiO}_2$  composite system to have a conduction band edge of about -0.8-V vs. NHE (valence band edge of +1.2-V vs. NHE). Of course, the band edge positions have been historically observed to shift with decreasing particle size and this will be our expectation to look for- we should expect expect a more negative shift in the conduction band edge of about 0.85-V when comparing the largest to smallest QDs. The mediator coordination compounds should be within these band. The driving force will then be defined as  $-nFE$  where  $E = E^0_{\text{mediator}} - \text{QD}_{\text{VB edge}}$  or  $E = \text{QD}_{\text{CB edge}} - \text{TiO}_{2\text{CB edge}}$ .

We will fit the transient absorption spectra using a biexponential decay kinetics model provided in the literature and define the charge transfer rate from the reduced form of the mediator to the QD as follows:

$$k_{ht} = 1/\tau_{\text{mediator}} - 1/\tau_{\text{NOmediator}}$$

These experiments will also give us an idea of how significant the back electron transfer from the TiO<sub>2</sub> to the oxidized form of the QD is. Laser pulse excitation of the QD in a composite photoelectrode results in immediate electron injection into TiO<sub>2</sub>. Without the reduced form of the mediator, the only option for the injected electrons is to recombine with the oxidized QD. Conversely, with the reduced form of the mediator present, the oxidized QD can be regenerated by the injected electron recombination *or* by the electron donor in solution. If the recombination is *not* significant, the change in absorption decay is faster with the reduced form of the mediator present as the QD is rapidly regenerated by the desired mechanism. If the regeneration is really slow, we will not be able to differentiate between the mediator/ no mediator data and so back electron transfer from the TiO<sub>2</sub> back to the oxidized QD is significant.

A more complicated scenario can arise wherein the mediator has HOMO-LUMO excitation which may interfere with its role as a hole scavenger in the ground state- a possibility that has been probed for the Ru-coordination compounds we will use. In that case, an electron can be injected into the CB of the QD- the same net result as if a photoexcited QD had transferred a hole to the mediator. To differentiate between the two mechanisms, it is useful to look at the transient absorption and photoluminescence decay on the same time scale. In CdSe QD's absorption changes provide information about the depopulation rate of electrons while the photoluminescence intensity is determined by the

product of electron and hole population numbers<sup>56</sup>. This means that an investigation of photoluminescence relaxation is a study of hole dynamics if the process occurs faster than electron transfer- a fortunate reality for CdSe QD's.

To investigate these competing mechanisms, one should examine the transient absorption and photoluminescence decay with and without the redox couple. IF the desired process is occurring, a hole will be transferred between the QD and the mediator. As luminescence is the product of *both* electron and hole populations, this is verified experimentally by the observation of an increased rate of photoluminescence decay when the mediator is present while the transient absorption traces remain relatively constant.

It will be necessary to estimate reorganization energies for each of the redox couples, as this will be necessary in curve-fitting the data to a Marcus model. One of the means by which a scientist can estimate reorganization energies is with solution-based NMR OR from curve-fitting plots of the electron transfer rate constant as a function of driving force as Lewis et al have done in experiments relating Marcus theory to semiconductor/ liquid junctions using Si and ZnO<sup>14,15,17,38,39</sup>. In a nutshell, for the NMR approach, one can determine the reorganization energies from a nonlinear least-squares fit of a selected proton peak within a simple NMR spectrum of the species in solution and an equation described in the references. The measurable information of interest in the "nonlinear least-squares fit" is the particular proton peak position and width. The purpose of the NMR-derived reorganization energies will be to see how it compares to the values derived from curve-fitting.

Once we are confident that we have established the relative energetics, the pieces of the kinetics puzzle, and the reorganization energies for the players in the photoelectrode system, we can begin to think about Marcus theory. In principle, the charge transfer kinetics (vis-à-vis current density if the desirable processes are occurring more rapidly than the undesirable ones) depends upon the interfacial free energy difference and reorganization energy such that the rate increases as the reorganization energy decreases and the driving force increases up to a point. After that point, the so-called “inverted region”, the charge transfer kinetics actually *decreases* with increasing driving force. So, IF this system follows the Marcus formalism, IF we have provided a large enough variability in the driving force, and IF the higher driving force doesn't also translate to a significant increase in the rate of undesirable recombinations, then the charge transfer kinetics should increase as the difference between the formal redox potential and QD valence band flatband potential increases until the difference is large enough that the trend reverses. From a curve fitting with the assumption that the logarithm of the electron transfer rate constant is a quadratic with respect to  $-\Delta G$ , one could then obtain the redox potential for optimal charge transfer kinetics for this system and that would potentially help to arrive at a possible device architecture to achieve the maximum power that could be obtained from these types of systems. It is also entirely possible that we won't find any Marcus relationship but we will stumble across a redox system that possesses other special kinetic advantages within the overall desired charge transfer mechanism (ala the iodide/ triiodide or the cobalt complexes your group studies).

It is probably more tractable to consider Marcus theory when changing the driving force via QD size while keeping all other parameters constant. We know that a decrease in the size of a quantum dots correlates to a decrease in the density of states near the valence and conduction band edges. Using this approximation, it is also logical to assume that smaller dots correspond to an increase in driving force between the redox mediator and the quantum dot as well as between the conduction bands of the QD and TiO<sub>2</sub>. We will fit the transient absorption spectra using a biexponential decay kinetics model provided in the literature and define the charge transfer rate from the mediator to the QD as above and between the QD and TiO<sub>2</sub> as follows:

$$k_{ht} = 1/\tau_{(CdSe + TiO_2)} - 1/\tau_{CdSe}$$

Expectations tell us that we should expect faster charge transfer rates (more current) for smaller QDs, as well as better coverage of the Gratzel scaffold, with the same cell open-circuit voltage but we would expect a lowered visible light response. So one of the purposes of our research would be to answer the unknown questions of “So what’s the optimal size of QD for power conversion efficiencies for a given redox couple? Which pieces of the kinetics puzzle helps to explain this?”

Finally, I think it would be very exciting to measure multiexciton generation as *photocurrent* (which has never been published) and that is only possible by making an actual device. Having said that, the best QD photoelectrochemical cell systems to date have measured *external* quantum efficiencies that are only about 15% and so the premise of measuring IPCE's greater than 100% is ridiculous (although an *internal* quantum efficiency of greater than 100% may be measured if the measurement is setup to do so). Nonetheless, the observation of multiexciton generation is usually deduced from a "quantum jump in the efficiency once certain incident photon energy is reached". Along those lines, one should/ might observe a "quantum jump in efficiency" (maybe as photocurrent if we can differentiate the TiO<sub>2</sub> response from the composite system response and the excited state electron production step is rate-limiting so that it can be deduced from steady-state measurements) once we reach a certain point in the incident photon energy that is  $>2E_{BG}$ . Of course, this is only expected to happen with UV irradiation and so we will look for this only as a "proof of concept" rather than implying that it would significantly enhance the efficiency for our system with visible light- although QD's with a smaller band gap might be able to do this with visible light and such a demonstration could lead to additional large grants for research resulting from those proposals (just kidding). In either case, such a discovery would be quite exciting and is unprecedented for these composite photoelectrode materials.

## A.6 Concluding Remarks

The potential benefits and disadvantages of II-VI materials can be hotly debated. The cited disadvantages are typically centered on stability and environmental contamination. Although the use of metal oxides is often cited to overcome the stability issue, the band gap of metal oxides is expected to be too large for efficient utilization of the solar spectrum and the blue-shift resulting from quantum confinement would only augment this shortcoming. The environmental threat posed by the use of these materials appears to be more a problem of perception than reality.

To meet the DOE's vision for efficient, yet cost-effective, next-generation solar cells we offer a logical proposal that the need can be met once the performance of a quantum dot photoelectrode assembly has been optimized. The popular ruthenium-based sensitizers for nanocrystalline configurations that are so rigorously studied today may ultimately need to be replaced by another material that is far more inexpensive, yet comparably effective. Quantum dots present the very real possibility of meeting that need. Beyond the interesting fundamental study of Marcus Theory applied to these systems, it is also important to try a more diverse sampling of redox couples for CdSe quantum dot photoelectrodes than those that have been used thus far. Additional progress could be made in this research area by optimizing the system with respect to the choice of redox couple, and seeing how those same redox couples affect the stability.

## References

- (1) Dubertret, B. *Nature Mat.* **2006**, *4*, 797-798.
- (2) Coe, S.; Woo, W.-K.; Bawendi, M.; Bulovic, V. *Nature* **2002**, *420*, 800-803.
- (3) Wang, C.; Wehrenberg, B. L.; Woo, C. Y.; Guyot-Sionnest, P. *J. Phys. Chem. B* **2004**, *108*, 9027-9031.
- (4) Gur, I.; Fromer, N. A.; Geier, M. L.; Alivasatos, A. P. *Science* **2005**, *310*, 462-465.
- (5) Nozik, A. J. *Inorg. Chem.* **2005**, *44*, 6893-6899.
- (6) Nozik, A. J. *Annu. Rev. Phys. Chem.* **2001**, *52*, 193-231.
- (7) Nazeerudin, M. K.; Kay, A.; Rodicio, I.; Humphry-Baker, R.; Muller, E.; Liska, P.; Vlachopoulos, N.; Gratzel, M. *J. Am. Chem. Soc.* **1993**, *115*, 6382-6390.
- (8) Murray, C. B.; Norris, D. J.; Bawendi, M. G. *J. Am. Chem. Soc.* **1993**, *115*, 8706-8715.
- (9) Nozik, A. J. *Phys. E* **2002**, *14*, 115-120.
- (10) Schaller, R. D.; Klimov, V. I. *Phys. Rev. Lett.* **2004**, *92*, 186601.
- (11) Schaller, R. D.; Sykora, M.; Pietryga, J. M.; Klimov, V. I. *Nano. Lett.* **2006**, *In Press*.
- (12) Ellingson, R. J.; Nozik, A. J.; al., e. *Nano. Lett.* **2005**, *5*, 865-871.
- (13) Fox, L. S.; Kozik, M.; Winkler, J. R.; Gray, H. B. *Science* **1990**, *247*, 1069-1071.
- (14) Hamann, T. W.; Gstrein, F.; Brunschwig, B. S.; Lewis, N. S. *J. Am. Chem. Soc.* **2005**, *127*, 7815-7824.
- (15) Hamann, T. W.; Gstrein, F.; Brunschwig, B. S.; Lewis, N. S. *J. Am. Chem. Soc.* **2005**, *127*, 13949-13954.
- (16) Marcus, R. A. *Angew. Chem. Int. Ed.* **1993**, *32*, 1111-1222.
- (17) Lewis, N. S. *Annu. Rev. Phys. Chem.* **1991**, *42*, 543-580.

- (18) Hodes, G.; Grunbaum, E.; Feldman, Y.; Bastide, S.; Levy-Clement, C. *J. Electrochem. Soc.* **2005**, *152*, G917-G923.
- (19) Kronik, L.; Ashkenasy, N.; Leibovitch, M.; Fefer, E.; Shapira, Y.; Gorer, S.; Hodes, G. *J. Electrochem. Soc.* **1998**, *145*, 1748-1755.
- (20) Alperson, B.; Demenge, H.; Rubinstein, I.; Hodes, G. *J. Phys. Chem. B* **1999**, *103*, 4943-4948.
- (21) Alperson, B.; Cohen, S. *Phys. Rev. B* **1995**, *52*, R17 017- R17 020.
- (22) Golan, Y.; Hodes, G.; Rubenstein, I. *J. Phys. Chem.* **1996**, *100*, 2220-2228.
- (23) Golan, Y.; Alperson, B.; Hutchinson, J. L.; Hodes, G.; Rubinstein, I. *Adv. Mat.* **1997**, *9*, 236-238.
- (24) Ruach-Nir, I.; Wagner, H. D.; Rubinstein, I.; Hodes, G. *Adv. Funct. Mat.* **2003**, *13*, 159-164.
- (25) Ruach-Nir, I.; Zhang, Y.; Popovitz-Biro, R.; Rubinstein, I.; Hodes, G. *J. Phys. Chem. B* **2003**, *107*, 2174-2179.
- (26) Bakkers, E. P. A. M.; Vanmaekelbergh, D.; al., e. *J. Phys. Chem. B* **2000**, *104*, 7266-7272.
- (27) Bakkers, E. P. A. M.; Kelly, J. J.; Vanmaekelbergh, D. *J. Electroanal. Chem* **2000**, *482*, 48-55.
- (28) Choi, S.-J.; Woo, D.-H.; Myung, N.; Kang, H.; Park, S.-M. *J. Electrochem. Soc.* **2001**, *148*, C569-C573.
- (29) Myung, N.; Tacconi, N. R. d.; Rajeshwar, K. *Electrochem. Comm.* **1999**, *1*, 42-45.
- (30) Bakkers, E. P. A. M.; Reitsma, E.; Kelly, J. J.; Vanmaekelbergh, D. *J. Phys. Chem. B* **1999**, *103*, 2781-2788.
- (31) Spanhel, L.; Haase, M.; Weller, H.; Henglein, A. *J. Am. Chem. Soc.* **1987**, *109*, 5649.
- (32) Peng, X.; Wilson, T. E.; Alivisatos, A. P.; Schultz, P. G. *Angew. Chem. Int. Ed.* **1997**, *36*, 145.
- (33) Noglik, H.; Pietro, W. *Chem. Mater.* **1994**, *6*, 1593.

- (34) Lifshitz, E.; Dag, I.; Litvin, I.; Hodes, G.; Gorer, S.; Reisfeld, R.; Zelner, M.; Minti, H. *Chem. Phys. Lett.* **1998**, *288*, 188-196.
- (35) Myung, N.; Bae, Y.; Bard, A. J. *Nano. Lett.* **2003**, *3*, 747-749.
- (36) Alperson, B.; Rubinstein, I.; Hodes, G. *Phys. Rev. B* **2001**, *63*, 081303.
- (37) Sze, S. M. *Physics of Semiconductor Devices*; 2nd ed. ed.; Wiley: New York, 1981.
- (38) Fajardo, A. M.; Lewis, N. S. *J. Phys. Chem. B* **1997**, *101*, 11136-11151.
- (39) Fajardo, A. M.; Lewis, N. S. *Science* **1996**, *274*, 969-972.
- (40) Liu, D.; Kamat, P. V. *J. Phys. Chem.* **1993**, *97*, 10769-10773.
- (41) Liu, D.; Kamat, P. V. *J. Electroanal. Chem* **1993**, *347*, 451-456.
- (42) Regan, B. O.; Gratzel, M. *Nature* **1991**, *353*, 737.
- (43) Vogel, R.; Hoyer, P.; Weller, H. *J. Phys. Chem.* **1994**, *98*, 3183-3188.
- (44) Peter, L. M.; Riley, D. J.; Tull, E. J.; Wijayantha, K. G. U. *Chem. Comm.* **2002**, 1030-1031.
- (45) Shen, Q.; Arae, D.; Toyoda, T. *J. Photochem. Photobiol. A* **2004**, *164*, 75-80.
- (46) Robel, I.; Subramanian, V.; Kuno, M.; Kamat, P. *J. Am. Chem. Soc.* **2006**, *In Press*.
- (47) Barbe, C. J.; Arendse, F.; Comte, P.; Jirousek, M.; Lenzenmann, F.; Shklover, V.; Gratzel, M. *J. Am. Ceram. Soc.* **1997**, *80*, 3157.
- (48) Toyoda, T.; Tsuboya, I.; Shen, Q. *Mat. Sci. Eng. C* **2005**, *25*, 853-857.
- (49) Colvin, V. L.; Alivisatos, A. P.; Tobin, J. G. *Phys. Rev. Lett.* **1991**, *66*, 2786-2789.
- (50) Diol, S. J.; Poles, E.; Rosenwaks, Y.; Miller, R. J. D. *J. Phys. Chem. B* **1998**, *102*, 6193-6201.
- (51) Knox, W. H.; Chemla, D. S.; Miller, D. A. B. *Phys. Rev. Lett.* **1989**, *62*, 1189-1192.

- (52) Koval, C. A.; Austerman, R. L.; Turner, J. A.; Parkinson, B. A. *J. Electrochem. Soc.* **1985**, *132*, 613-623.
- (53) Miller, R. J. D.; McLendon, G.; Nozik, A.; Willig, F.; Schmickler, W. *Surface Electron-Transfer Processes*; VCH: New York, 1995.
- (54) Morrison, S. R. *Electrochemistry at Semiconductor and Oxidized Metal Electrodes*; Plenum: New York, 1980.
- (55) Kittel, C. *Introduction to Solid State Physics*; 6th ed. ed.; Wiley: New York, 1986.
- (56) Sykora, M.; Petruska, M. A.; Alstrum-Acevedo, J.; Bezel, I.; Meyer, T. J.; Klimov, V. I. *J. Am. Chem. Soc.* **2006**, *128*, 9984-9985.

## Appendix B: Introduction to the High Throughput Materials Screening Database

Due to the large number of materials that have been produced and tested throughout this project, a database was created using Filemaker® software. This software is currently in the group's possession, the databases are currently stored on the group server under my folder (which is not password protected), and the printed films have been organized in two shelves in the lab according to the date they were produced and described in the lab notebooks. A sample screen of the largest of these databases, for the four-metals-mixed-three-at-a-time template, is shown below.





**Plate Number 38** Experiment References: EF

<p>Metal A La Metal B Fe Metal C Cu Metal D K</p>	<p><b>Laser Wavelength</b>  <input checked="" type="radio"/> 632.8 nm <input type="radio"/> 514.5 nm <input type="radio"/> 532 nm <input type="radio"/> 488 nm  <b>Laser Power (mW)</b> 11.5      <b>Firing Temperature (°C)</b> 500</p>
---	--

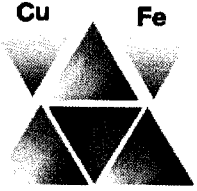
**pH**  
 Acidic  Neutral  Basic

**Positive Bias Scan** Positive txt file  Acidic  Neutral  Basic  
 38 Ternary Funk E.txt      **Date Scanned** 8/4/2004



Fe Internal Standard IPCE  
2.0 E-6

Highest n-type IPCE  
6.2 E-6



▲ A  
▲ B  
▲ C  
▲ D

**Negative Bias Scan** Negative txt file  
 38 Ternary Funk F.txt



Cu Internal Standard IPCE  
4.1 E-6

Highest p-type IPCE  
6.8 E-6

Submitted by  
Mike

**Positive Bias Score for Best Triangle**  
 Not Scanned  Below Standard  Same As Standard  Above Standard  Outstanding

**Negative Bias Score for Best Triangle**  
 Not Scanned  Below Standard  Same As Standard  Above Standard  Outstanding

Figure B.1: Sample screen of a combination in the ternary mixtures library.

There are several fields of data that are input for each scanned film. In addition to the images seen for qualitative comparisons of the printed materials, the exact name of the corresponding text file is given should one be interested in a more thorough, perhaps quantitative, investigation of the data. The fields at the bottom are more of a subjective “score”, with the label “outstanding” historically reserved for those materials displaying IPCE values at least twice that of the respective internal standards. On the right side of the screen, shown below in Figure B.2, is a field for any comments that may be added as well as reference electrode information. The rest of the input fields are fairly self-explanatory.

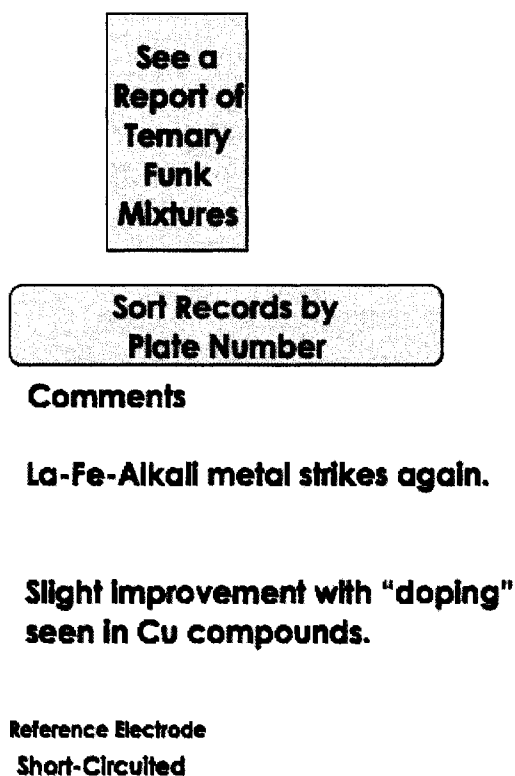


**Figure B.2:** The right side of the sample screen of a combination in the ternary mixtures library.

A couple of other amenities designed for this database are available as macros within the program. First, it is possible to search the entire database for any numerical value, material identity, input field, or any combination thereof. This is begun by clicking on the magnifying glass button in the upper left of the screen (not shown here). It is also possible to generate an organized columnar report of this search result by clicking on the button labeled "See a Report of Ternary Funk Mixtures". One can also organize the search results by plate number by clicking on the corresponding button.

All of the materials printed to date were predominantly nitrate salts, whenever it was available for a given precursor. Titanium chloride (in the form of 2 M aqueous  $\text{TiCl}_4$ ) is one notable exception. It is straightforward to determine who printed which film as the "Submitted By" field has been incorporated into the program. Researching the appropriate plate number in the lab notebooks can also retrieve the scanning parameters for each film.

Although the example shown was for ternary mixtures, smaller databases for quaternary mixtures and ternary "zoom-ins" were also created and are available in the same location on the group server. Backups have also been made onto my personal external hard drive. As always, I am available for personal consultations should the next individual working on this project have any questions regarding this database or any other issue.